Protonation-dependent alternating access of a spinster transporter, an emerging family of broad-specificity efflux pumps

Reza Dastvan[1,*], Ali Rasouli[2,§], Sepehr Dehghani-Ghahnaviyeh[2,§], Samantha Gies[1], Emad Tajkhorshid[2,*]

[1] Department of Biochemistry and Molecular Biology, Saint Louis University School of Medicine, St. Louis, MO 63104, USA

[2] Department of Biochemistry and NIH Center for Macromolecular Modeling and Bioinformatics, Beckman Institute for Advanced Science and Technology, University of Illinois at Urbana-Champaign, Urbana, IL 61801, USA

* To whom correspondence may be addressed. Email: reza.dastvan@health.slu.edu, emad@illinois.edu.

[§] These authors contributed equally to this work.

Abstract

Spinster (Spns) lipid transporters are critical for transporting sphingosine-1-phosphate (S1P) across cellular membranes. S1P regulates growth, survival and migration of cells with profound proangiogenic effects. Of the three human Spns proteins, Spns2 functions as the main S1P transporter, making it a potential drug target for modulating S1P export and signaling. Using an integrated approach in lipid membranes, we employed double electron–electron resonance (DEER) spectroscopy, combined with molecular dynamics simulations and site-directed mutagenesis of conserved residues to generate new conformational states of a close bacterial homolog of the human Spns proteins from *Hyphomonas neptunium* (*Hn*Spns) and to define its proton- and substrate-coupled conformational dynamics. Our systematic study reveals conserved residues critical for protonation and its regulation, and how sequential protonation of these switches drives conformational transitions in the context of a global description of a noncanonical ligand-dependent alternating access in the absence of an obvious outward-facing conformational state. A periplasmic salt bridge keeps the transporter in a closed conformation, while protonation-dependent conformational dynamics are significantly enhanced on the periplasmic side, providing a pathway for ligand exchange. Another distinctive feature of *Hn*Spns is the decoupling of transmembrane protonation-dependent conformational changes that may be facilitated by hinged transmembrane helices with more flexible periplasmic halves of the gating helices. Our resistance assays to structurally unrelated antibiotics and antimicrobial compounds reveal substrate polyspecificity and *Hn*Spns multidrug resistance (MDR) activity that underscore the previously unknown role of *Hn*Spns and potentially human Spns proteins in MDR, beyond their sphingolipid transport and signaling activities.

Significance Statement

The Spinster (Spns) lipid transporters use ion electrochemical gradients to drive substrate transport, including the bioactive lipid sphingosine-1-phosphate. This study investigated how binding of protons powers the conformational changes that enable transport by *Hn*Spns, a bacterial Spns transporter from *Hyphomonas neptunium*. The results show that sequential protonation of two highly conserved acidic residues, regulated by the strength of a nearby positive electrostatic potential, induces reconfiguration of the structure from an inward facing to an inward- and outward-closed conformation with enhanced flexibility of the periplasmic side of the transporter to enable ligand exchange. Protonation, not substrate binding, drives this non-canonical alternating access. Our functional assays reveal a previously unknown multidrug resistance activity of *Hn*Spns and potentially the human Spns family.

Introduction

The bioactive lipid sphingosine-1-phosphate (S1P) plays a key role in regulating the growth, survival and migration of mammalian cells. Thus, it is critical for lymphocyte trafficking, immune responses, vascular and embryonic development, metastatic cancer, and bone homeostasis.[1-4] S1P is produced intracellularly by sphingosine kinases and then released extracellularly to engage in its physiological or pathological roles. Its accumulation is linked to the development/progression of cancer and various other diseases, including atherosclerosis, diabetes and inflammatory disorders. The Spinster (Spns) lipid transporters of the major facilitator superfamily (MFS) are critical for transporting S1P across cellular membranes.[5-7] The Spns family includes three S1P or sphingolipid transporters (Spns1-3) in humans. Spns1 is associated with lysosomal membranes and is one of the major efflux transporters removing degradation products, including sphingolipids, from the lysosomal lumen to maintain normal size and function. It also participates in the late stages of autophagy. Thus, its loss of function is associated with human lysosomal storage diseases and neurodegenerative diseases.[6] Though less-studied, high Spns3 expression is associated with poor prognosis in chemotherapy patients with acute myeloid leukemia and in renal cancer.[8] Spns2 is localized in the cell membrane and functions as a physiologically relevant S1P transporter.[6,7] S1P extracellularly activates its receptors (S1PR1–5), allowing it to regulate many important cellular functions.[1] Its secretion by Spns2 plays a critical role in controlling S1P levels in circulatory fluids, thus boosting immune cell function in lymph, implying that Spns2 might be a potential immunosuppressant drug target.[9-13] Spns2 transports the S1P analog FTY720-P, an immunomodulating agent, out of cells to bind the S1P receptor and block lymphocyte egress into blood circulation.[5] Interestingly, endothelial cell-specific knockout of Spns2 in mice results in impaired lymphocyte egress and prevents tumor metastasis.[1,14] This strongly suggests that Spns2 could be an effective target for reducing metastases by increasing the efficacy of immunotherapy.[1] Spns2 overexpression in non-small cell lung carcinoma cells increases S1P secretion, but also leads to increased apoptosis and decreased cell migration.[1] Thus, a detailed understanding of the functional mechanism of Spns2 and its regulation are of high significance to resolve these seemingly different observations and to provide a molecular framework for developing new therapeutic strategies for diseases associated with S1P signaling.

Spns proteins are MFS secondary active transporters that use the electrochemical gradient of proton or sodium ions to drive substrate transport.[15] Crystal structures of several MFS transporters reveal that these proteins possess a 12-transmembrane (TM) helix core consisting of two pseudo-symmetrical domains, namely the N-terminal domain (NTD: TMs 1-6) and the C-terminal domain (CTD: TMs 7-12) (Fig. 1A). Between the two domains there is a central cavity serving as both the binding site and transport path for the substrate. An MFS transporter usually consists of four pseudo-symmetrical, three-helix repeats.[16,17] “Cavity-helices”, the first in each repeat (TMs 1, 4, 7, and 10; Fig. 1), contribute to the formation of the cavity. “Gating-helices”, the second in each repeat (TMs 2, 5, 8, and 11), are usually long and curved, possessing a banana-like shape. Together, these four helices form the side walls of the central cavity and provide a lateral gating mechanism to the membrane leaflets. The third group of shorter “support-helices” (TMs 3, 6, 9, and 12) does not directly contribute to cavity formation, but does contact the lipid bilayer.[15,18] An alternating access mechanism for substrate transport involves a series of protein conformational changes allowing access of the ligand binding site to extracellular and intracellular solutions/membrane leaflets.[19] Thus, a transporter often undergoes structural transitions between three major functional states: the inward-facing (IF), the outward-facing (OF), and possibly the occluded (O) conformations. In MFS proteins, these states may be stabilized by the formation and breaking of inter- and intra-domain salt bridges.[20] In Spns proteins, the gating helices are hinged and especially their periplasmic/extracellular halves are inherently flexible due to the frequent occurrence of highly conserved helix-breaking residues like glycine (Figs. 2F-2H). This deviation from rigid-body movement of these “rocker” helices in the context of a rocker-switch model of the conformational change between the IF and OF states hints at a noncanonical alternating access mechanism for Spns proteins possibly involving an occluded conformation.[21-23]

While an AlphaFold model for the human Spns2 has been generated (Fig. 1C),[24] its experimentally-resolved structures are yet to emerge. Atomic resolution structures of a bacterial Spns transporter from *Hyphomonas neptunium* (*Hn*Spns) with high sequence similarity to human

Spns2 (~20% sequence identity), have recently been elucidated (Figs. 1 and 2).[25] The architecture of the *Hn*Spns core follows the typical MFS fold (Figs. 1A and 1B). The IF crystal structure of *Hn*Spns (Fig. 1) reveals the binding mode of an unspecified substrate in the cavity near conserved residue, Arg42^{TM1}, which is locked in position by interactions with conserved residues Glu129^{TM4} and Arg122^{TM4} (Fig. 1B, green circle).[25] Additionally, the structure reveals a potential proton binding site in the NTD (Fig. 1B, blue circle), comprised of highly conserved residues Asp41^{TM1} (Fig. 2A), Trp102^{TM3} and Thr106^{TM3} (Fig. 2E). Compared with other MFS transporters, the binding cavity in *Hn*Spns has fewer charges (e.g., Arg42^{TM1}) and is less hydrophilic (e.g., Tyr277^{TM7} and Tyr371^{TM10}), implying a lipidic or lipophilic nature for its transport substrate, e.g., S1P. More than half of the conserved residues between Spns proteins are localized around the inner cavity and most of them are found in the NTD of *Hn*Spns (Fig. 2).[25] Hence, the structure suggests that human Spns proteins also transport negatively charged lipophilic small molecules, and the conserved residue Glu129^{TM4} might serve as the main protonation switch regulating the proton motive force (PMF)-coupled conformational transitions.[25] The most conserved motif in MFS transporters, motif A (Figs. 2E and 1B), is located in the intracellular loop connecting TMs 2 and 3.[15,26] Motif A and its surrounding residues from TM4 and TM11 form a conserved "structural motif A", stabilizing the O or OF conformation.[15] A structural motif A associated charge-relay network, Asp87$^{motif\text{-}A}$-Arg91$^{motif\text{-}A}$-Asp142^{TM4}, is proposed to regulate the inter-domain charge-dipole interaction between TMs 2 and 11 (Fig. 1A). In addition, based on the structure, a salt bridge could be formed between symmetry-related TMs 5 and 8. The highly conserved Arg122^{TM4} is the signature residue of a B-like motif "RxxxG" in Spns proteins (Figs. 2C and 1B), although in *Hn*Spns, the conserved Gly in the motif is replaced by an alanine.[15] This motif also exists in proton-coupled sugar and sugar acid symporters such as *E. coli* XylE and DgoT.[27,28] The arginine of this motif carries a buried positive charge, and all the putative protonation sites inside the central cavity (i.e., Asp41^{TM1} and Glu129^{TM4}) are in close proximity to this residue (Fig. 1B). It is proposed that increasing the strength of the positive electrostatic potential inside the central cavity in the IF state is a common mechanism of promoting the cytosolic proton release step in MFS transporters.[15]

*Hn*Spns was captured in the same IF conformation with and without an uncharacterized substrate.[25] Thus, the alternating access mechanism and the protonation-dependent conformational dynamics of the transporter are undefined. In addition, the transport direction of the ligands (i.e., symport vs. antiport) and the stoichiometry of the transported ions (i.e., electrogenic vs. electroneutral transport) remain poorly understood but crucial aspects of the transport mechanism in Spns proteins. Here, we employed double electron–electron resonance (DEER; also called PELDOR) spectroscopy,[29-33] combined with nonequilibrium-driven[34-39] and restraint-assisted molecular dynamics (MD) simulations[40] to generate new conformational states of *Hn*Spns in the membrane and to define its proton- and substrate-coupled conformational changes in a lipid bilayer-like environment. Our systematic study reveals the conformational changes of *Hn*Spns following protonation of critical acidic residues, conserved in most Spns proteins and their bacterial homologs (Figs. 2A and 2C), in the context of a global description of a noncanonical ligand-dependent alternating access.

Results

Defining the transport cycle of Spns transporters entails identifying the conformational states that enable binding, translocation and exit of the substrate and elucidating the sequence and structural elements (e.g., protonation switches) that control the isomerization of the transporter between functional states. Considering the inwardly directed proton gradient across the plasma membrane, *Hn*Spns could function as a symporter to enable uptake of its substrate or similar to Spns2 as an efflux antiporter. Thus, to define the ligand dependence of *Hn*Spns, which putatively couples proton translocation to the cytoplasm to substrate extrusion to the periplasm, DEER distance distributions were determined at pH 4 to mimic a protonated state, at pH 7.5, and pH 9 to favor deprotonation, and for selected pairs on cavity and gating helixes in the presence of S1P at pH 7.5 to populate a substrate-bound state. These studies were performed both in lauryl maltose

neopentyl glycol (LMNG) micelles and *Hn*Spns reconstituted into nanodiscs composed of plasma membrane phospholipids (Fig. S1A and S1B).

Structural and functional integrity of *Hn*Spns mutants and the Multidrug Resistance (MDR) activity. To apply DEER spectroscopy, cysteine mutations are introduced at sites of interest on a cysteine-less (CL) background. The effect of introducing spin labels on structural integrity was monitored by thermal stability analysis using circular dichroism (CD) spectroscopy in micelles and nanodiscs and compared to the CL *Hn*Spns for each mutant (Fig. S1, Table S1).[41] Introducing spin labels does not significantly affect the structural integrity of the CL transporter. Among protonation-mimetic mutations of acidic residues in lipid nanodiscs, D142N and E129Q have the highest and the lowest T_m values, respectively (Fig. S1D, Table S1). Introducing the D41N mutation in micelles or combined with E129Q in both environments (Figs. S1C and S1D), enhances the thermal stability of *Hn*Spns. D142N putatively stabilizes the IF conformation by interrupting the structural motif A-associated charge-relay network.[20] Thus, the effect of these mutations on the stability of *Hn*Spns could reflect their influence on its structural dynamics and functional properties.

Functional integrity of the CL and the protonation-mimetic mutants compared to wildtype (WT) transporter was determined using a cell growth assay in *Escherichia coli*.[42] The assay measures the resistance conferred by *Hn*Spns to toxic concentrations of a spectrum of structurally unrelated antibiotics and antimicrobial compounds like capreomycin, rifampicin and ethidium bromide (Fig. S2). Unlike S1P, these drugs are uncharged or positively charged. Water-soluble compounds ethidium bromide and capreomycin (a cyclic polypeptide antitubercular antibiotic) are known substrates of the *Mycobacterium smegmatis* MDR efflux transporter MSMEG_3705 (*Ms*Spns), a close homolog of *Hn*Spns and other Spns proteins (Fig. 2).[43] It has been reported that *Ms*Spns is unable to confer resistance against the highly lipophilic drug rifampicin, the most effective first-line antibiotic against tuberculosis. In our resistance assays, CL and WT *Hn*Spns similarly conferred resistance against different concentrations of these compounds, highlighting the relevance of the CL construct in our studies. Interestingly, as observed previously for *Ms*Spns, under low but still toxic concentrations of rifampicin, *Hn*Spns expression inhibits cell growth seemingly increasing the drug uptake, unlike ethidium bromide and capreomycin. However, at higher concentrations of rifampicin that could accumulate in the cells by diffusion, *Hn*Spns can significantly enhance resistance to the drug that quickly diminishes by further increasing drug concentration (Fig. S2). Interestingly, at toxic concentrations of rifampicin (10 μg/ml) and capreomycin (52.5 μg/ml) at 4 hrs, the protonation-mimetic mutants differentially conferred resistance to these compounds relative to the WT or CL transporter, with compromised and enhanced drug resistance for the D142N and the E129Q, respectively, and relatively unaltered resistance for D41N and D41N/E129Q mutations. These observations underscore the previously unknown role of *Hn*Spns and potentially human Spns proteins in MDR in addition to their sphingolipid transport activity. The mechanistic significance of these observations will be further elaborated in the Discussion.

Protonation induces closing of the intracellular side with distinct rearrangements for gating and cavity helices. For distance pairs across the *Hn*Spns on the symmetry-related gating helices 2-11 and 5-8 (Fig. 3) that are directly involved in inter-domain conformational changes, shifts to shorter distances were observed on the intracellular side at pH 4. The distance population for the TM2-TM11 pair corresponds to the formation of the structural motif A between TMs 2-4 and 11 in an intracellular closed (IC) homology model of *Hn*Spns, hence closing of the intracellular side. Though TM5 and TM8 move closer at pH 4, the experimental distance population does not match the predicted distance distribution corresponding to the formation of a salt bridge between TMs 5 and 8 in the IC model. Also, the formation of this salt bridge was not observed in our MD simulations. Overall, the populated states at different pH values were similar for LMNG micelles and lipid nanodiscs (Figs. 3, 4 and S3). The pH 4 conformational state was found to be more populated in the lipid nanodiscs compared with micelles. The experimental distance distributions in micelles on the gating helices at basic pH values correspond well with the predicted distributions calculated from the X-ray IF structure (Fig. 3B). Conversely, the protonation-dependent pattern of distance changes between pairs involving cavity helices, TMs 1 and 4 (Fig. 4) is entirely different from the gating helices, suggesting that rotating or bending of TMs 1 and 4 may be required for the

structural transition. Notably, unlike gating helices, TMs 1 and 4 distance distributions showed disagreements with the predicted distributions calculated from the X-ray structure.

Protonation induces an outward-closed conformation with a flexible lateral opening between TMs 5 and 8. Gating TM pairs 2-11 and 5-8 behave differently on the extracellular side (Fig. 5). The distance between TM2 and TM11 is shorter at pH 4, possibly due to rotation of TM11. Unlike this pair that is more structured, the TM5-TM8 pair is highly dynamic with a shift to longer distances at pH 4. The periplasmic halves of TMs 5 and 8 are intrinsically flexible due to the frequent occurrence of highly conserved glycine residues (Figs. 2F and 2G) that might imply a role in the gating mechanism. There is a highly conserved salt bridge on the periplasmic side of Spns proteins and *Hn*Spns formed by Asp60^{TM2} and Arg289^{TM7}. This salt bridge tightly couples TMs 1/2 and 7 and possibly inhibits the periplasmic opening of *Hn*Spns, thus stabilizing the IF and an outward-closed conformations. Indeed, we find that pH-dependent distance changes are significantly attenuated for distance pairs between TM7 and TM1 or other helices like TM3 (Fig. 6). Distance distributions for pairs with Ser57 on TM1 present substantial protonation-dependent changes, hinting at twisting of the TM1 away from TM3. Overall, the pH-dependent distance changes on the periplasmic side provide evidence for an outward-closed conformation under acidic conditions with a flexible lateral opening toward the membrane to enable the release of lipophilic substrates including drugs. The experimental distance distributions in both micelles and lipid nanodiscs at basic pH values correspond to the predicted distributions calculated from the X-ray IF structure (Figs. 5, 6, and S4). Notably, shifts to shorter average distances in lipid nanodiscs compared with micelles were observed for distance pairs to the lipid-interacting helix TM3. Also, the amplitudes of pH-dependent conformational changes were higher in micelles than in nanodiscs. From both intracellular and periplasmic pairs like M84-S386, M84-Y143, S57-L111 and M288-L111, three conformational intermediates can be detected at different pH values, likely due to different protonation states of the proton-coupled residues.

S1P binding to *Hn*Spns stabilizes the IF conformation. Although S1P is not a native substrate of *Hn*Spns, the conserved substrate binding cavity residues in the Spns proteins (Fig. 2) imply a lipophilic nature for their transport substrates. Addition of S1P to *Hn*Spns in lipid nanodiscs (pH 7.5) did not produce a substantial shift in the conformational equilibrium but a slight global shift to shorter distances on both sides was observed (Fig. 7). If this finding persists with other potential substrates, it implies that protonation is the main driver of the alternating access mechanism in these transporters. Our resistance assays highlighted *Hn*Spns and potentially other Spns proteins as MDR transporters being able to transport a wide range of compounds in addition to sphingolipids and their metabolites as their physiological substrates.

Interaction of Glu129^{TM4} with Arg42^{TM1} in the substrate binding site is largely regulated by protonation of Asp41^{TM1}. The structure of *Hn*Spns contains two titratable buried residues at the NTD, Glu129^{TM4} and Asp41^{TM1}. Glu129 was previously hypothesized to be the master proton-coupled switch, triggering the conformational transition.[25] Due to the proximity between Glu129 and Asp41, using MD simulations, we explored the local conformational changes in different permutations of protonation states of these two acidic residues (four different systems) and their interactions with two nearby basic residues, the substrate binding residue Arg42^{TM1} and Arg122^{TM4}. Arg122^{TM4} is expected to promote deprotonation of nearby acidic residues in the IF state. In the course of our simulations, we monitored the formation of two specific salt bridges, Glu129-Arg42 and Asp41-Arg122, by calculating pairwise distances between the side chains of these residues. Stable interactions between these pairs are formed when both acidic residues are deprotonated (Figs. 8C and S5C). Notably, upon Asp41 protonation, its interaction with Arg122 is lost (Figs. 8A and S5A) but the deprotonated Glu129-Arg42 interaction is intact. Double protonation of the acidic residues stabilizes a distinct conformation in which the side chain of Arg122 continuously and transiently interacts with the backbone oxygen of Arg42 and Asp41, respectively (Figs. 8B, S5B, and S5E), thereby prohibiting the rotational freedom of TM1 that is essential for both substrate binding and conformational transition. This might explain the higher thermal stability of this mutant (Figs. S1C and S1D). In contrast, only if Asp41 is deprotonated and interacting with Arg122 can Glu129 function as the intracellular master switch. Glu129 protonation liberates Arg42, allowing it

to bind the substrate and triggers the local, and possibly global, conformational changes (Figs. 8D and S5D). As a plausible coupling mechanism, protonation of Glu129 is promoted by decreasing the strength of the nearby positive electrostatic potential, either by neutralization of the highly conserved Arg122 by formation of a charge pair with deprotonated and charged Asp41 or by binding of substrate to Arg42.

Protonation-dependent conformational changes occur while preserving the extracellular-closed conformation. In our MD simulations, we observe that protonation of Asp41 releases this residue from Arg122, enabling the rotation/bending of TMs 1 and 4 (Fig. 8A vs. 8C, middle panel). Under this condition, the charge relay network essential for the assembly of the structural motif A and for the conformational transition cannot be formed, thereby stabilizing the IF conformation (Fig. 8A, lower panel). However, protonation of Glu129 alone (Fig. 8D) triggers the most conformational changes in TMs 1 and 4 and enables the proper formation of the charge relay network. Bending of the gating helix TM2 on the intracellular side occurs for either of these protonation events, providing a passage for substrate binding. However, only in the singly protonated Glu129, the now freed Arg42^{TM1} and Tyr277^{TM7} (GY^{277}G) become available for substrate binding (Fig. 8D). Double protonation (Fig. 8B) has a similar effect on charge relay network formation as the single protonation of Asp41. Interestingly, all these local and global protonation-dependent conformational changes that trigger the closing of the intracellular side could occur without disrupting the periplasmic salt bridge between Asp60^{TM2}-Arg289^{TM7} that stabilizes the extracellular-closed conformation, suggesting the population of the IF and doubly-occluded conformations.

Independent proton-coupled conformational changes on the two sides of *Hn*Spns. Our experimental DEER data using protonation-mimetic mutations of the proton-coupled residues support the results of the MD simulations (Figs. 9, S6 and S7). On the intracellular side and probed by the distance pair M84-S386 between TMs 2 and 11 (Fig. 9A), the E129Q mutation shifts the equilibrium towards the pH 4 state that represents the formation of the structural motif A and closing of the intracellular side. For most of the probed intracellular pairs, the E129Q mutation captures the transporter in the pH 4 population state, i.e., the inward-closed conformation (Figs. 9A and S8). Thus, our data suggest that E129 is the intracellular protonation master switch regulating the conformational transition between IF and inward-closed states. However, the D41N mutation has the opposite effect, shifting the equilibrium to the pH 9 state (Figs. 9A and S6). Mutation of the Asp142^{TM4} in the charge relay network produces a similar effect as the D41N mutation, as shown previously on other MFS transporters (Figs. 9A and S6).[20] Importantly, for the M84-S386 pair with the double E129Q/D41N mutation, the effect of D41N on closing of the intracellular side dominates that of E129Q. Interestingly, for the S25-S386 distance pair that monitors the conformational changes in TM1, the reverse effect of the D41N mutation can be observed in both DEER and CW EPR data (Fig. 9A). The change in the CW spectra hints at the rotation/bending of the TM1 that affects the local spin dynamics. Our MD simulations indicate that rotation/bending of TM1 could still occur in the doubly protonated state (Fig. 8B, middle panel), a prediction supported by our DEER measurements on the S25-S386-D41N-E129Q. On the periplasmic side, though slight shifts in the conformational equilibria can be observed with different protonation-mimetic mutations, the amplitude of the changes are much smaller than the intracellular side, indicating independent proton-coupled conformational changes on the two sides of the transporter (Figs. 9B, S7, and S9).

Periplasmic side of *Hn*Spns senses the proton differently. The pH-dependent conformational equilibrium of ligand-free *Hn*Spns in lipid nanodiscs and micelles was further investigated using different distance pairs on both intracellular and periplasmic sides. Variation in the population of rising states as a function of pH was used to estimate the pK of the conformational transition (Figs. 10, S10, and S11). Interestingly, a pK value of 7.6 was obtained for the S25-S386 intracellular pair from a nonlinear least-squares fit, which monitors relative movement of TM1 and TM10/TM11 (Figs. 10A and 10B). Since the pK reflects the protonation/deprotonation of acidic residue(s) as the driver of *Hn*Spns isomerization, this high pK value most likely is related to the protonation state of buried protonation sites inside the central cavity (i.e., Asp41^{TM1} and Glu129^{TM4}). A Hill coefficient of 1.0 was determined that hints at independent protonation events. On the contrary, an acidic pK value of 4.8±0.1 was determined for the periplasmic pairs S57-K427 (TM1-TM11) and S57-L111 (TM1-

TM3; Figs. 10A and 10B). This significantly lower pK on the periplasmic side could reflect the protonation state of Asp60^{TM2} that forms a highly conserved salt bridge to Arg289^{TM7}, which inhibits the periplasmic opening of *Hn*Spns. This finding further highlights the dissociation of the intracellular and periplasmic protonation-dependent conformational changes, which was further investigated by repeating these titration experiments on double and single protonation-mimetic mutations of Asp41 and Glu129 (Figs. 10C, 10D, and S10). We were not able to study Asp60 or Arg289 mutations due to negligible protein expression. As predicted, the D41N mutation on the intracellular distance pair shifts the pK value from 7.6 to 6.4, possibly reflecting a lower pKa of the less buried residue Glu129. The D41N-E129Q double mutation completely abrogates conformational changes on the intracellular side and stabilizes the inward-closed conformation, further demonstrating that the observed pK value reflects the protonation/deprotonation of these two intracellular switches. Predictably, similar protonation-mimetic mutations have no significant effect on the extracellular pK of conformational transition (Figs. 10C, 10D, and S10). The pH-dependence of the CW EPR spectra of the S25-S386 (TM1-TM10/11) intracellular pair reflects change in the local spin label dynamics, possibly rotation/bending rearrangements, and correlates with the corresponding DEER titration experiment (Fig. S12A). Interestingly, the D41N and E129Q mutations shift the equilibrium in opposite directions towards basic and acidic pH states, respectively (Fig. S12B). Similar pK values were obtained in LMNG micelles and lipid nanodiscs (Fig. S11).

DEER guided refinement of IF *Hn*Spns structure and modeling the doubly-occluded state. Starting from the X-ray IF conformation of the *Hn*Spns, we performed well-tempered metadynamics, an enhanced sampling MD technique,[44] to sample different conformations of the transporter ranging from IF to O. The conformations were sampled in a phase-space composed of two orientation-based collective variables (CVs) denoted as α and β angles representing the intracellular and extracellular openings, respectively (Fig. S16). During 200-ns metadynamics simulations, a putative O conformation was captured. This conformation was stabilized by forming two salt-bridges, namely Arg289^{TM7}-Asp60^{TM2} and Arg390^{TM11}-Asp142^{TM4}, respectively (Fig. S13E). The following 500-ns equilibrium simulation of the obtained O structure confirmed the stability of the formed salt bridges as well as the intracellular closure with reference to the starting IF conformation (Fig. S13C). Both the IF and O structures were refined using the DEER distance population histograms at pH 9 and 4, respectively, employing restrained-ensemble MD (reMD) simulation (Fig. 11).[40] The refined models match the experimentally determined distance populations (Figs. S14 and S15). The intracellular protonation master switch Glu129 is predicted to have a pKa of approximately 4.0 and 6.4 (H++ server) in the refined IF and O models, respectively.[45] This could indicate further sequestration and protonation of this residue in the O model. Interestingly, the predicted pKa for the Glu129 in the O state matches the experimental intracellular pK of conformational changes in lipid nanodiscs for the D41N mutation that is more reflective of the Glu129 protonation state (Fig. 10C). With its side chain carboxyl relatively more sequestered, Asp41 is predicted to have a pKa of 6.2 in the IF model that is increased to 7.8 in the O state, corresponding to the increased intracellular pK for the WT protein with intact Asp41 besides the Glu129 (Fig. 10A).

The NTD charge relay network is accompanied by an inter-domain hinge loop (i.e., L6-7). This linker peptide contains a number of polar residues (often positively charged) as well as an amphipathic α-helix (Fig. 1B). In the IF crystal structure of *Hn*Spns, the hinge loop (L6-7) is tethered to TM4 and TM2 via interactions between Arg233 and Gly234 with Asp87$^{motif\text{-}A}$ and Asp142^{TM4}, respectively (Fig. 1B).[25] In the O state (Fig. 11C), this tether is released (Fig. S3, M84-S236 pair: pH 7.5 to 4.0), and the structural motif A is formed. According to the "motif A hypothesis",[15] protonation-induced conformational rearrangements are sensed by the amphipathic α-helix. This helix further induces a conformational change in L6–7. Through the charge-relay network, the positive charges (e.g., Arg233) of the loop may weaken the interdomain interaction between Asp87$^{motif\text{-}A}$ and TM11, thus destabilizing the O state of *Hn*Spns. Acidic residues in the charge-relay network (e.g., Asp142) could also function as protonation switches (Figs. 9A and S6).[20]

Discussion

Using an integrated approach in lipid membranes, the extensive results presented above reveal new mechanistic details of *Hn*Spns as a close homolog of the human Spns proteins, including its conformational dynamics following protonation/deprotonation of glutamate 129 that is regulated by protonation state of aspartate 41 and substrate binding. Our comprehensive MD simulations implicate neutralization of the highly conserved Arg122 or Arg42 in this regulatory mechanism. Our results also indicate a noncanonical ligand-dependent alternating access in the absence of an obvious OF conformational state. While our IF model is similar to the X-ray structure, we have detected and generated a novel occluded state of *Hn*Spns in the membrane. The periplasmic salt bridge keeps the transporter in a closed conformation while the protonation-dependent conformational dynamics is significantly enhanced on the periplasmic side (Fig. 12A), providing a pathway for ligand exchange. Our DEER results in the presence of S1P (Fig. 7) indicated that protonation/deprotonation and not substrate binding drives the alternating access. Another distinctive feature of *Hn*Spns is the decoupling of the transmembrane protonation-dependent conformational changes that may be facilitated by hinged TM helices with more flexible periplasmic halves of the gating helices. Accordingly, the considerably lower periplasmic pK of conformational changes compared with the intracellular side implies the functional necessity for an inwardly directed proton gradient across the membrane.

Substrate polyspecificity and *Hn*Spns MDR activity. Our resistance assays to structurally unrelated antibiotics and antimicrobial compounds underscore the previously unknown role of *Hn*Spns and potentially human Spns proteins in MDR in addition to their sphingolipid transport and signaling activity. *Hn*Spns confers resistance to the same compounds as its close homolog MDR efflux transporter *Ms*Spns, highlighting their similar binding pocket properties.[43] High Spns2 and Spns3 expression is associated with poor prognosis in chemotherapy patients with acute myeloid leukemia.[8] Notably in Spns3, the substrate binding pocket is less charged, with the substrate binding residue arginine in TM1 being replaced with a tryptophan (Fig. 2A). Similar to other drug-proton antiporter 1 (DHA1) MFS transporters like MdfA, the observed flexibility of the protonated *Hn*Spns and a less hydrophilic binding cavity are crucial to populate transport-competent intermediates that fit several unrelated substrates.[46-49] Our resistance assays indicated differential resistance for the protonation-mimetic mutants with potential mechanistic implications (Fig. S2B, middle panels). As previously shown for MdfA, proton coupling can be different for neutral and charged substrates.[49-51] Likely, stabilization of the IF conformation by the D142N mutation abrogates efflux transport, and enduring protonation of the intracellular protonation master switch by E129Q mutation does not interfere with the transport and enhances the drug resistance. Single D41N mutation has no impact, but counteracts the effect of E129Q in double mutation. This may further highlight the regulatory effect of Asp41 on the IF-O conformational transition. Interestingly, for the MDR protein LmrP, binding of a negatively charged lipid in the binding pocket facilitates the substrate polyspecificity.[52] Similarly, in bacterial Spns proteins, binding of a lipid to the substrate binding residue arginine may assist their ability to bind a variety of neutral or positively-charged substrates.

Putative periplasmic path for proton translocation. Interestingly, both the refined IF and O models predict a tunnel in the NTD that extends from the periplasmic surface to Asp41 (Figs. 11B and 11C). At the end of the tunnel, a pocket of conserved polar residues including the intracellular protonation master switch Glu129, Arg122 and the putative substrate-binding residue Arg42, lies next to Asp41.[28] The top of the tunnel may be constricted by highly conserved residues $Trp206^{TM6}$ and $Phe56^{TM1/EH1-2}$ (Fig. 11D). Based on our DEER data on S57-L111 pair (TM1-TM3; Fig. S7), we predict these residues act as gatekeepers that sense the protonation-dependent structural rearrangements on the extracellular but not the intracellular side. Conservation analysis outlines a putative proton transfer pathway to the Asp41,[53] including conserved residues along TM3 (e.g., Trp102, Ser103, Thr106, Cys109 and Gly110) and TM6 (Trp206, Arg207, Val209, Phe210, Gly214 and Gly217). Protons can be released via water to the intracellular side from the main vestibule. But an alternate pathway from the periplasmic side to Asp41 and Glu129 via the main vestibule rather than through the putative tunnel may be only possible if intrinsic flexibility of the protonated

periplasmic side and particularly the putative periplasmic gate between TMs 5-8 allows such access (Fig. 12A).

Model of *Hn*Spns ligand-dependent alternating access. Based on the DEER-refined IF and O models of *Hn*Spns in lipid membranes and its local and global protonation-dependent conformational dynamics, we propose an antiport model of *Hn*Spns. This model identifies residues critical for protonation and its regulation, reveals how sequential protonation of these switches drive the conformational transitions, and suggests a mechanism of energy coupling to substrate transport and a putative path for proton translocation (Figs. 11 and 12). In the model, the stable resting state is IF (Fig. 12, steps 2 and 3), whereas the O (Fig. 12, steps 1 and 4) is of relatively high energy. In transition from the O state to IF (Fig. 12, step 1 to 2), Asp41 protonation, possibly through the putative periplasmic tunnel, promotes the Glu129 deprotonation and its neutralization by formation of a charge pair with Arg42. Subsequently, proton transfer to the acidic residues of the intracellular charge-relay network (e.g., Asp142) and its disruption stabilizes the IF conformation[20] suitable for substrate binding via intracellular side (Fig. 12, step 2). Proton transfer from Asp41 to Glu129 liberates Arg42 to bind substrates like S1P (Fig. 12, step 2 to 3). Substrate binding following Glu129 protonation triggers closing of the intracellular side and transition to a periplasmic flexible but closed conformation (Fig. 12, step 3 to 4). This enables the substrate release to the periplasmic leaflet, possibly through the putative periplasmic gate between TMs 5-8 (Fig. 12A) and restoration of the Arg42-Glu129 charge pair and Glu129 deprotonation. For an electrogenic substrate/nH^+ (with $n \geq 2$) transport, Glu129 is possibly re-protonated from the flexible periplasmic side (Fig. 12, step 4 to 1). Otherwise, proton transfer from Glu129 to the intracellular charge-relay network and protonation of Asp41 in step 4 are sufficient to directly reset the transporter to the IF conformation (Fig. 12, step 4 to 2).

The proposed transport model highlights distinct and novel aspects of alternating access in Spns proteins. Substantial similarities can also be detected to the proposed alternating access mechanisms in some other MFS transporters, including proton-coupled sugar acid and sugar symporters such as *E. coli* DgoT and XylE, and MDR efflux antiporters like MdfA and LmrP.[27,28,46,52] A similar regulatory effect of Asp41 protonation in *Hn*Spns is proposed for Asp27 in XylE and several of the conserved functional residues in the NTD of Spns proteins are also present in DgoT (Figs. 2A and 2C). Likewise, active transport in DgoT requires reversible protonation of both Asp46 and Glu133, corresponding residues to the Spns protonation switches.[28] A recent study of MdfA in lipid nanodiscs suggested a noncanonical alternating access involving a flexible, outward-closed/inward-closed conformation, similar to the occluded states we detected in *Hn*Spns.[46]

Among human Spns transporters, lysosomal Spns1 most likely functions as a symporter, removing degradation products, including sphingolipids, from the lysosomal lumen by coupling to the proton gradient across the lysosomal membrane. In contrast, Spns2 is predicted to function as a S1P efflux antiporter, given the inwardly directed H^+ gradient across the cell membrane. This strongly suggests that identical functional elements (e.g., protonation switches) can support substrate transport in opposite directions. Using a similar integrated approach to define the transport mechanism of other Spns family members and their prokaryotic homologs will identify the key commonalities and differences in their mechanisms, highlighting the mechanistic flexibility that enables their diverse function with transformative therapeutic potential.

Materials and Methods

Site-Directed Mutagenesis

Codon-optimized *Hn*Spns (GenScript) was cloned into pET19b vector encoding an N-terminal 10-His tag under control of an inducible T7 promoter. The five cysteine residues in *Hn*Spns were mutated (C98A, C109S, C132S, C442A, C457A) via site-directed mutagenesis with complementary oligonucleotide primers, yielding the CL protein. This construct was used as the template to introduce double-cysteine pairs and background mutations. Substitution mutations were generated using a single-step PCR in which the entire template plasmid was replicated from a single mutagenic primer. *Hn*Spns mutants were sequenced using both T7 forward and reverse

primers to confirm mutagenesis and the absence of aberrant changes. Mutants are identified by the native residue and primary sequence position followed by the mutant residue.

Expression, Purification, and Labeling of HnSpns

*Hn*Spns was expressed and purified using a similar protocol as previously published.[54] *Escherichia coli* C43 (DE3) cells (Sigma-Aldrich) were freshly transformed with pET19b vector encoding recombinant *Hn*Spns mutants. A transformant colony was used to inoculate Luria–Bertani (LB) media (Fisher Bioreagents) containing 0.1 mg/mL ampicillin (Gold Biotechnology), which was grown overnight (~15 h) at 34 °C and was subsequently used to inoculate 3-6 L of minimal medium A at a 1:50 dilution. Cultures were incubated while being shaken at 37°C until they reached an absorbance at 600 nm (Abs_{600nm}) of ~0.8, at which time *Hn*Spns expression was induced by the addition of 1 mM IPTG (Gold Biotechnology). The cultures were incubated overnight (~15 h) at 20°C and then harvested by centrifugation. Cell pellets were resuspended in resuspension buffer (20 mM Tris·HCl, pH 8.0, 20 mM NaCl, 30 mM imidazole, and 10% [vol/vol] glycerol) at 15 mL per liter of culture, including 10 mM DTT and 1 mM PMSF, and the cell suspension was lysed via sonication. Cell debris was removed by centrifugation at 9,000 × *g* for 10 min. Membranes were isolated from the supernatant by centrifugation at 200,000 × *g* for 1.5 h.

Membrane pellets were solubilized in resuspension buffer containing 5 mM LMNG (Anatrace) and 0.5 mM DTT and incubated on ice with stirring for 1 h. Insoluble material was cleared by centrifugation at 200,000 × *g* for 30 min. The cleared extract was bound to 1.0 mL (bed volume) of Ni-NTA Superflow resin (Qiagen) at 4 °C for 2 h. After washing with 10 bed volumes of buffer containing 30 mM imidazole, *Hn*Spns was eluted with buffer containing 300 mM imidazole.

Double-cysteine mutants were labeled with two rounds of 20-fold molar excess 1-oxyl-2,2,5,5-tetramethylpyrroline-3-methyl methanethiosulfonate (Enzo Life Sciences) per cysteine on ice in the dark over a 4-h period, after which the sample was kept on ice at 4 °C overnight (~15 h) to yield the spin label side chain R1. Unreacted spin label was removed by size exclusion chromatography over a Superdex200 Increase 10/300 GL column (GE Healthcare) into 50 mM Tris/MES, pH 7.5, 0.1 mM LMNG, and 10% (vol/vol) glycerol buffer. Peak fractions of purified *Hn*Spns were combined and concentrated using an Amicon Ultra 100,000 MWCO filter concentrator (Millipore), and the final concentration was determined by A_{280} measurement (ε = 95,340 $M^{-1}\cdot cm^{-1}$) for use in subsequent studies.

Reconstitution of HnSpns into Nanodiscs

1-palmitoyl-2-oleoyl-sn-glycero-3-phosphocholine (POPC), 1-palmitoyl-2-oleoyl-sn-glycero-3-phosphoethanolamine (POPE), 1-palmitoyl-2-oleoyl-sn-glycero-3-phospho-L-serine (POPS) and L-α-phosphatidylinositol (Liver, Bovine, POPI) (Avanti Polar Lipids) were combined in a 17.5:44:27.5:11 (mol/mol) ratio, dissolved in chloroform, evaporated to dryness on a rotary evaporator, and desiccated overnight under vacuum in the dark. The lipids were hydrated in 50 mM Tris/MES, pH 7.5, buffer to a final concentration of 20 mM, homogenized by freezing and thawing for 10 cycles, and stored in small aliquots at −80 °C. MSP1D1E3 was expressed and purified as previously described[55] and dialyzed into 50 mM Tris/MES, pH 7.5, buffer. MSP1D1E3 was concentrated using a 10,000 MWCO filter concentrator and the final protein concentration was determined by A_{280} measurement (ε = 29,910 $M^{-1}\cdot cm^{-1}$).

For reconstitution into nanodiscs, spin-labeled double-cysteine mutants in LMNG micelles were mixed with lipid mixture, MSP1D1E3, and sodium cholate in the following molar ratios: lipid:MSP1D1E3, 50:1; MSP1D1E3:*Hn*Spns, 10:1; and LMNG+cholate:lipid, 3:1. Reconstitution reactions were mixed at 4 °C for 1 h. Detergent was removed from the reaction by addition of 0.1 g/mL Biobeads (Bio-Rad) and incubation at 4°C for 1 h. This was followed by another addition of 0.1 g/mL Biobeads with 1-h incubation, after which 0.2 mg/mL Biobeads were added and mixed overnight. The next day, 0.2 mg/mL Biobeads were added and mixed for 1 h. The reaction was filtered using a 0.45-μm filter to remove Biobeads. Full nanodiscs were separated from empty nanodiscs by size exclusion chromatography into 50 mM Tris/MES, pH 7.5, and 10% (vol/vol) glycerol buffer. The *Hn*Spns-containing nanodiscs were concentrated using Amicon ultra 100,000 MWCO filter concentrator, and then characterized using SDS/PAGE to verify reconstitution and estimate reconstitution efficiency. The concentration of spin-labeled mutants in nanodiscs was determined as described previously by comparing the intensity of the integrated continuous-wave

electron paramagnetic resonance (CW-EPR) spectrum to that of the same mutant in detergent micelles.[56]

CW-EPR and DEER Spectroscopy

CW-EPR spectra of spin-labeled *Hn*Spns samples were collected at room temperature on a Bruker EMX spectrometer operating at X-band frequency (9.5 GHz) using 10-mW incident power and a modulation amplitude of 1.6 G. DEER spectroscopy was performed on an Elexsys E580 EPR spectrometer operating at Q-band frequency (33.9 GHz) with the dead-time free four-pulse sequence at 83 K.[57] Pulse lengths were 28 ns ($\pi/2$) for the probe pulse and 44 ns for the pump pulse. The frequency separation was 63 MHz. To ascertain the role of H^+, samples were titrated to pH 4 and 9 with empirically determined amounts of 1 M citric acid and 1 M Tris, respectively, and confirmed by pH microelectrode measurement. The substrate-bound state was generated by addition of 1 mM S1P at pH 7.5. Samples for DEER analysis were cryoprotected with 24% (vol/vol) glycerol and flash-frozen in liquid nitrogen.

Primary DEER decays were analyzed using home-written software operating in the Matlab (MathWorks) environment as previously described.[58] Briefly, the software carries out global analysis of the DEER decays obtained under different conditions for the same spin-labeled pair. The distance distribution is assumed to consist of a sum of Gaussians, the number and population of which are determined based on a statistical criterion. The generated confidence bands were determined from calculated uncertainties of the fit parameters. We also analyzed DEER decays individually and found that the resulting distributions agree with those obtained from global analysis. Comparison of the experimental distance distributions with the *Hn*Spns crystal structure (PDB code 6E9C) using a rotamer library approach was facilitated by the MMM software package.[59] Rotamer library calculations were conducted at 298 K. For a few samples, a noticeable change in the intermolecular background was observed in nanodiscs at pH 4, giving rise to a steep decay relative to higher pH. This reversible change in background is associated with reversible clustering of individual nanodisc particles.[54]

Molecular Dynamics

System Setup

The crystal structure of *Hn*Spns in the IF conformation (PDB code 6E9C) was prepared for MD simulations. Missing side chains and hydrogen atoms were added to the structure using the PSFGEN plugin of VMD.[60] Neutral N-terminal and C-terminal caps were added to the beginning and end of the polypeptide chain, respectively, followed by addition of a disulfide bond between residues Cys442 and Cys457 using PSFGEN. The protonation state of all titratable residues was estimated with PROPKA.[61] The protein was embedded in a lipid bilayer generated by CHARMM-GUI,[62] followed by removing the steric clashes between the protein and lipid molecules. Orientations of Proteins in Membranes (OPM) database was used to obtain the orientation of the protein in the bilayer.[63] The same lipid composition as lipid nanodiscs was employed in MD simulations. The complex was subsequently solvated in VMD (system size: 233,000 atoms).

Simulation Conditions

All simulations were performed employing the fully atomistic CHARMM36m[64] and CHARMM36 force fields for the protein and lipids, respectively. The TIP3P model was used for water molecules. The systems were simulated with NAMD2[65] using the following parameters. For the short-range, non-bonded interactions a 12-Å cutoff was employed, with switching starting at 10 Å. The particle mesh Ewald (PME) algorithm was employed to calculate long-range electrostatic interactions with a grid density of 1 $Å^{-1}$, and a PME interpolation order of 6. Bonds involving hydrogen atoms were kept fixed employing the SHAKE algorithm. Temperature was sustained at 310 K using Langevin thermostat with a damping coefficient of 1.0 ps^{-1}. Pressure was kept at 1 atm by the Nosé-Hoover Langevin piston barostat with period and decay of 100 and 50 fs, respectively. All simulations were performed in a flexible cell allowing the dimensions of the periodic cell to change independently while keeping the cell aspect ratio in the *xy* plane (membrane plane) constant. A 2-fs timestep was used in all simulations. Lennard-Jones and PME forces were updated at one and two timesteps, respectively. Three different sets of simulations were conducted to

investigate: 1) proton-coupled conformational changes of the *Hn*Spns in the IF conformation, 2) capturing a stable O conformation of the transporter, and 3) structural refinement of the IF and O conformations by incorporating the experimental DEER data.

Equilibrium MD to Investigate Proton-coupled Conformational Changes of HnSpns

Four different systems were simulated to investigate the coupling of the two putative proton-binding sites (Asp41 and Glu129) to the conformational changes of the transmembrane region of *Hn*Spns. These four systems cover all the combinations of different protonation states of the two titratable residues. To improve statistics, each of the four systems was replicated three times and simulated for 500 ns (3×4×500 ns = 6 μs).

Capturing a Stable O Conformation of HnSpns Through Combined Non-equilibrium and Equilibrium MD

Well-tempered metadynamics simulation[44] was employed to capture the O *Hn*Spns by sampling a phase-space containing two orientation-based collective variables (CVs), denoted as α and β, describing the cytoplasmic and extracellular opening/closing of the transmembrane region of the transporter, respectively (Fig. S13A). The two angles were calculated by first splitting the N- and C-domain of the transporter into two equal segments representing the intracellular and extracellular halves. α was defined as the angle between the center of mass of three different parts: 1) the intracellular half of N-domain, 2) the extracellular half of the protein (including both the N- and C-domains), and 3) the intracellular half of C-domain. β is the angle between: 1) the extracellular half of N-domain, 2) the intracellular half of the protein (including both the N- and C-domains), and 3) the extracellular half of C-domain. The metadynamics simulation was performed for 200 ns from which a putative O conformation was obtained. This conformation was further stabilized by forming salt-bridges at the extracellular and intracellular gates, namely Arg289-Asp60 and Arg390-Asp142, respectively (Fig. S13E). The stability of the formed salt bridges and the intracellular closure was confirmed through a 500-ns equilibrium simulation.

DEER-Guided Refinement of the IF and O Conformations Through reMD Simulations

The DEER data was used to refine both the IF and O structures employing restrained-ensemble MD (reMD).[40] Prior to the simulations, dummy spin labels (OND), were added to the sites of interest using PSFGEN. Pairwise distances between the dummy spin labels were harmonically restrained to the experimental values with a force constant of 10 kcal/mol/Å^2 and then simulated for 1 ns. REMD simulations were performed using the same parameters described in *Simulation Conditions* except for using a 1-fs timestep for integration.

Thermal Stability Analysis

Structural integrity of the spin-labeled DEER and protonation mimetic mutants in LMNG micelles and lipid nanodiscs were monitored using CD spectroscopy. Protein samples were diluted to 0.1 mg/mL in 10 mM sodium phosphate, pH 7.5 buffer (CD buffer) with or without 0.1 mM LMNG, for detergent micelles and nanodiscs, respectively. CD measurements were recorded on an Applied Photophysics Chirascan V100. Thermal denaturation was continuously monitored every 0.5°C at 222 nm from 10 to 95°C with a 0.2°C tolerance and corrected with the same measurements using CD buffer with LMNG or empty nanodiscs. Melting temperature (T_m) was determined by a non-linear least squares analysis of each individual curve in OriginPro (OriginLab).

Drug Resistance Assay

Resistance to toxic concentrations of capreomycin, rifampicin and ethidium bromide, conferred by *Hn*Spns WT and its mutants was carried out as previously described.[42] *Escherichia coli* BL21 (DE3) were transformed with empty pET19b vector, pET19b encoding *Hn*Spns WT, or mutant *Hn*Spns. A dense overnight culture from a single transformant was used to inoculate 10 mL of LB broth containing 0.1 mg/mL ampicillin to a starting Abs_{600} of 0.0375. Cultures were grown to Abs_{600} of 0.3 at 37°C and expression of the encoded construct was induced with 1.0 μM IPTG (Gold Biotechnology). Expression was allowed to continue at 37°C for 2 h, after which the Abs_{600} of the cultures was adjusted to 0.5. The cells were then used to inoculate (1:20 dilution, starting Abs_{600} = 0.025) a sterile 96-well microplate (Greiner) containing 50% LB broth, 0.1 mg/mL ampicillin, and

2.5-70 µg/mL rifampicin or 9-70 µg/mL of capreomycin/ethidium bromide. Microplates were incubated at 37°C with shaking at 250 rpm for 2 to 8 h. The cell density (Abs_{600}) was measured every 2 h on a SpectraMax i3 microplate reader and normalized to the 0 µg/mL drug well to obtain a relative absorbance, which accounts for growth behavior of the vector, WT, CL and other variants in the absence of drug. Each data point was performed in triplicate, and the experiments were repeated.

Acknowledgments

The authors wish to thank Mr. Brant Swiney for his assistance in creating all *Hn*Spns mutants and protein expression and purification. We thank Dr. Joel Eissenberg for critical reading and editing of the manuscript and Dr. Edwin Antony and Ms. Sahiti Kuppa for assistance on the CD analyses. This work was supported by a Lottie C Hardy Foundation grant (to R.D.). The molecular dynamics studies were supported by NIH grant P41-104601 (to E.T.) and computing resources provided by XSEDE (grant No. MCA06N060 to E.T.) and by Microsoft Azure.

Author Contributions

R.D. and E.T. designed the experiments. R.D. and S.G. purified the mutants and reconstituted in nanodiscs. R.D. performed the EPR experiments and analyzed the data. A.R. and S.D.G. performed and analyzed molecular dynamics simulations and modeling. S.G. performed thermal stability analyses and cell growth assays. R.D., A.R. and S.D.G. wrote the paper with input from all authors.

Competing Interests

The authors declare no competing interests.

References

1. Spiegel, S., et al., New insights into functions of the sphingosine-1-phosphate transporter SPNS2. Journal of Lipid Research, 2019. 60(3): 484-489.
2. Newton, J., et al., Revisiting the sphingolipid rheostat: Evolving concepts in cancer therapy. Experimental Cell Research, 2015. 333(2): 195-200.
3. Spiegel, S. and S. Milstien, Sphingosine-1-phosphate: An enigmatic signalling lipid. Nature Reviews Molecular Cell Biology, 2003. 4(5): 397-407.
4. Kunkel, G.T., et al., Targeting the sphingosine-1-phosphate axis in cancer, inflammation and beyond. Nature Reviews Drug Discovery, 2013. 12(9): 688-702.
5. Hisano, Y., et al., The sphingosine 1-phosphate transporter, SPNS2, functions as a transporter of the phosphorylated form of the immunomodulating agent FTY720. Journal of Biological Chemistry, 2011. 286(3): 1758-1766.
6. Zhu, X., et al., Biological function of SPNS2: From zebrafish to human. Molecular Immunology, 2018. 103: 55-62.
7. Fang, L., et al., Spinster homolog 2 in cancers, its functions and mechanisms. Cellular Signalling, 2021. 77: 109821.
8. Huang, W., et al., Prognostic significance of Spinster homolog gene family in acute myeloid leukemia. Journal of Cancer, 2020. 11(15): 4581-4588.
9. Nijnik, A., et al., The role of sphingosine-1-phosphate transporter Spns2 in immune system function. Journal of Immunology, 2012. 189(1): 102-111.
10. Cyster, J.G. and S.R. Schwab, Sphingosine-1-phosphate and lymphocyte egress from lymphoid organs. Annual Review of Immunology, 2012; 30: 69-94.
11. Mendoza, A., et al., The transporter Spns2 is required for secretion of lymph but not plasma sphingosine-1-phosphate. Cell Reports, 2012. 2(5): 1104-1110.
12. Nagahashi, M., et al., Spns2, a transporter of phosphorylated sphingoid bases, regulates their blood and lymph levels, and the lymphatic network. The FASEB Journal, 2013. 27(3): 1001-1011.
13. Donoviel, M.S., et al., Spinster 2, a sphingosine-1-phosphate transporter, plays a critical role in inflammatory and autoimmune diseases. The FASEB Journal, 2015. 29(12): 5018-5028.
14. van der Weyden, L., et al., Genome-wide in vivo screen identifies novel host regulators of metastatic colonization. Nature, 2017. 541(7636): 233-236.
15. Zhang, X.C., et al., Energy coupling mechanisms of MFS transporters. Protein Science, 2015. 24(10): 1560-1579.
16. Madej, M.G., et al., Evolutionary mix-and-match with MFS transporters. Proceedings of the National Academy of Sciences of the USA, 2013. 110(15): 5870-5874.
17. Radestock, S., and L.R. Forrest, The alternating-access mechanism of MFS transporters arises from inverted-topology repeats. Journal of Molecular Biology, 2011. 407(5): 698-715.
18. Heng, J., et al., Substrate-bound structure of the *E. coli* multidrug resistance transporter MdfA. Cell Research, 2015. 25(9): 1060-1073.
19. Jardetzky, O., Simple allosteric model for membrane pumps. Nature, 1966. 211: 969-970.
20. Martens, C., et al., Direct protein-lipid interactions shape the conformational landscape of secondary transporters. Nature Communications, 2018. 9: 4151.

21. Huang. Y., et al., Structure and mechanism of the glycerol-3-phosphate transporter from *Escherichia coli*. Science, 2003. 301: 616-620.

22. Abramson, J., S. Iwata, and H.R. Kaback, Lactose permease as a paradigm for membrane transport proteins. Molecular Membrane Biology, 2004. 21(4): 227-236.

23. Law, C.J., P.C. Maloney, and D.N. Wang, Ins and outs of major facilitator superfamily antiporters. Annual Review of Microbiology, 2008. 62: 289-305.

24. Jumper. J., et al., Highly accurate protein structure prediction with AlphaFold. Nature, 2021. 596(7873): 583-589.

25. Zhou, F., et al., Crystal structure of a bacterial homolog to human lysosomal transporter, spinster. Science Bulletin, 2019. 64: 1310-1317.

26. Jiang, D., et al., Structure of the YajR transporter suggests a transport mechanism based on the conserved motif A. Proceedings of the National Academy of Sciences of the USA, 2013. 110(36): 14664-14669.

27. Wisedchaisri, G., et al., Proton-coupled sugar transport in the prototypical major facilitator superfamily protein XylE. Nature Communications, 2014. 5: 4521.

28. Leano, J.B., et al., Structures suggest a mechanism for energy coupling by a family of organic anion transporters. PLoS Biology, 2019. 17(5): e3000260.

29. Schiemann, O., et al., Benchmark Test and Guidelines for DEER/PELDOR Experiments on Nitroxide-Labeled Biomolecules. Journal of the American Chemical Society, 2021. 143(43): 17875-17890.

30. Claxton, D.P., et al., Navigating membrane protein structure, dynamics, and energy landscapes using spin labeling and EPR spectroscopy. Methods in Enzymology, 2015. 564: 349-387.

31. Dastvan, R., et al., Protonation-dependent conformational dynamics of the multidrug transporter EmrE. Proceedings of the National Academy of Sciences of the USA, 2016. 113(5): 1220-1225.

32. Verhalen, B., Dastvan R., et al., Energy transduction and alternating access of the mammalian ABC transporter P-glycoprotein. Nature, 2017. 543(7647): 738-741.

33. Dastvan, R., et al., Mechanism of allosteric modulation of P-glycoprotein by transport substrates and inhibitors. Science, 2019. 364(6441): 689-692.

34. Moradi, M., G. Enkavi, and E. Tajkhorshid, Atomic-level characterization of transport cycle thermodynamics in the glycerol-3-phosphate: phosphate antiporter. Nature Communications, 2015. 6(1): 1-11.

35. Moradi, M., and E. Tajkhorshid, Mechanistic picture for conformational transition of a membrane transporter at atomic resolution. Proceedings of the National Academy of Sciences, 2013. 110(47): 18916-18921.

36. Moradi, M., and E. Tajkhorshid, Computational recipe for efficient description of large-scale conformational changes in biomolecular systems. Journal of Chemical Theory and Computation, 2014. 10(7): 2866-2880.

37. Li, J., Z. Zhao, and E. Tajkhorshid, Locking two rigid-body bundles in an outward-facing conformation: the ion-coupling mechanism in a LeuT-fold transporter. Scientific Reports, 2019. 9(1): 19479.

38. Sauer, D.B., et al., Structural basis for the reaction cycle of DASS dicarboxylate transporters. eLife, 2020. 9: e61350.

39. Chen, I., et al., Glutamate transporters have a chloride channel with two hydrophobic gates. Nature, 2021. 591(7849): 327-331.

40. Islam, S.M., et al., Structural refinement from restrained-ensemble simulations based on EPR/DEER data: Application to T4 Lysozyme. Journal of Physical Chemistry B, 2013. 117(17): 4740-4754.

41. Miles, A.J. and B.A. Wallace, Circular dichroism spectroscopy of membrane proteins. Chemical Society Reviews, 2016. 45(18): 4859-4872.

42. Jagessar, K.L., H.S. Mchaourab, and D.P. Claxton, The N-terminal domain of an archaeal multidrug and toxin extrusion (MATE) transporter mediates proton coupling required for prokaryotic drug resistance. The Journal of Biological Chemistry, 2019. 294(34): 12807-12814.

43. Zhang, Z., R. Wang, and J. Xie, *Mycobacterium smegmatis MSMEG_3705* encodes a selective major facilitator superfamily efflux pump with multiple roles. Current Microbiology, 2015. 70(6): 801-809.

44. Barducci, A., G. Bussi, and M. Parrinello, Well-tempered metadynamics: a smoothly converging and tunable free-energy method. Physical review letters, 2008. 100(2): 020603.

45. Gordon, J.C., et al., H++: a server for estimating pKas and adding missing hydrogens to macromolecules. Nucleic Acids Research, 2005. 33: W368–W371.

46. Yardeni, E.H., et al., The multidrug transporter MdfA deviates from the canonical model of alternating access of MFS transporters. Journal of Molecular Biology, 2020. 432(20): 5665-5680.

47. Kim, J., et al., Structural insights into transporter-mediated drug resistance in infectious diseases. Journal of Molecular Biology, 2021. 433(16): 167005.

48. Drew, D., et al., Structures and general transport mechanisms by the major facilitator superfamily (MFS). Chemical Reviews, 2021. 121(9): 5289-5335.

49. Fluman, N. and E. Bibi, Bacterial multidrug transport through the lens of the major facilitator superfamily. Biochimica et Biophysica Acta, 2009. 1794(5): 738-747.

50. Sigal, N., et al., The secondary multidrug/proton antiporter MdfA tolerates displacements of an essential negatively charged side chain. The Journal of Biological Chemistry, 2009. 284(11): 6966-6971.

51. Fluman, N., et al., Dissection of mechanistic principles of a secondary multidrug efflux protein. Molecular Cell, 2012. 47(5): 777-787.

52. Debruycker, V., et al., An embedded lipid in the multidrug transporter LmrP suggests a mechanism for polyspecificity. Nature Structural and Molecular Biology, 2020. 27(9): 829-835.

53. Celniker, G., et al., ConSurf: Using evolutionary data to raise testable hypotheses about protein function. Israel Journal of Chemistry (2013). doi:10.1002/ijch.201200096.

54. Jagessar, K.L., et al., Sequence and structural determinants of ligand-dependent alternating access of a MATE transporter. Proceedings of the National Academy of Sciences, 2020. 117(9): 4732-4740.

55. Mishra, S., et al., Conformational dynamics of the nucleotide binding domains and the power stroke of a heterodimeric ABC transporter. Elife, 2014. 3, e02740.

56. Zou, P. and H.S. Mchaourab, Increased sensitivity and extended range of distance measurements in Spin-labeled membrane proteins: Q-band double electron-electron resonance and nanoscale bilayers. Biophysical Journal, 2010. 98(6): L18-L20.

57. Jeschke, G., DEER distance measurements on proteins. Annual Review of Physical Chemistry, 2012. 63: 419-446.

58. Hustedt, E.J., R.A. Stein, and H.S. Mchaourab, Protein functional dynamics from the rigorous global analysis of DEER data: Conditions, components, and conformations. The Journal of General Physiology, 2021. 153(11): e201711954.

59. Polyhach, Y., E. Bordignon, and G. Jeschke, Rotamer libraries of spin labelled cysteines for protein studies. Physical Chemistry Chemical Physics, 2011. 13: 2356-2366.

60. Humphrey, W., A. Dalke, and K. Schulten, VMD: visual molecular dynamics. Journal of Molecular Graphics, 1996. 14(1): 33-38, 27-28.

61. Olsson, M.H.M., et al., PROPKA3: consistent treatment of internal and surface residues in empirical pKa predictions. Journal of Chemical Theory and Computation, 2011. 7(2): 525-537.

62. Jo, S., et al., CHARMM-GUI membrane builder for mixed bilayers and its application to yeast membranes. Biophysical Journal, 2009. 97(1): 50-58.

63. Lomize, M.A., et al., OPM: orientations of proteins in membranes database. Bioinformatics, 2006. 22(5): 623-625.

64. Huang, J., et al., CHARMM36m: an improved force field for folded and intrinsically disordered proteins. Nature Methods, 2017. 14(1): 71-73.

65. Phillips, J.C., et al., Scalable molecular dynamics with NAMD. Journal of Computational Chemistry, 2005. 26(16): 1781-1802.

Figures and Tables

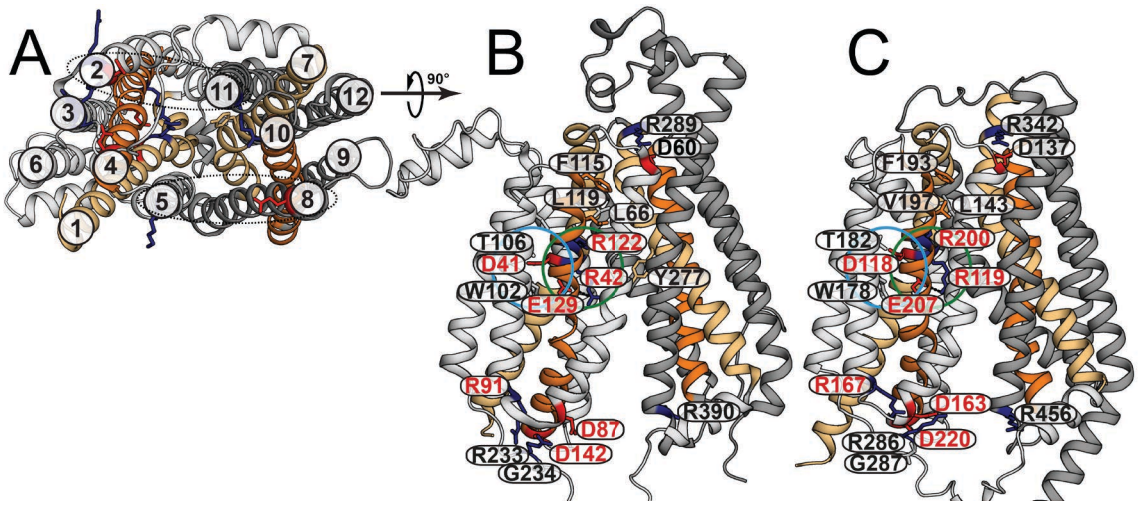

Figure 1. The architecture of the Spns proteins. (A) Cytoplasmic view of the *Hn*Spns crystal structure (Protein Data Bank (PDB) code 6E9C) in the IF state with the NTD and CTD colored in light and dark gray, respectively. (B) Membrane view of *Hn*Spns with the positions of conserved and functional residues labeled. Symmetry-related TM helices 1/7 and 4/10 are colored with light and dark orange, respectively. (C) The AlphaFold model of the human Spns2.

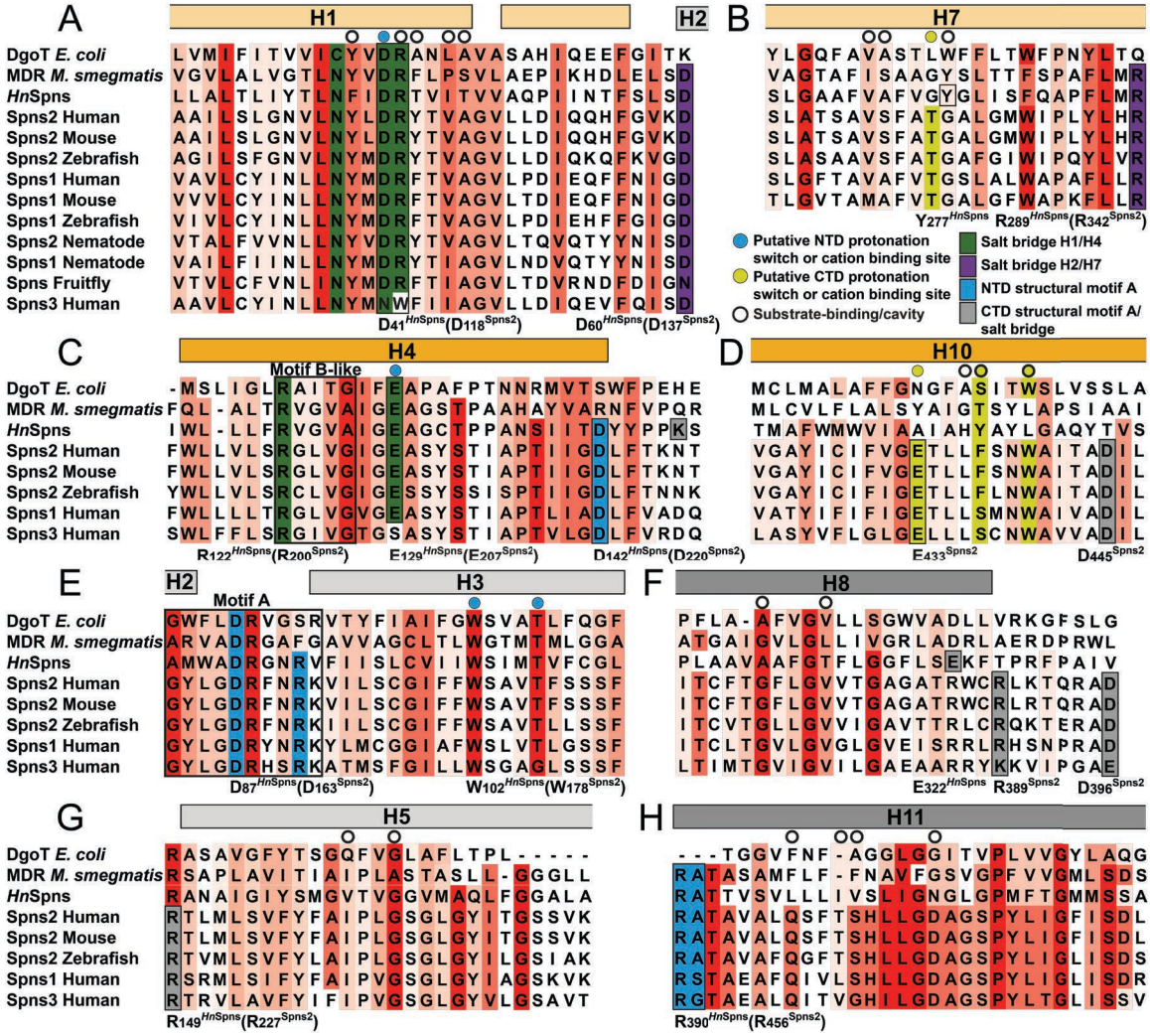

Figure 2. Sequence alignment of spinster family proteins and their bacterial homologs, the *M. smegmatis* MDR transporter (*Ms*Spns), and the *E. coli* MFS homolog DgoT. The putative substrate and cation binding site residues are indicated by circles above the sequence alignment. Residues are colored according to sequence conservation with different shades of red. Functional residues are colored differently.

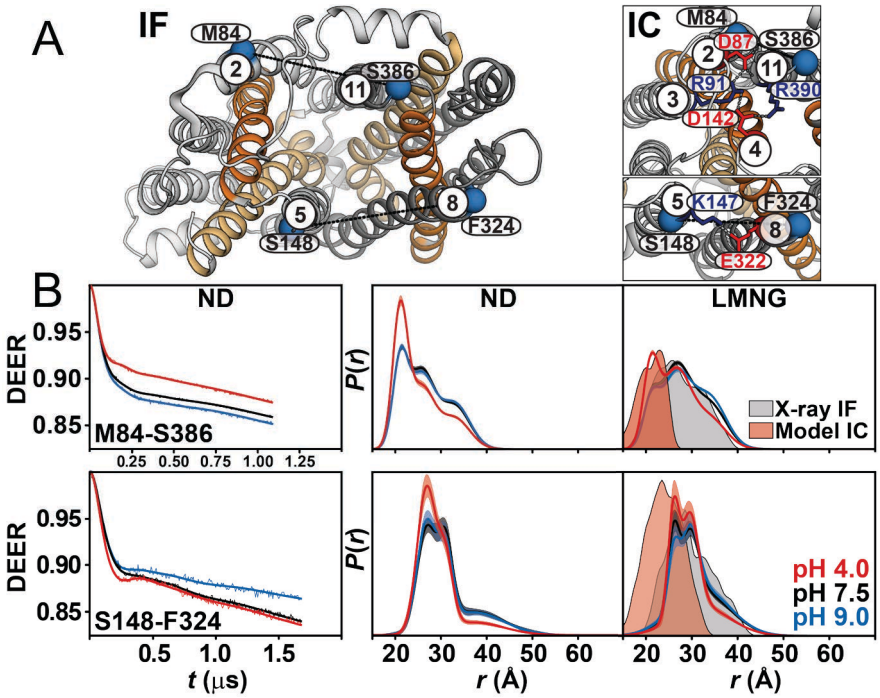

Figure 3. Protonation closes the intracellular side of *Hn*Spns. (A) Spin label pairs for DEER distance measurements on gating helices across the N- and C-lobes are depicted on the intracellular side of the IF crystal structure and an intracellular-closed (IC) model. (B) Raw DEER decays and fits (left) are presented for the experimentally-determined distributions *P*(*r*) in lipid nanodiscs (middle) and compared to distance distributions in LMNG micelles (right). The predicted distributions derived from the IF crystal structure and the IC model are shaded gray and red, respectively.

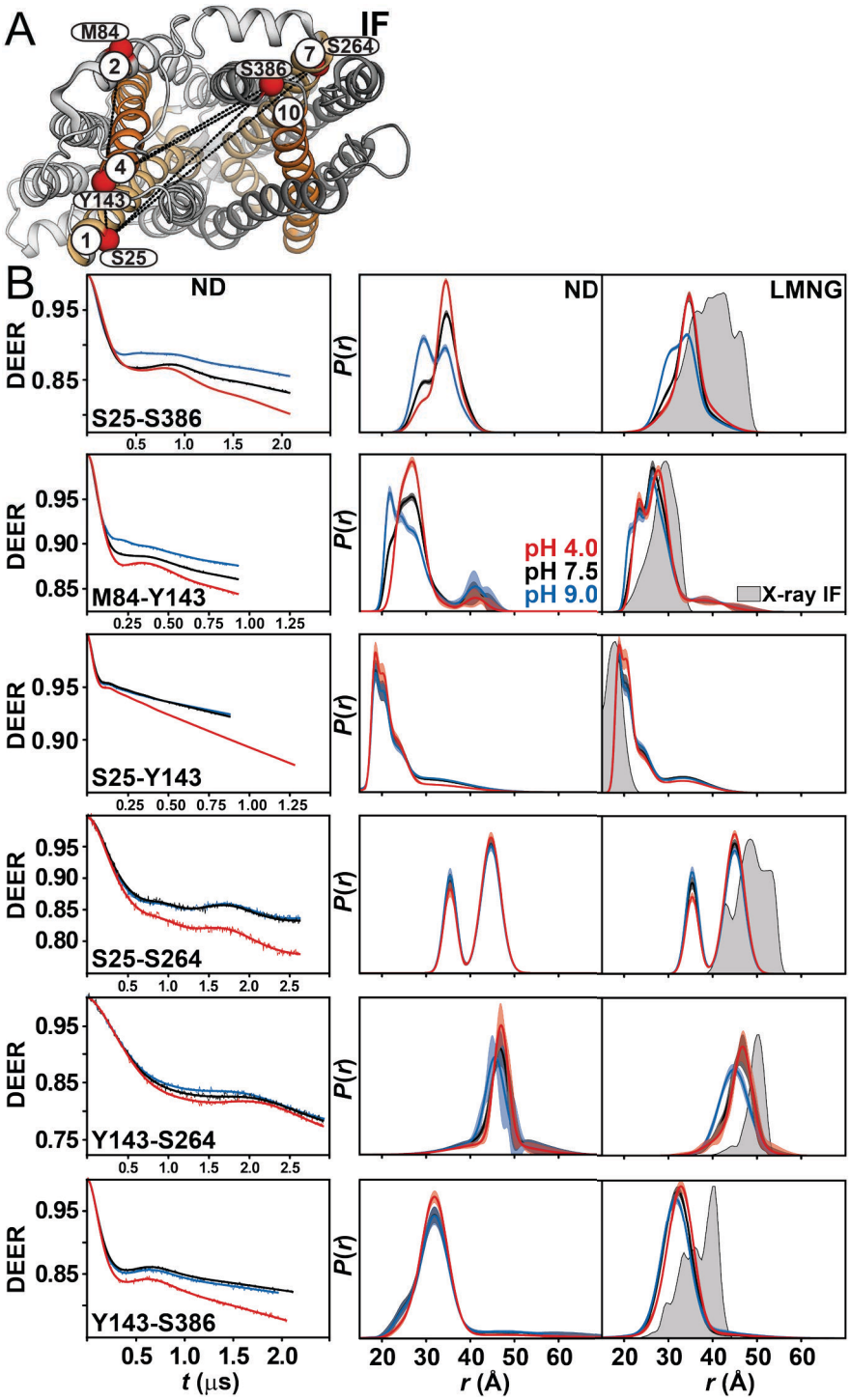

Figure 4. Protonation induces distinct rearrangements for cavity helices on the intracellular side. (A) Spin label pairs on cavity helices are depicted on the intracellular side of the IF crystal structure. (B) Raw DEER decays and fits (left) are presented for the distance distributions *P*(*r*) in lipid nanodiscs (middle) and compared with distributions in LMNG micelles (right). The predicted distributions derived from the IF crystal structure are shaded gray.

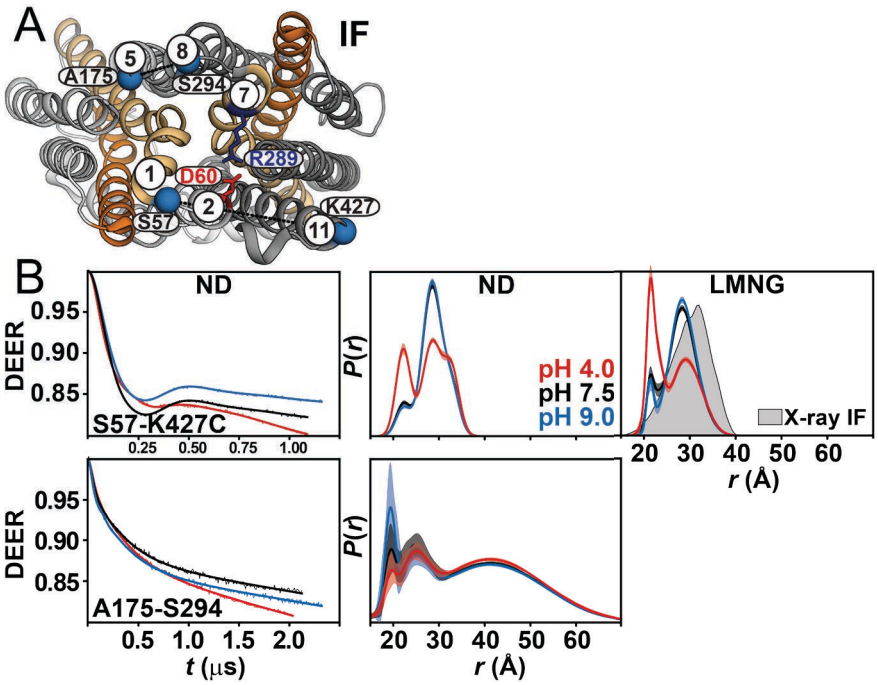

Figure 5. Enhanced flexibility of the periplasmic side of *Hn*Spns induced by protonation, with a lateral opening between TMs 5 and 8. (A) Spin label pairs on gating helices across the N- and C-lobes are depicted on the periplasmic side. (B) Raw DEER decays and fits (left) are presented for the distance distributions *P*(*r*) in lipid nanodiscs (middle) and compared to distance distributions in LMNG micelles (right). The predicted distributions derived from the IF crystal structure are shaded gray.

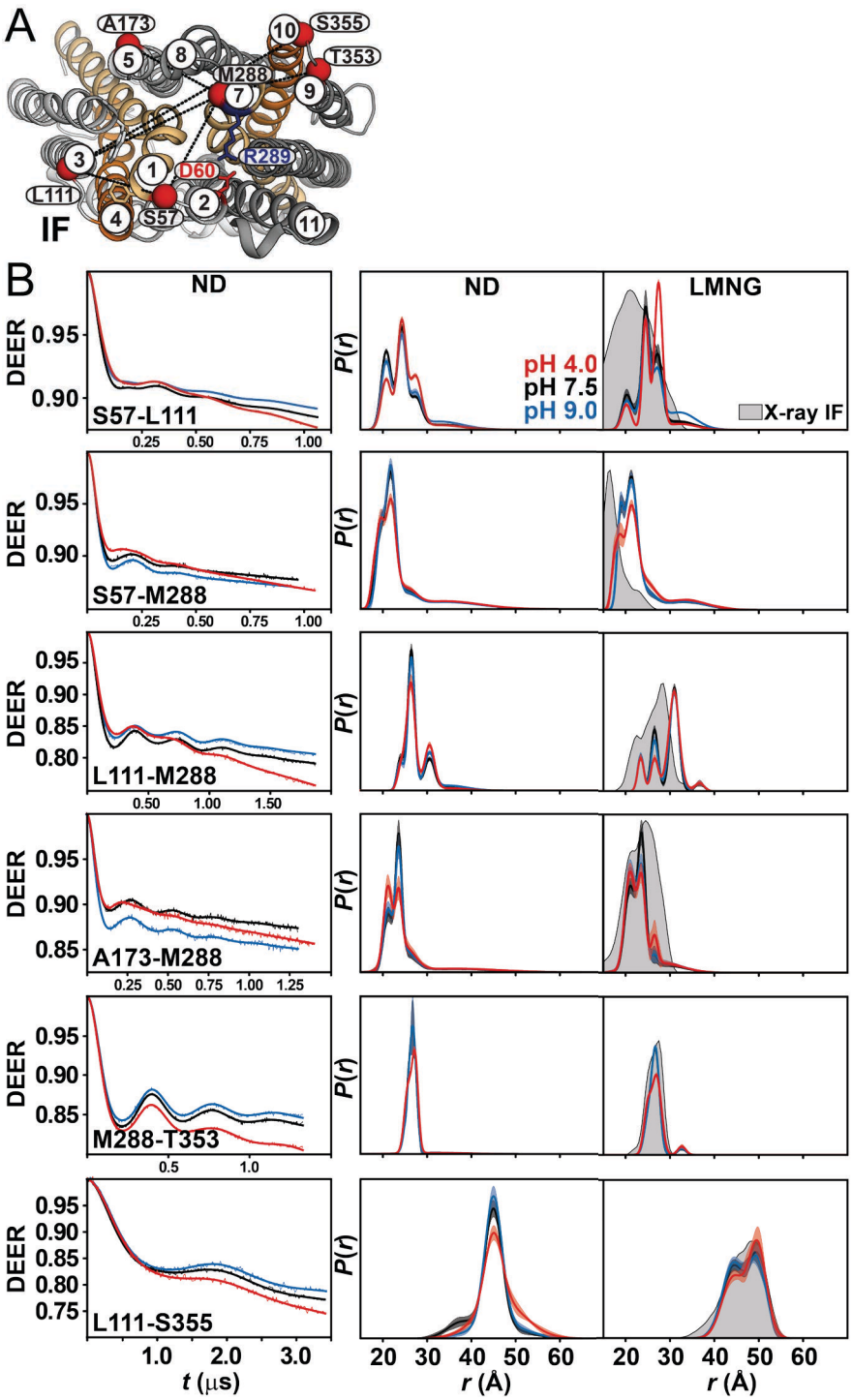

Figure 6. Protonation stabilizes an outward-closed conformation. (A) Spin label pairs are depicted on the periplasmic side of the IF crystal structure. A salt bridge between Asp60 and Arg289 keeps the transporter in a closed conformation. (B) Raw DEER decays and fits (left) are presented for the distance distributions *P*(*r*) in lipid nanodiscs (middle) and compared to distance distributions in LMNG micelles (right). The predicted distributions derived from the IF crystal structure are shaded gray.

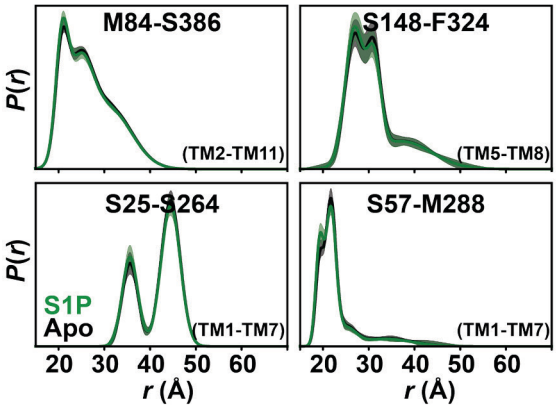

Figure 7. S1P binding to *Hn*Spns in lipid nanodiscs does not induce major conformational changes but rather a slight shift to shorter distances. The distance distributions *P*(*r*) in lipid nanodiscs (pH 7.5) are shown in the apo state (black) and with S1P (green).

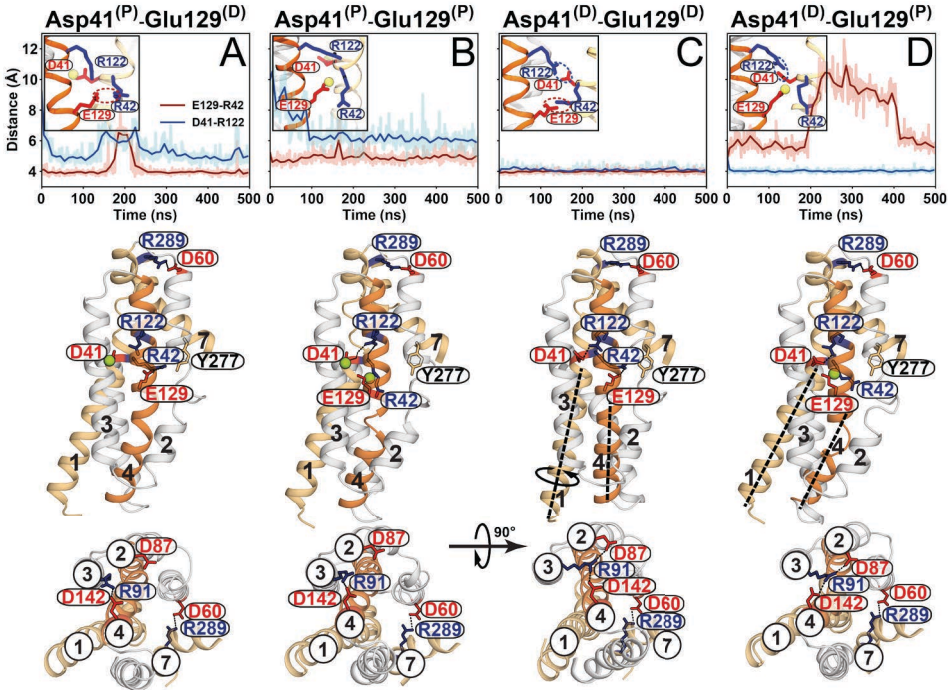

Figure 8. MD simulations of the IF *Hn*Spns structure in lipids revealed that Glu129 protonation-dependent liberation of the substrate binding residue Arg42 strongly depends on the protonation state of the Asp41. Time series of distances between the side chains of Glu129-Arg42 (red) and Asp41-Arg122 (blue) are presented to monitor proximity and formation of these salt bridges as a function of protonation states of Asp41 and Glu129 (top panels, Fig. S5). Only with Asp41 deprotonated and interacting with Arg122, can Arg42 completely disengage from protonated Glu129 and bind substrate (panel D). The Asp41 and Glu129 protonation-dependent conformational changes in TMs 1 and 4 could occur independent of the periplasmic salt bridge stabilizing the extracellular-closed conformation (middle panels). Upon protonation of Asp41, the charge relay network between Asp87-Arg91-Asp142, essential for the conformational transition cannot be formed, thereby stabilizing the IF conformation (A and B, lower panels).

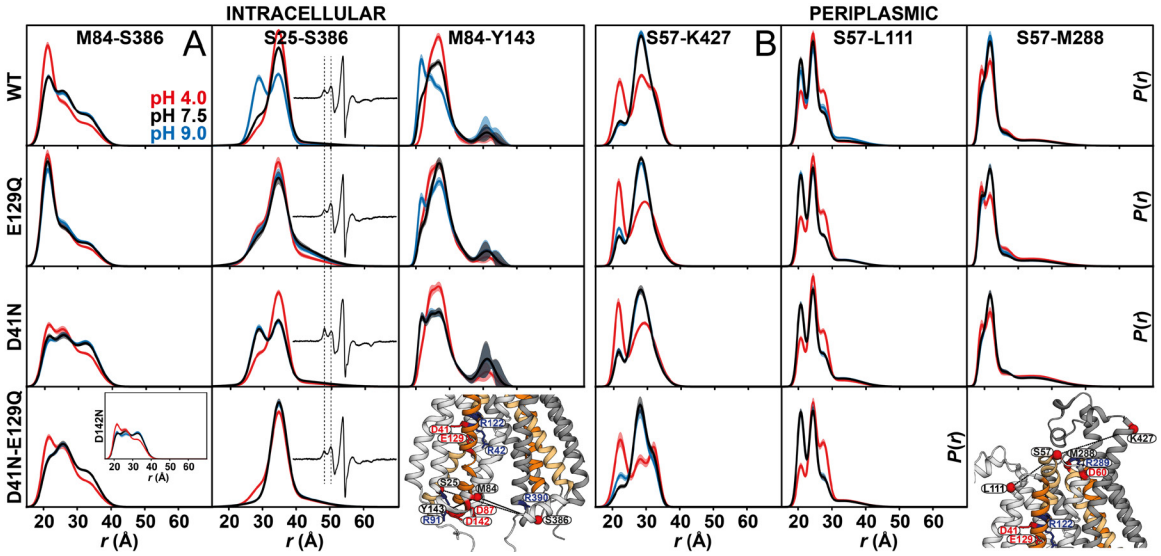

Figure 9. Independent proton-coupled conformational changes on the two sides of *Hn*Spns in lipid nanodiscs. Effect of protonation-mimetic mutation of acidic residues on conformational states in equilibrium on the (A) intracellular and (B) periplasmic side (Figs. S6-S9). The single (E129Q, D41N, D142N) or double (D41N/E129Q) mutations were combined with the double-cysteine mutations. DEER experiments in the presence of these mutations support the results of the MD simulations and reveal that Asp41 protonation has the opposite effect from that of Glu129 on the intracellular side conformational changes and the periplasmic side remains mostly invariant in response to these mutations.

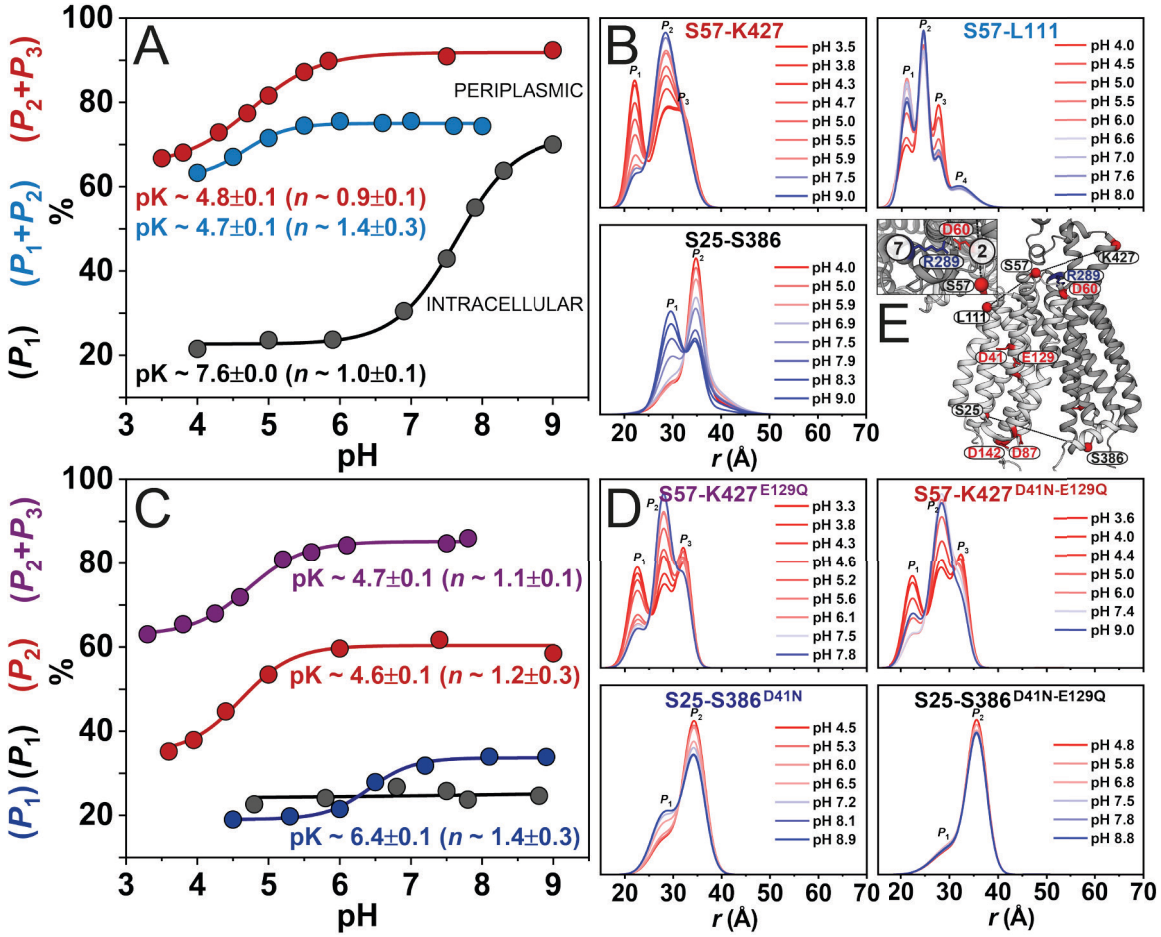

Figure 10. Intracellular and periplasmic sides of *Hn*Spns sense differently its protonation state. (A, B) Distance distributions of periplasmic (S57-K427 and S57-L111) and intracellular (S25-S386) pairs were obtained at different pH values in lipid nanodiscs (Fig. S10) and LMNG micelles (Fig. S11). The variation in population of rising or decreasing distance peaks as a function of pH was used to estimate the pK value for conformational changes in *Hn*Spns on both membrane sides. (C, D) Effect of protonation-mimetic mutation of acidic residues on pK values for conformational changes. The D41N-E129Q double mutation completely abrogates conformational changes on the intracellular side with periplasmic side mainly unaffected, further demonstrating the decoupling of transmembrane protonation-dependent conformational changes.

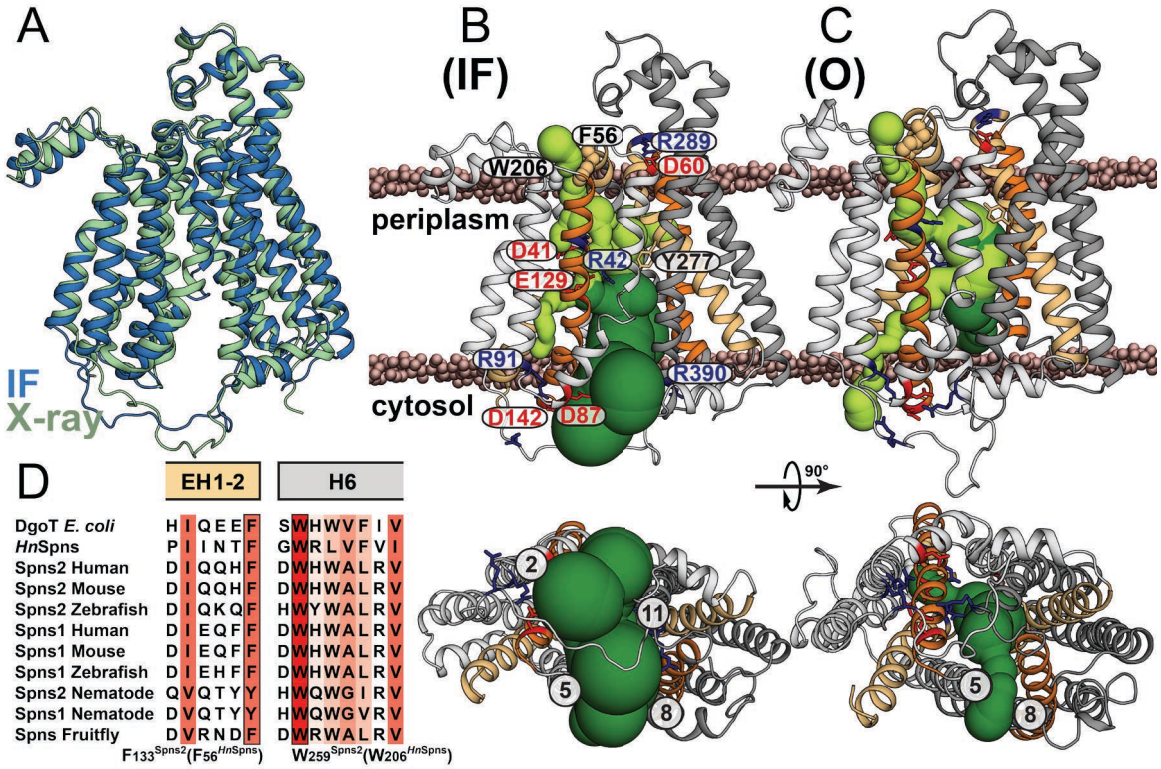

Figure 11. Sampled conformational states of *Hn*Spns reveal a noncanonical ligand-dependent alternating access in the absence of an obvious outward-facing state. (A) The refined X-ray structure of *Hn*Spns in the lipid membrane based on the pH 9 DEER distance populations in nanodiscs (Fig. S14), is IF and comparable to the IF X-ray structure. (B) Calculated tunnels using software MOLEonline within the IF model indicate that the substrate can reach the binding site either from the inner leaflet of the membrane using TMs 2-11 and 5-8 gates or directly from the cytoplasm. Thus, both lipophilic and water-soluble substrates can bind to the transporter. In this conformation, Arg42^{TM1} and Tyr277^{TM7} in the binding site are poised to bind the substrate. (C) Due to the formation of the structural motif A, the intracellular gate between TMs 2 and 11 is closed in the modeled doubly-occluded state based on the pH 4 DEER distances (Fig. S15). However, the gate between TMs 5-8 is not completely occluded and is still accessible from the membrane. The periplasmic salt bridge Asp60^{TM2}-Arg289^{TM7} is also intact in this O state. (D) A putative periplasmic tunnel for proton translocation is predicted on both the refined IF and O models. The top of the tunnel may be constricted by highly conserved residues Trp206^{TM6} and Phe56$^{TM1/EH1-2}$.

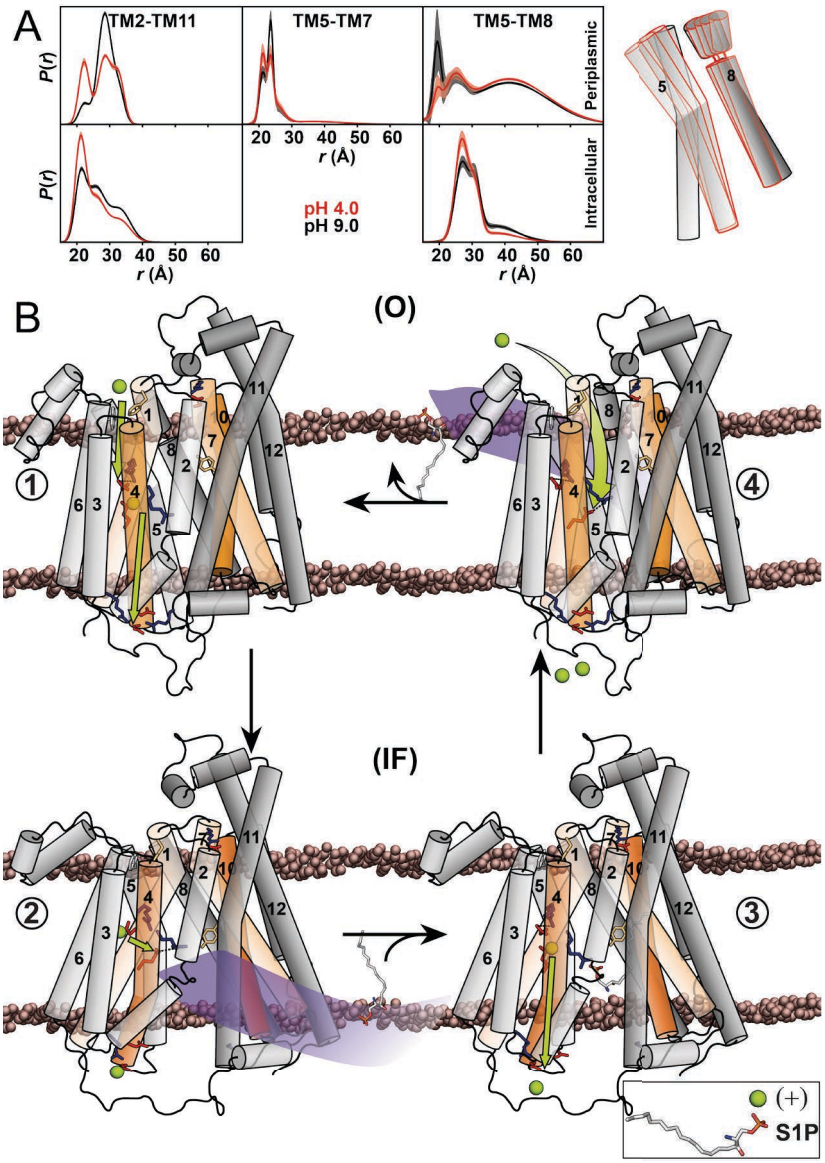

Figure 12. Proposed model of S1P/H$^+$ antiport for *Hn*Spns. (A) Protonation-dependent conformational dynamics are significantly enhanced on the periplasmic side, providing a pathway for ligand exchange. (B) In this model, the stable resting state is IF, whereas the O is of relatively high energy. Side chains of the functionally conserved residues are represented as sticks. Asp41 protonation promotes the Glu129 deprotonation and formation of a charge pair with Arg42 **(1)**. Subsequently, the released proton translocates to the intracellular side, where the acidic residues of the charge-relay network (e.g., Asp142) are protonated, stabilizing the IF conformation, suitable for substrate binding via intracellular side **(2)**. Proton transfer from Asp41 to Glu129 liberates Arg42 to bind substrates like S1P **(3)**. Substrate binding following Glu129 protonation triggers closing of the intracellular side and transition to a periplasmic flexible but closed conformation **(4)**. This enables the substrate release to the periplasmic leaflet, possibly through the putative periplasmic gate between TMs 5-8 and restoration of the Arg42-Glu129 charge pair and Glu129 deprotonation. Glu129 is either re-protonated from the flexible periplasmic side or proton transfer from Glu129 to the intracellular charge-relay network and protonation of Asp41 in step 4 are sufficient to directly reset the transporter to the IF conformation.

Supplementary Information

Protonation-dependent alternating access of a spinster transporter, an emerging family of broad-specificity efflux pumps

Reza Dastvan[1,*], Ali Rasouli[2,§], Sepehr Dehghani-Ghahnaviyeh[2,§], Samantha Gies[1], Emad Tajkhorshid[2,*]

[1] Department of Biochemistry and Molecular Biology, Saint Louis University School of Medicine, St. Louis, MO 63104, USA

[2] Department of Biochemistry and NIH Center for Macromolecular Modeling and Bioinformatics, Beckman Institute for Advanced Science and Technology, University of Illinois at Urbana-Champaign, Urbana, IL 61801, USA

[§] These authors contributed equally to this work.

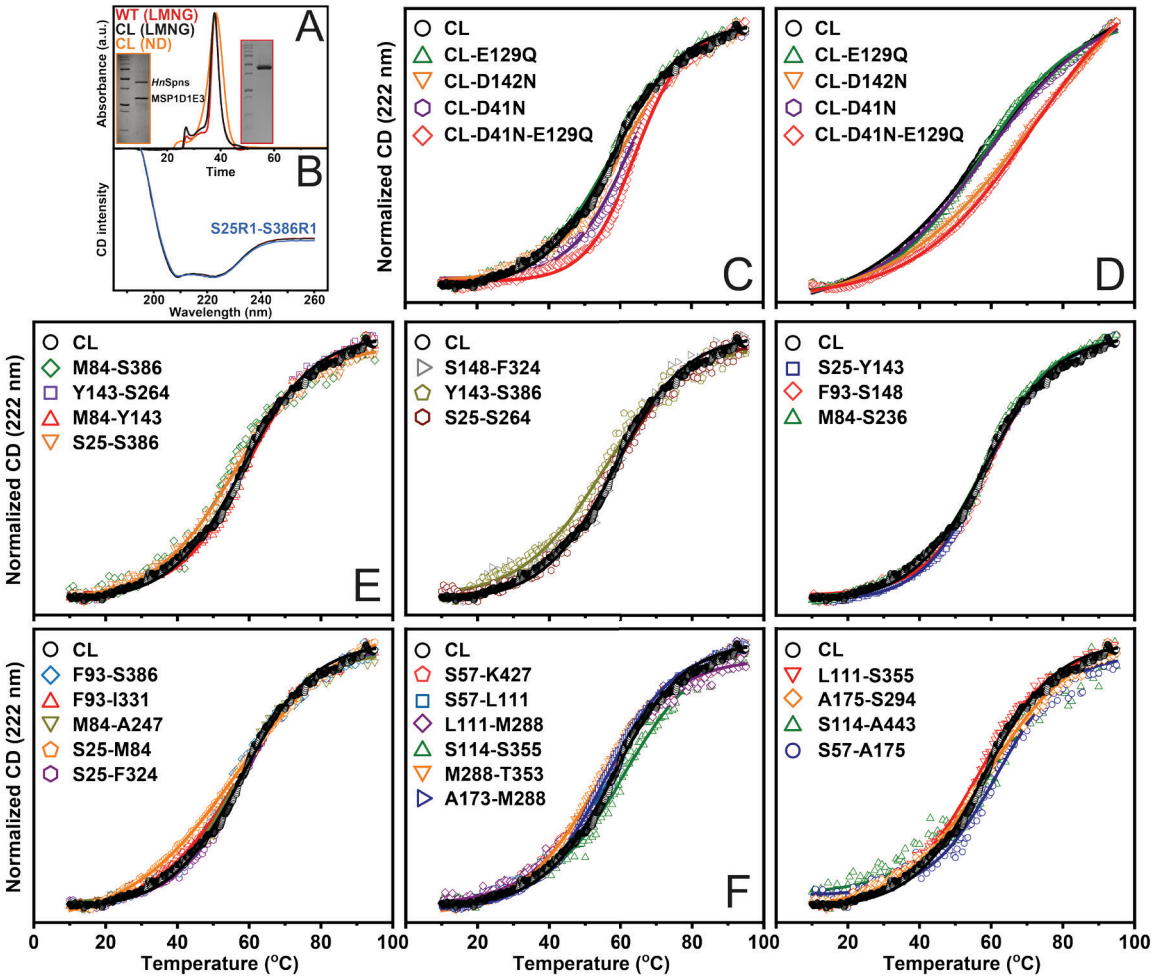

Figure S1. Thermal stability analyses. (A) Size exclusion chromatography profiles of the wildtype (WT) and cysteine-less (CL) *Hn*Spns in LMNG micelles and nanodiscs (ND), and (B) their circular dichroism spectra in micelles along with a spin-labeled DEER mutant. (C) Thermal stability analyses of the protonation mimetic mutants in LMNG micelles and (D) lipid nanodiscs, compared to the CL protein. (E) Thermal stability analyses of the spin-labeled DEER mutants on the intracellular and (F) extracellular side in LMNG micelles compared to CL protein.

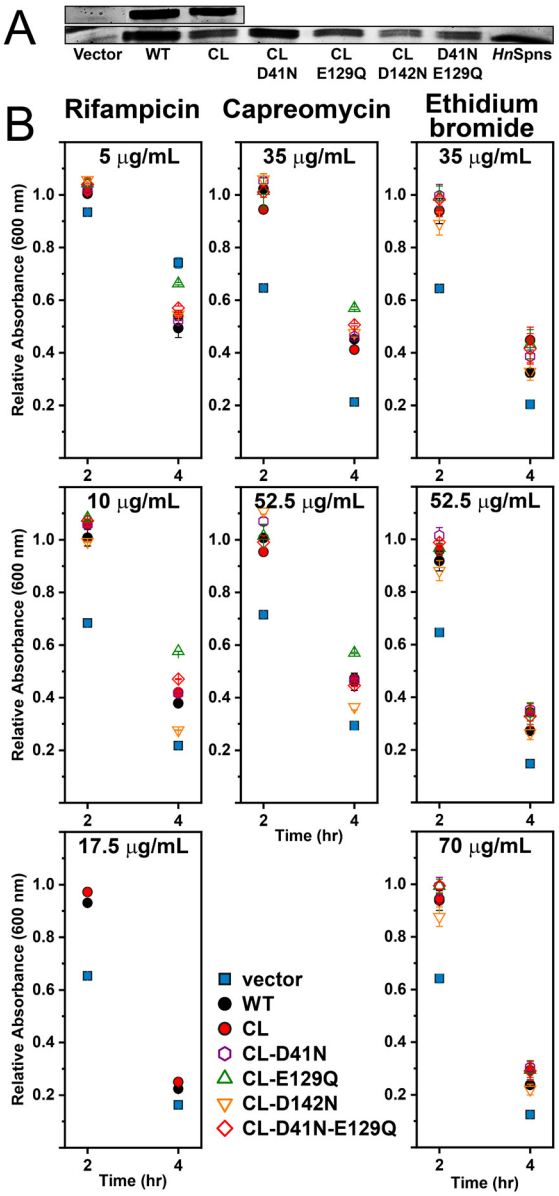

Figure S2. Cell growth-based drug resistance assays. (A) The relative expression of WT, CL, and the protonation mimetic mutants of *Hn*Spns in the cell growth assays was visualized by SDS-PAGE and staining with InVision His tag stain, confirming similar levels of expression for each construct. Purified *Hn*Spns used as a standard is shown for comparison. (B) Cell growth for the WT and its variants relative to the vector at 37°C, in the presence of different concentrations of rifampicin, capreomycin and ethidium bromide. Each data point was performed in triplicate, and the experiments were repeated. Absorbances at 600 nm in the presence of drugs were divided by the 0 μg/ml drug well. The standard deviation is shown for each data point.

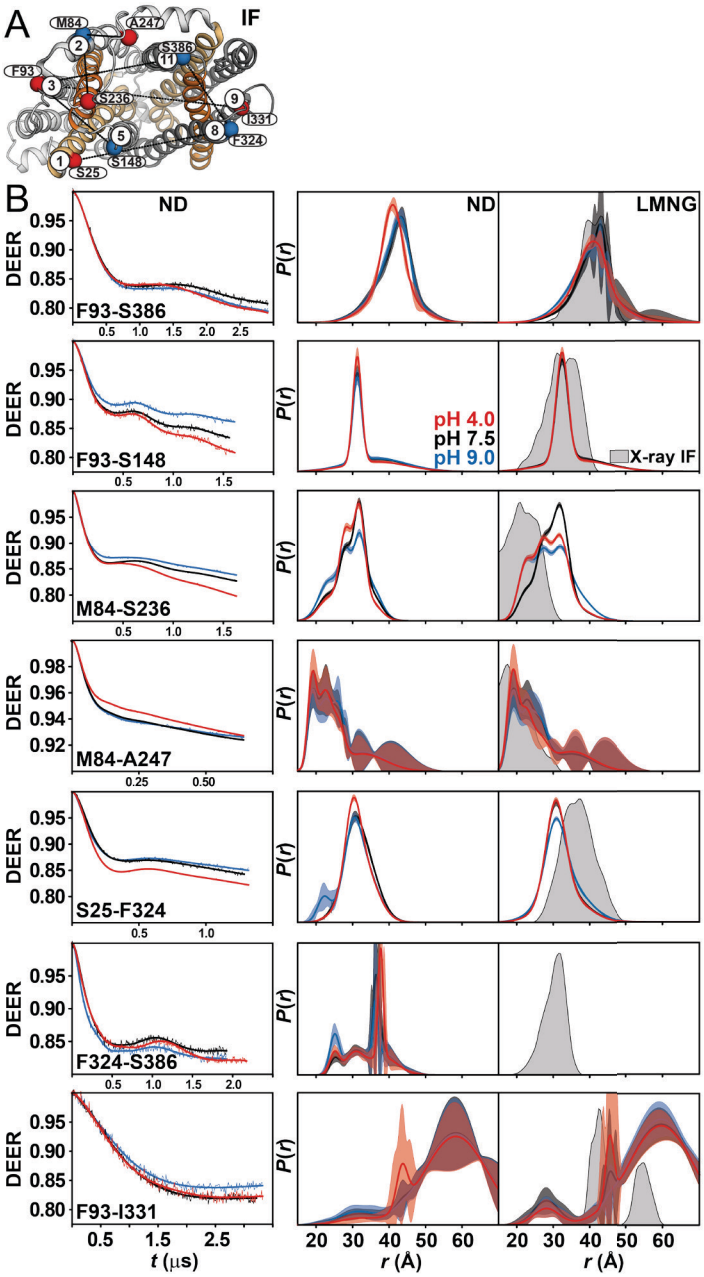

Figure S3. DEER distance measurements on the intracellular side. (A) Spin label pairs are depicted on the intracellular side of the IF crystal structure. (B) Raw DEER decays and fits (left) are presented for the experimentally determined distributions *P*(*r*) in lipid nanodiscs (middle), compared to distance distributions in LMNG micelles (right), with predicted distributions derived from the IF crystal structure (shaded gray).

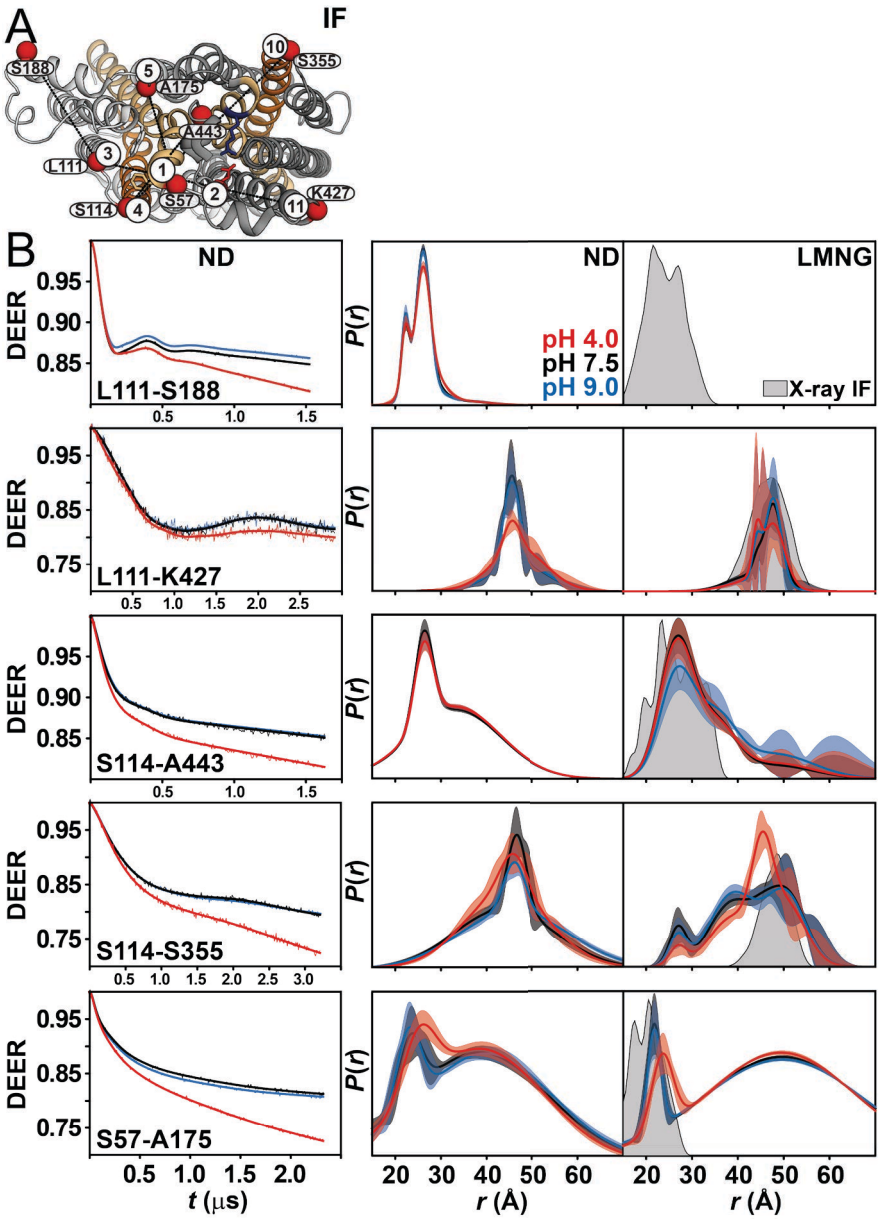

Figure S4. DEER distance measurements on the periplasmic side. (A) Spin label pairs are depicted on the periplasmic side of the IF crystal structure. (B) Raw DEER decays and fits (left) are presented for the experimentally determined distributions *P*(*r*) in lipid nanodiscs (middle), compared to distance distributions in LMNG micelles (right), with predicted distributions derived from the IF crystal structure (shaded gray).

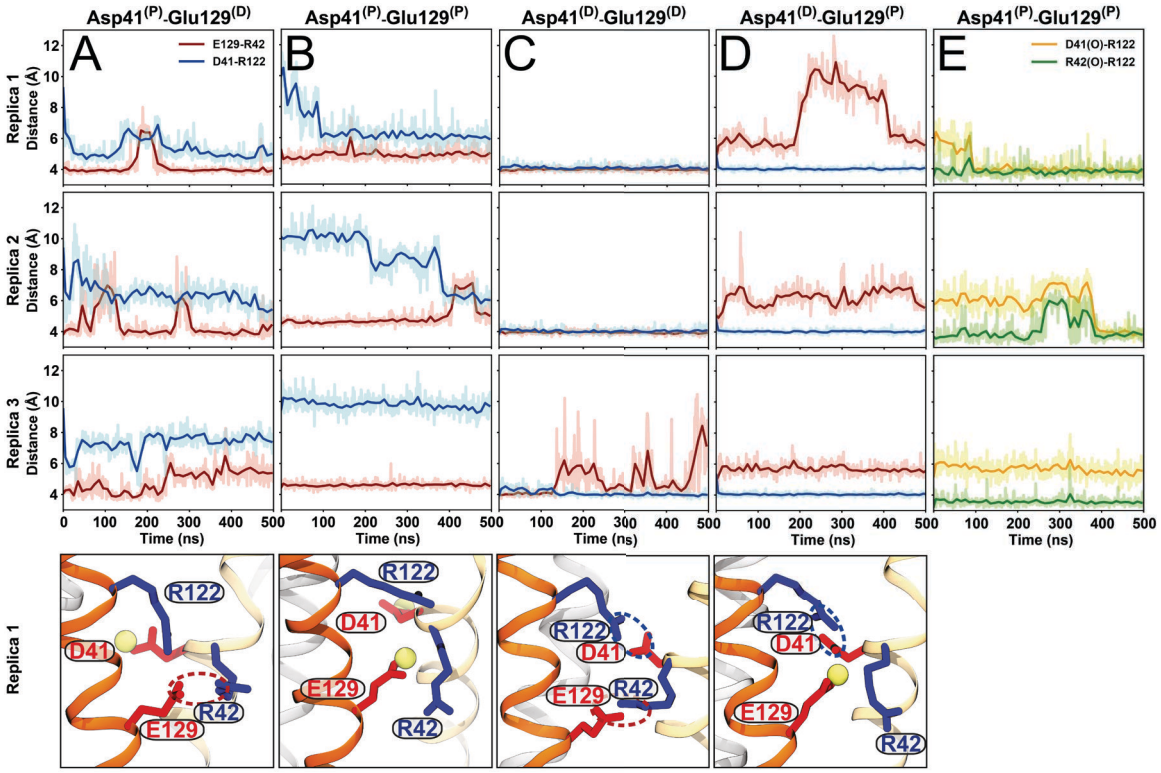

Figure S5. Molecular dynamics simulations of the *Hn*Spns IF structure in lipid membranes with different permutations of protonation states of Asp41 and Glu129 (four different systems A-D in three independent copies) and their interactions with two nearby basic residues. (E) Double protonation of these acidic residues stabilizes a distinct conformation in which the side chain of Arg122 continuously and transiently interacts with the backbone oxygen of Arg42 and Asp41, respectively. Molecular snapshots are captured from the last frame of each trajectory of the first replica. Acidic and basic residues are shown in red and blue, respectively, and the proton is represented with a yellow sphere.

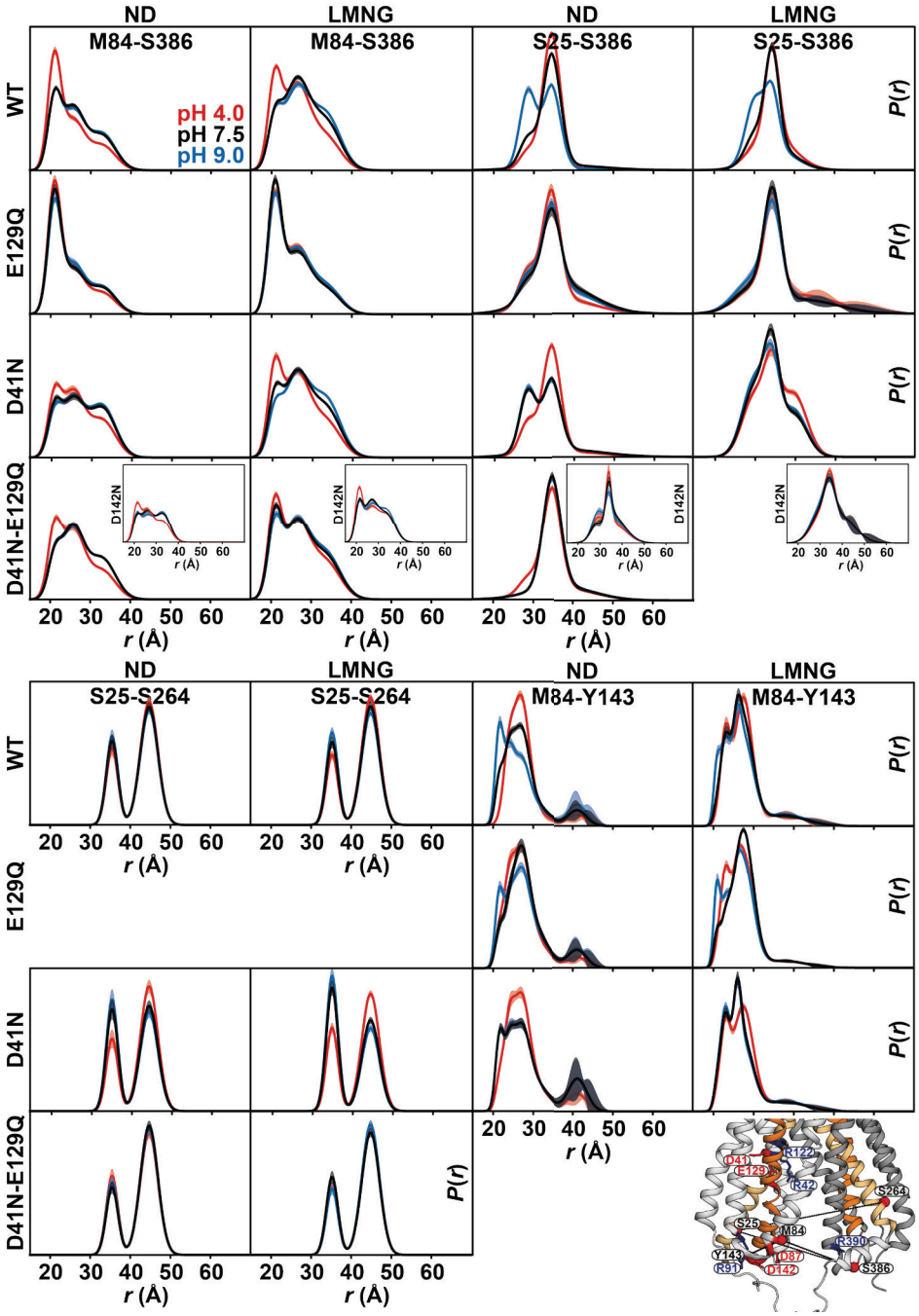

Figure S6. Effect of protonation-mimetic mutation of acidic residues on conformational states in equilibrium on the intracellular side in lipid nanodiscs and detergent micelles. The single (E129Q, D41N, D142N) or double (D41N/E129Q) mutations were combined with the double-cysteine mutations. DEER experiments in the presence of these mutations support the results of the MD simulations and reveal that Asp41 protonation has the opposite effect from that of Glu129 on the conformational changes on the intracellular side.

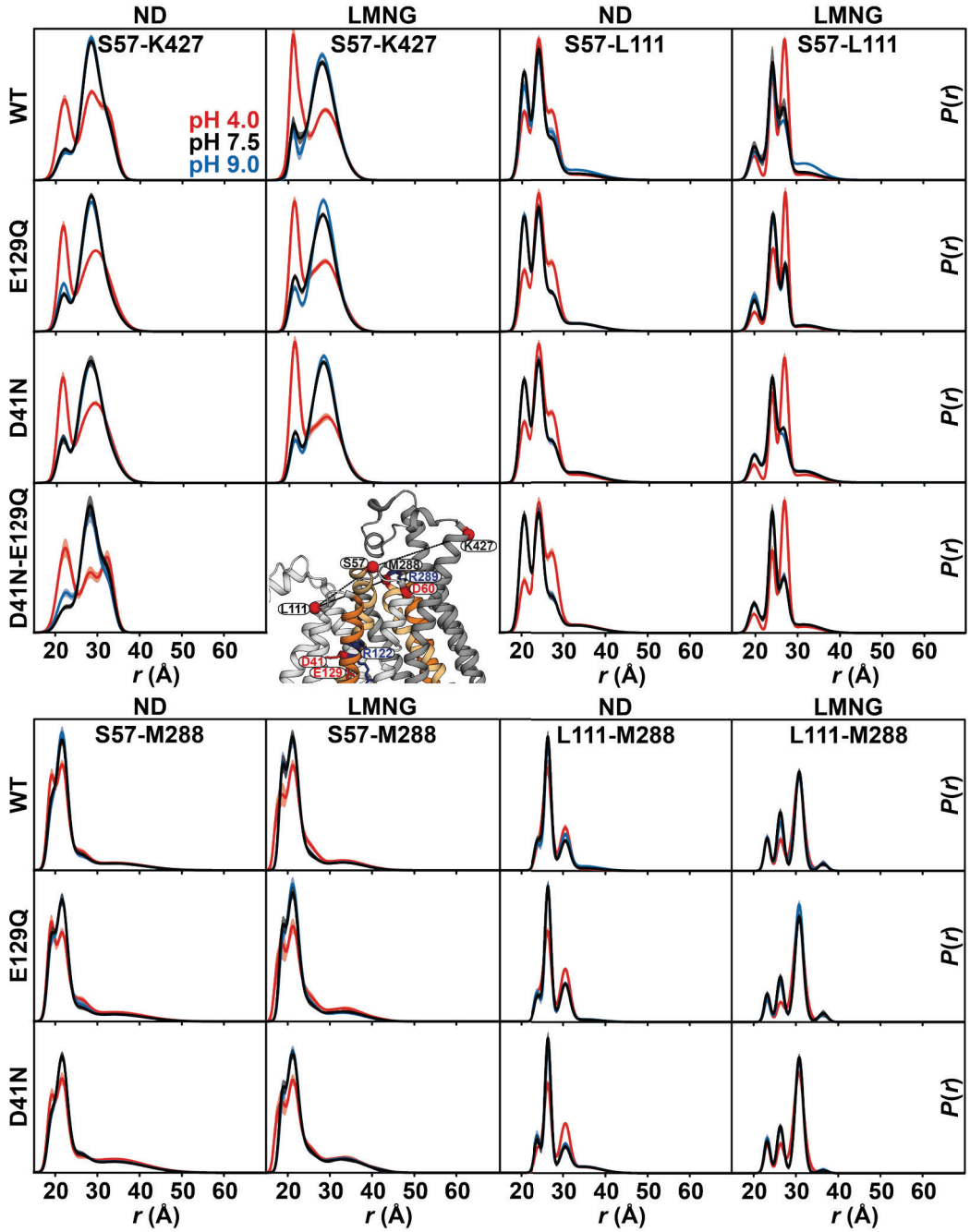

Figure S7. Effect of protonation-mimetic mutation of acidic residues on conformational states in equilibrium on the periplasmic side in lipid nanodiscs and detergent micelles. The single (E129Q, D41N, D142N) or double (D41N/E129Q) mutations were combined with the double-cysteine mutations. DEER experiments in the presence of these mutations reveal that the periplasmic side remains mostly invariant in response to these mutations.

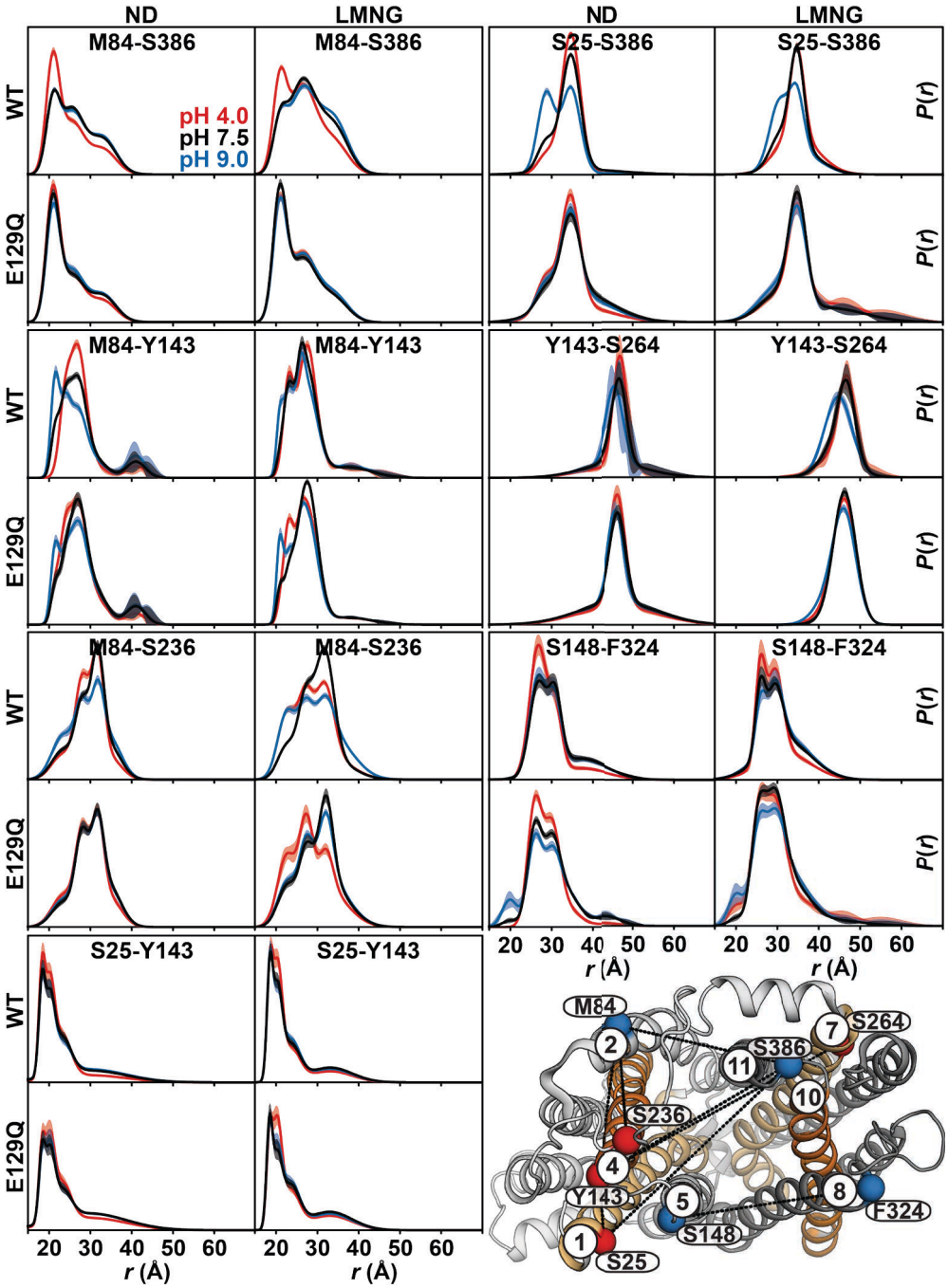

Figure S8. Effect of protonation-mimetic mutation of the intracellular protonation master switch glutamate 129 (E129Q) on conformational states in equilibrium on the intracellular side in lipid nanodiscs and detergent micelles. The E129Q mutation was combined with the double-cysteine mutations. The E129Q mutation captures the transporter in the pH 4 population state, i.e., the inward-closed conformation. Thus, our data suggest that E129 is the intracellular protonation master switch regulating the conformational transition between IF and inward-closed states.

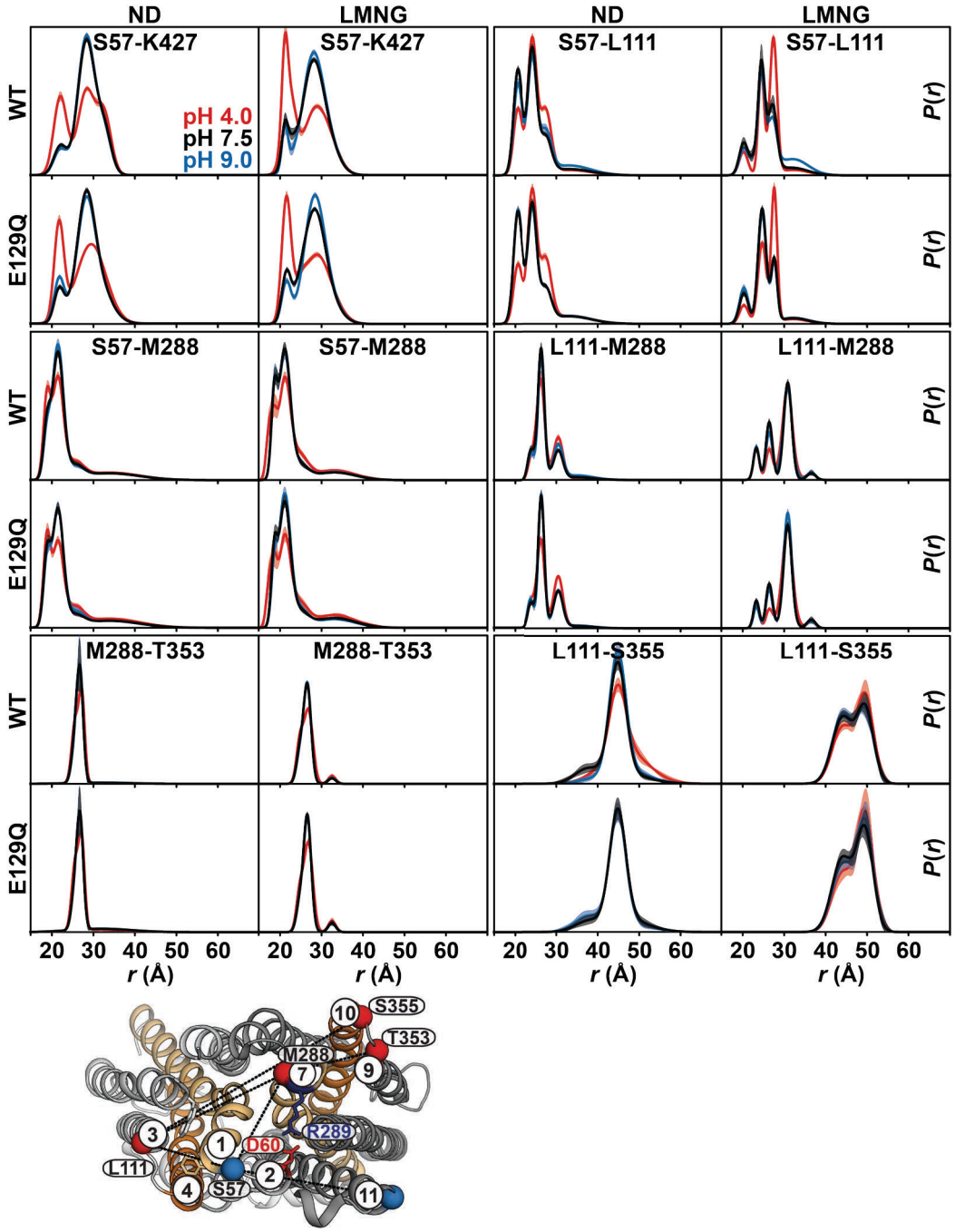

Figure S9. Effect of protonation-mimetic mutation of the intracellular protonation master switch glutamate 129 (E129Q) on conformational states in equilibrium on the periplasmic side in lipid nanodiscs and detergent micelles. The E129Q mutation was combined with the double-cysteine mutations. DEER experiments reveal that the periplasmic side remains mostly invariant in response to this mutation.

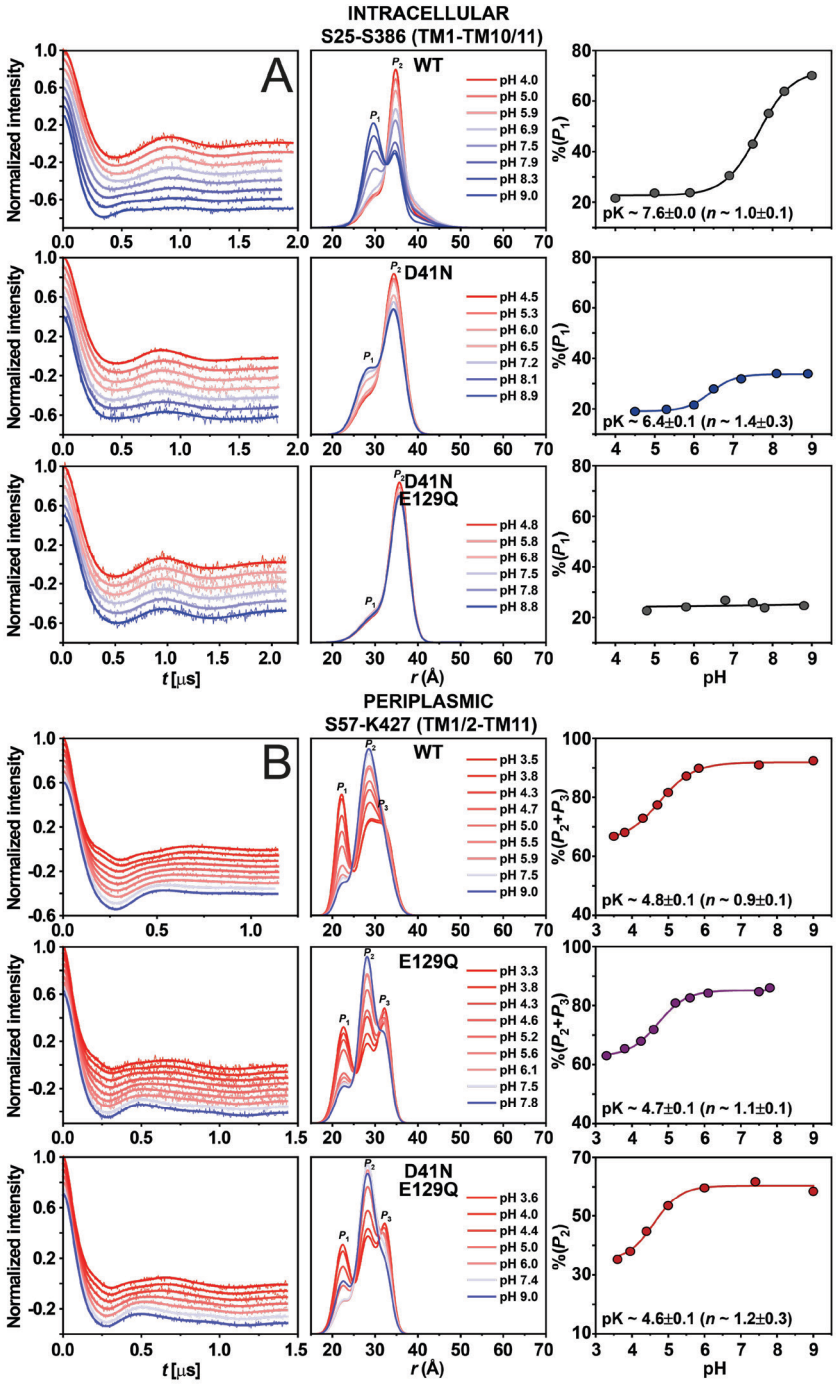

Figure S10. Intracellular and periplasmic sides of *Hn*Spns sense differently its protonation state. (A) Distance distributions of intracellular (S25-S386) and periplasmic (S57-K427) pairs were obtained at different pH values in lipid nanodiscs with and without protonation-mimetic mutations of acidic residues. The variation in population of rising or decreasing distance peaks as a function of pH was used to estimate the pK value for conformational changes in *Hn*Spns. The D41N-E129Q double mutation abrogates conformational changes on the intracellular side with periplasmic side mainly unaffected, demonstrating the decoupling of transmembrane protonation-dependent conformational changes.

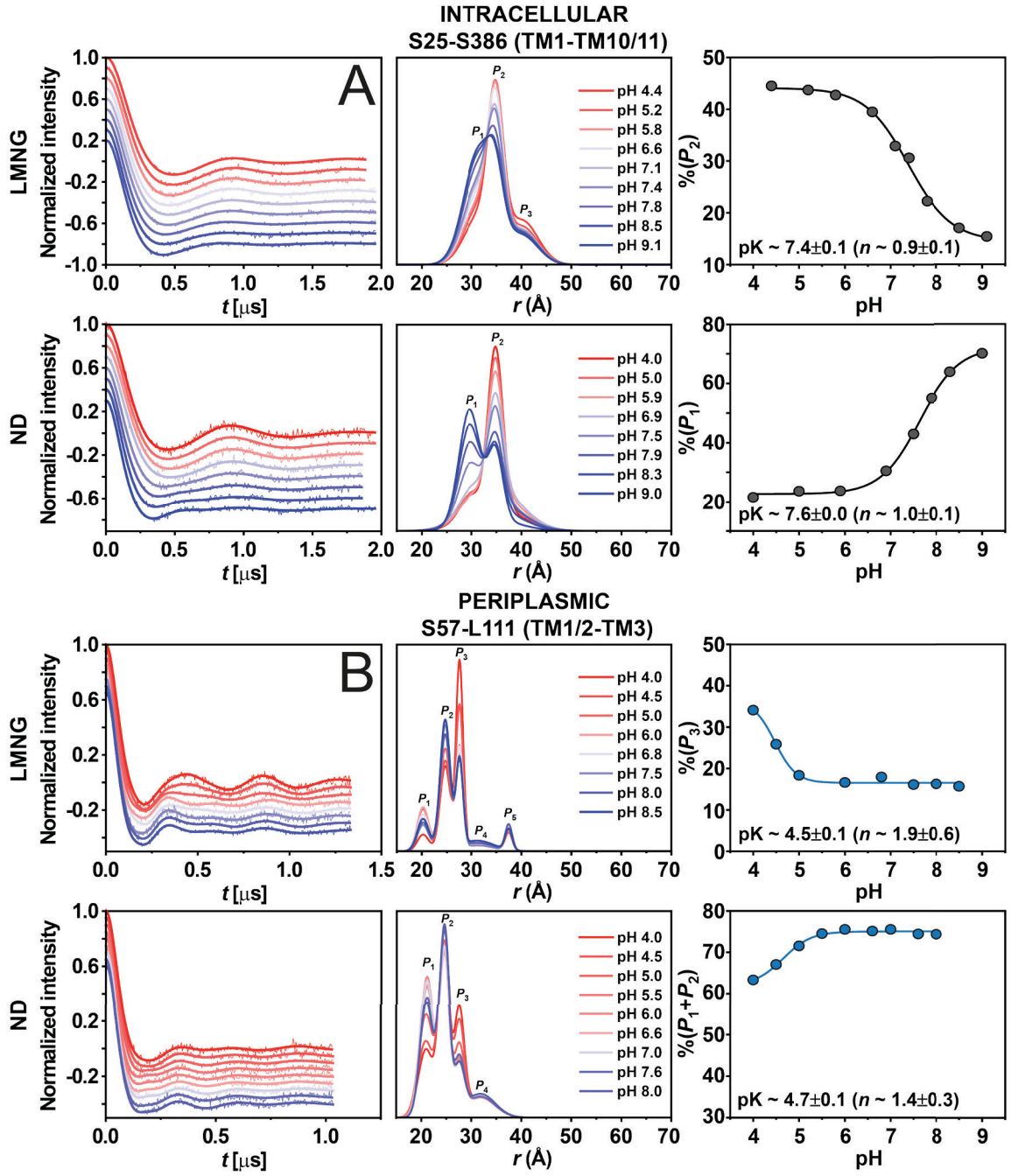

Figure S11. Effect of environment (lipid nanodiscs vs. micelles) on sensing the protonation state of *Hn*Spns. (A) Distance distributions of intracellular (S25-S386) and (B) periplasmic (S57-L111) pairs were obtained at different pH values in lipid nanodiscs and LMNG micelles. Similar pK values were obtained in LMNG micelles and lipid nanodiscs.

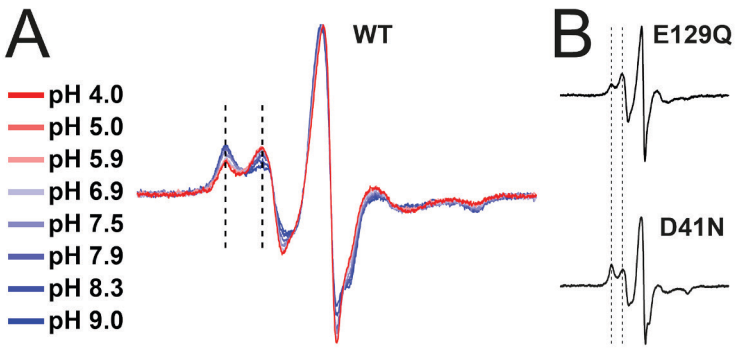

Figure S12. (A) The pH-dependence of the CW EPR spectra of the S25-S386 (TM1-TM10/11) intracellular pair. (B) The D41N and E129Q mutations on the same cysteine pair shift the equilibrium in opposite directions towards basic and acidic pH states, respectively.

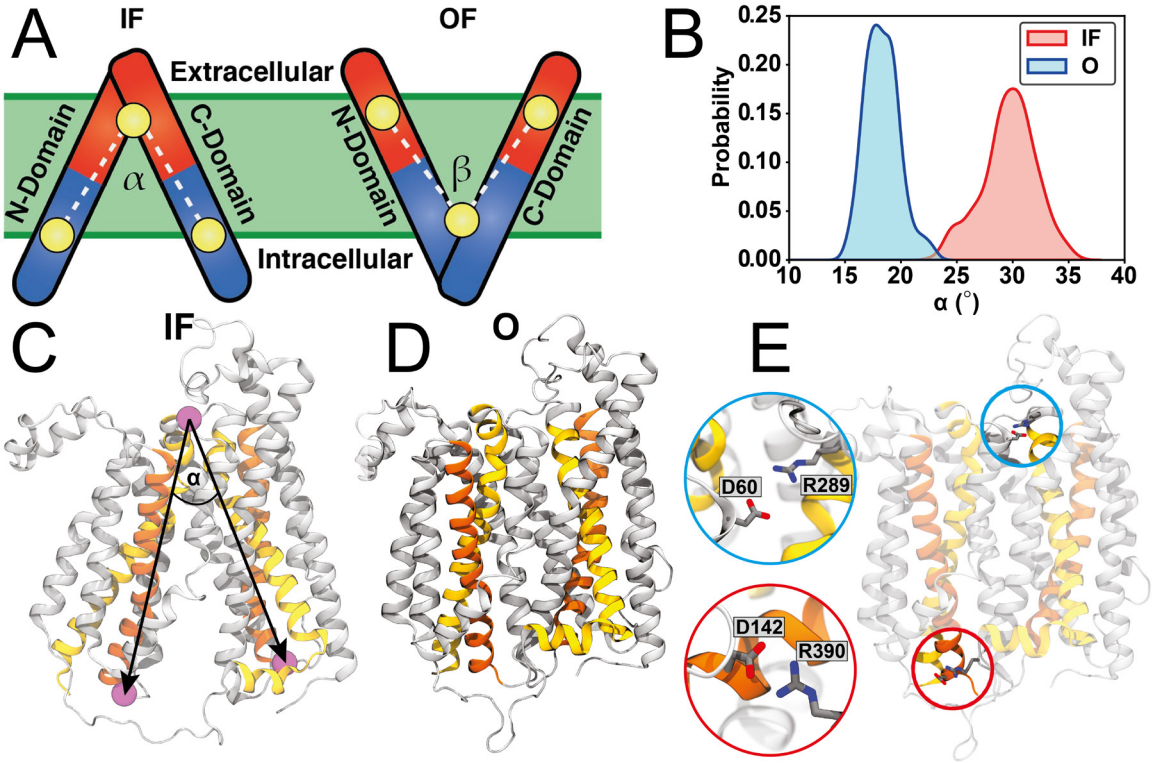

Figure S13. Capturing a stable O conformation of *Hn*Spns. (A) Two orientation-based collective variables, α and β, representing the intracellular and extracellular opening/closing of the transporter, respectively, used to control the conformation of the transporter. N- and C-domain are split into two equal segments shown in red and blue, representing the extracellular and intracellular halves, respectively. α is defined as the angle between the center of mass of three parts: (1) the intracellular half of N-domain, (2) the extracellular half of the protein (including both the N- and C-domains), and (3) the intracellular half of C-domain. β is the angle between (1) the extracellular half of N-domain, (2) the intracellular half of the protein (including both the N- and C-domains), and (3) the extracellular half of C-domain. (B) Probability distribution of the intracellular opening of the transporter for the IF and stabilized O conformations through 500 ns of equilibrium simulations. (C) The IF conformation and definition of the intracellular opening angle. (D) The stable O conformation. (E) Periplasmic (Arg289^{TM7}-Asp60^{TM2}) and intracellular (Arg390^{TM11}-Asp142^{TM4}) salt-bridges are formed, stabilizing the O conformation.

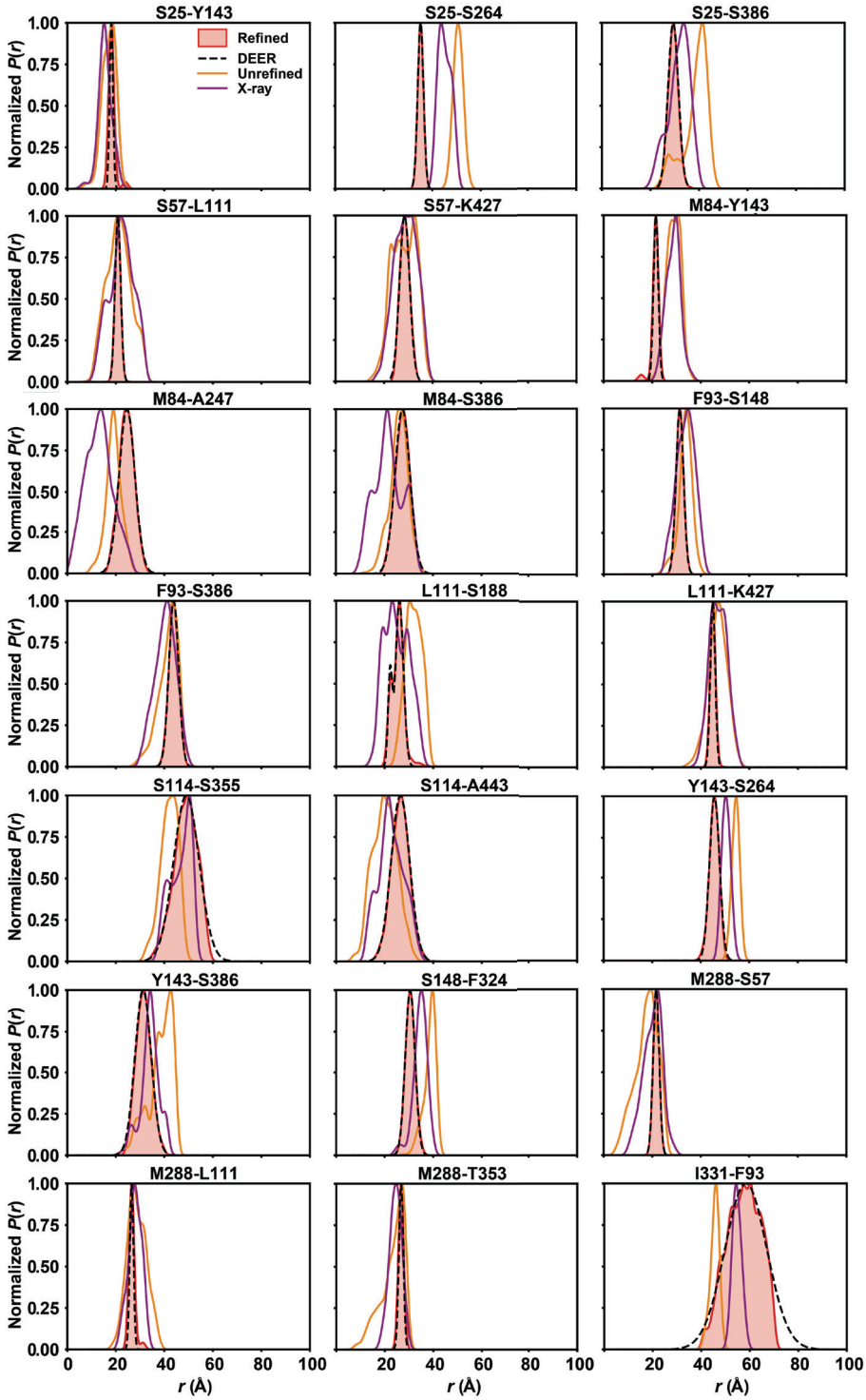

Figure S14. DEER restraint-assisted refinement of IF *Hn*Spns structure in lipid membranes. Comparison of the distance distributions from the refined structure (shaded red) to the experimental pH 9 DEER distance populations in nanodiscs (dashed black lines), the relaxed unrefined template (orange lines), and the predicted distributions on the crystal structure (purple lines). The refined model completely matches the experimental distance populations.

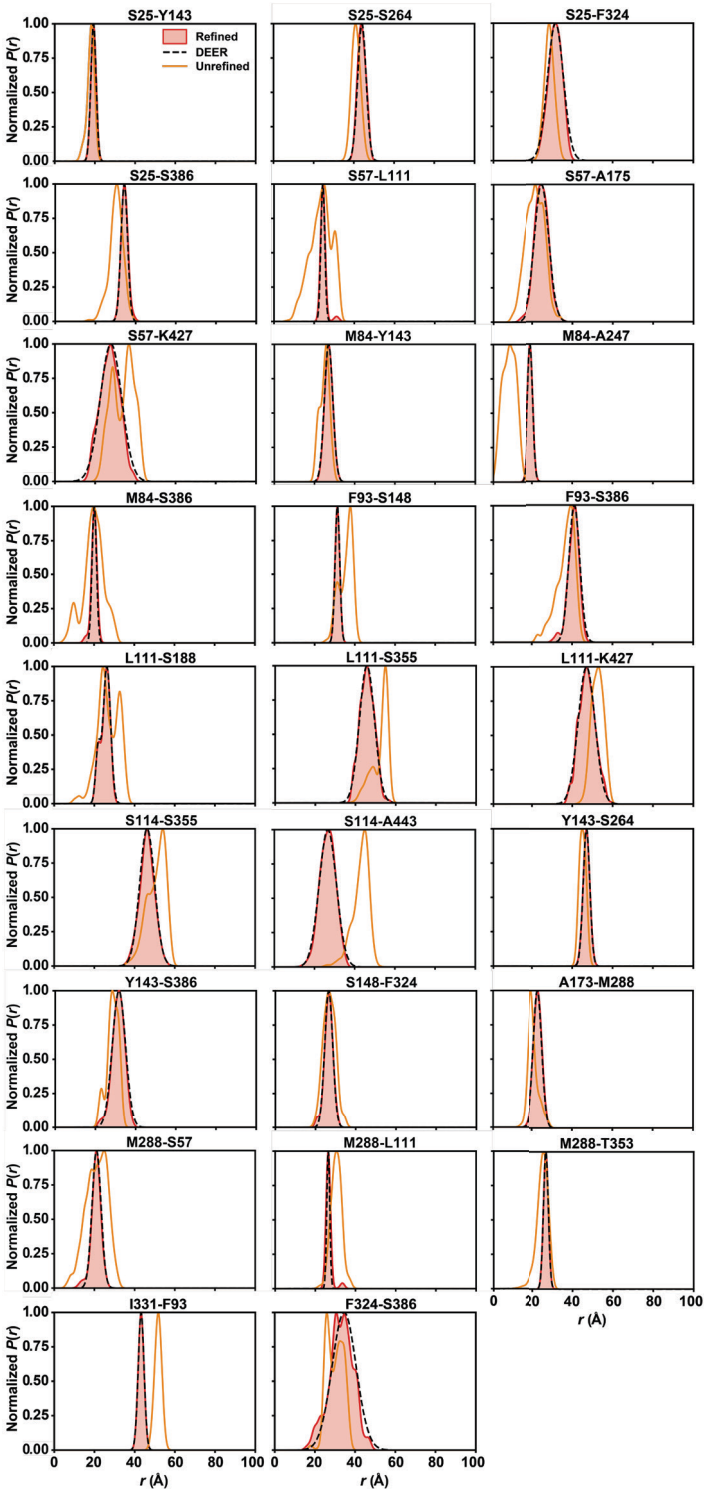

Figure S15. Refinement of the O state of *Hn*Spns in lipid membrane. Comparison of the distance distributions from the refined model (shaded red) to the experimental pH 4 DEER distance populations in nanodiscs (dashed black lines), and the unrefined template, without imposing the harmonic restraints on the probes (orange lines). The refined model matches the experimental distance populations.

Table S1. Thermal stability melting temperatures (T_m) of spin-labeled DEER and protonation mimetic mutants in LMNG micelles and lipid nanodiscs.

	T_m (°C) ± Fitting Error	
Mutant	**LMNG**	**ND**
CL	58.1±0.1	58.3±0.1
CL-E129Q	57.7±0.1	57.3±0.1
CL-D142N	60.0±0.2	72.8±0.4
CL-D41N	62.2±0.2	58.8±0.2
CL-D41N-E129Q	64.2±0.1	71.3±0.2
M84C-S386C	54.8±0.4	56.6±0.5
M84C-Y143C	58.8±0.1	57.5±0.2
S25C-S386C	55.6±0.1	54.3±0.1
S25C-S264C	58.0±0.2	64.1±0.9
S148C-F324C	58.4±0.3	58.7±0.5
Y143C-S264C	58.4±0.1	71.3±0.3
Y143C-S386C	54.7±0.3	61.8±0.2
S57C-K427C	55.7±0.1	54.8±0.2
S57C-L111C	58.0±0.2	58.1±0.1
L111C-M288C	54.7±0.2	56.1±0.1
S114C-S355C	61.2±0.3	54.9±0.1
F93C-S148C	59.2±0.1	72.1±0.5
S25C-Y143C	58.4±0.1	58.6±0.2
M84C-S236C	58.0±0.1	61.8±0.2
S25C-F324C	58.5±0.1	
M84C-A247C	57.1±0.1	59.8±0.2
F93C-I331C	57.5±0.1	67.7±0.3
F93C-S386C	56.3±0.1	77.3±0.7
S25C-M84C	56.5±0.1	
F324C-S386C		63.8±0.1
S57C-A175C	61.5±0.3	59.9±0.2
S114C-A443C	60.7±0.5	70.6±0.7
L111C-S355C	56.2±0.1	64.6±0.2
A175C-S294C	58.9±0.1	58.8±0.7
M288C-T353C	53.9±0.3	62.9±0.3
A173C-M288C	55.5±0.1	
L111C-K427C		79.0±1.0
L111C-S188C		60.2±0.2

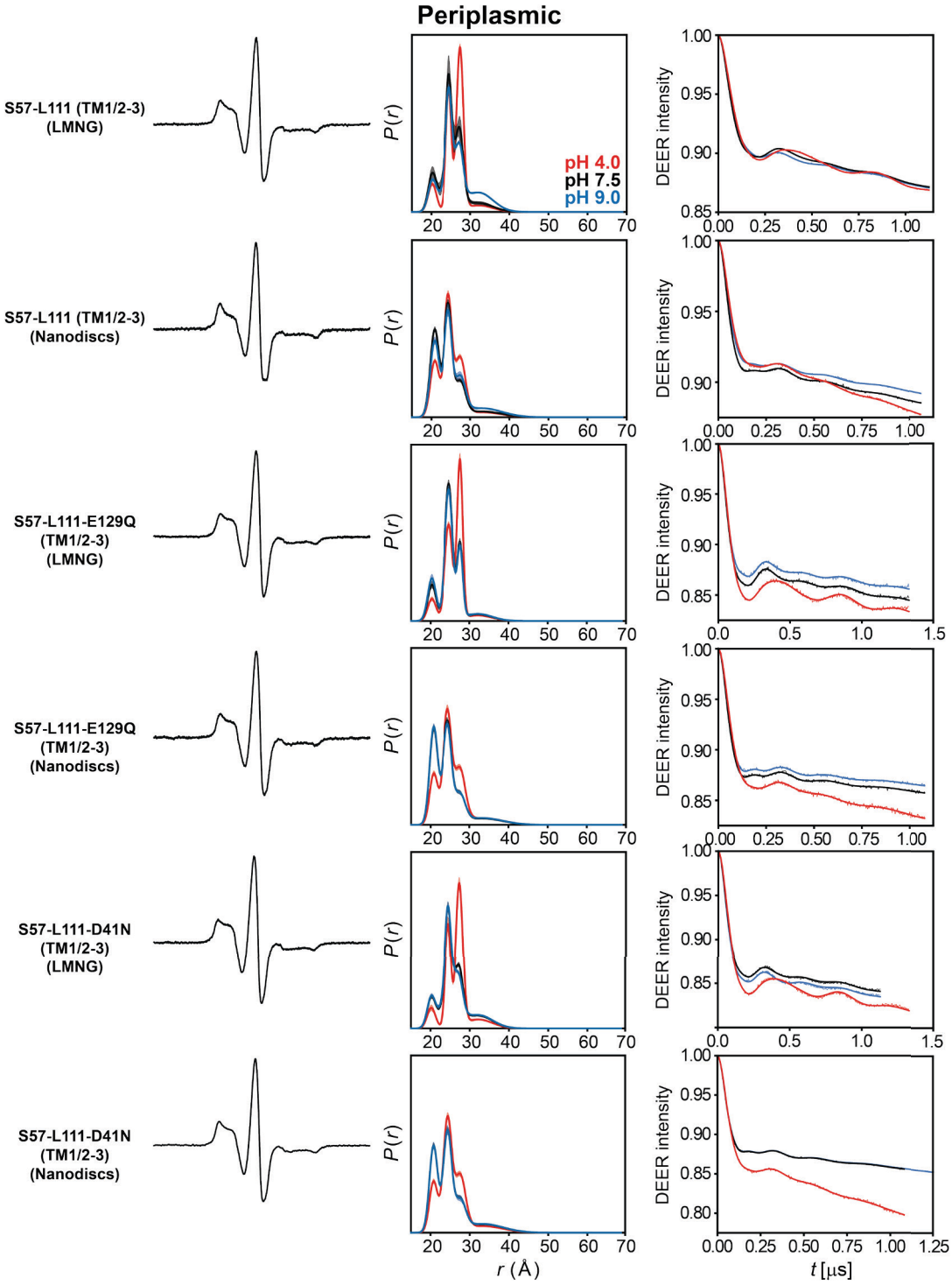

Data Appendix 1. DEER data analysis for the periplasmic side. For each mutant, from left to right, CW EPR, distance distributions, and the primary DEER traces along with the fits are shown.

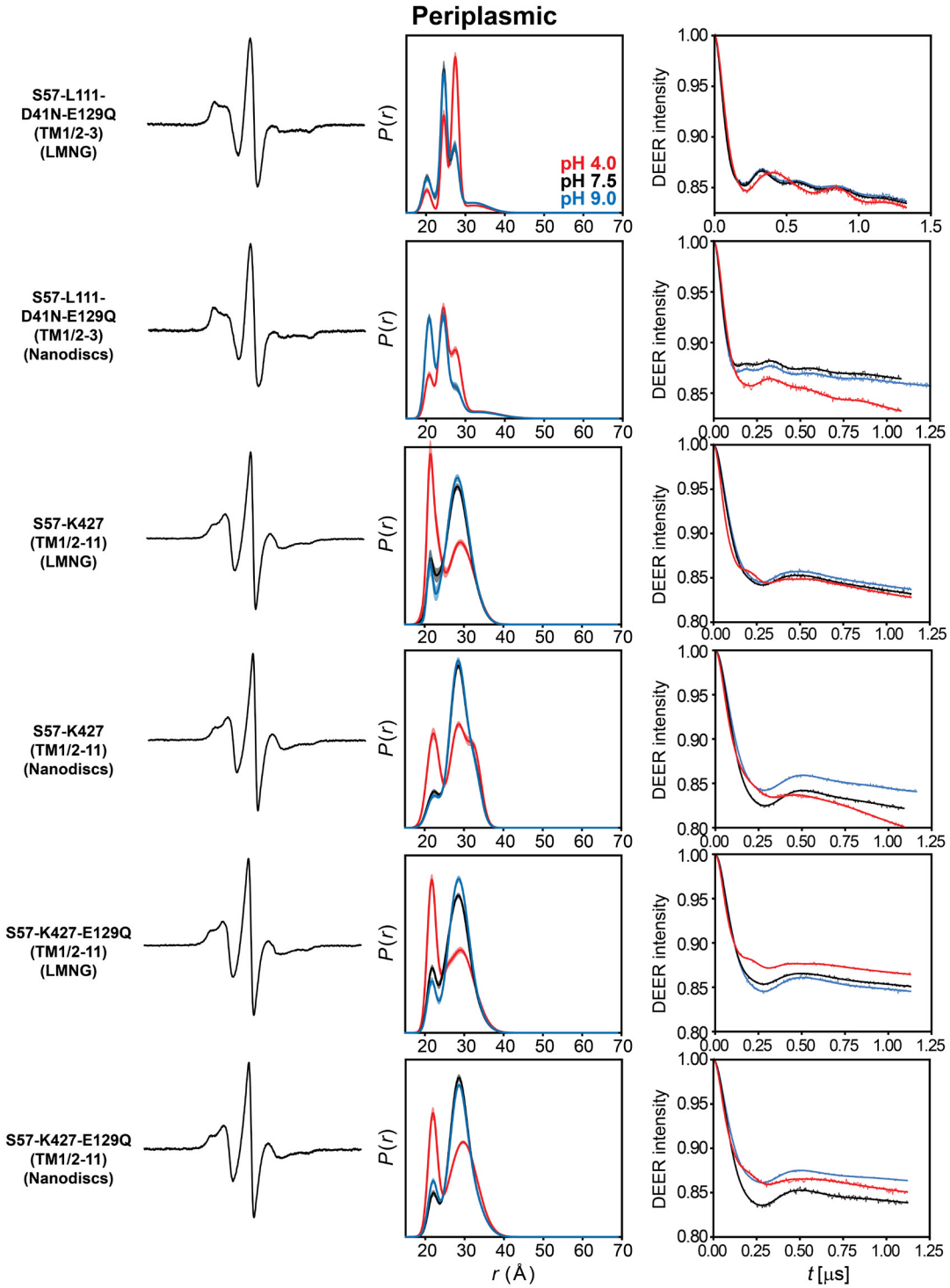

Data Appendix 2. DEER data analysis for the periplasmic side. For each mutant, from left to right, CW EPR, distance distributions, and the primary DEER traces along with the fits are shown.

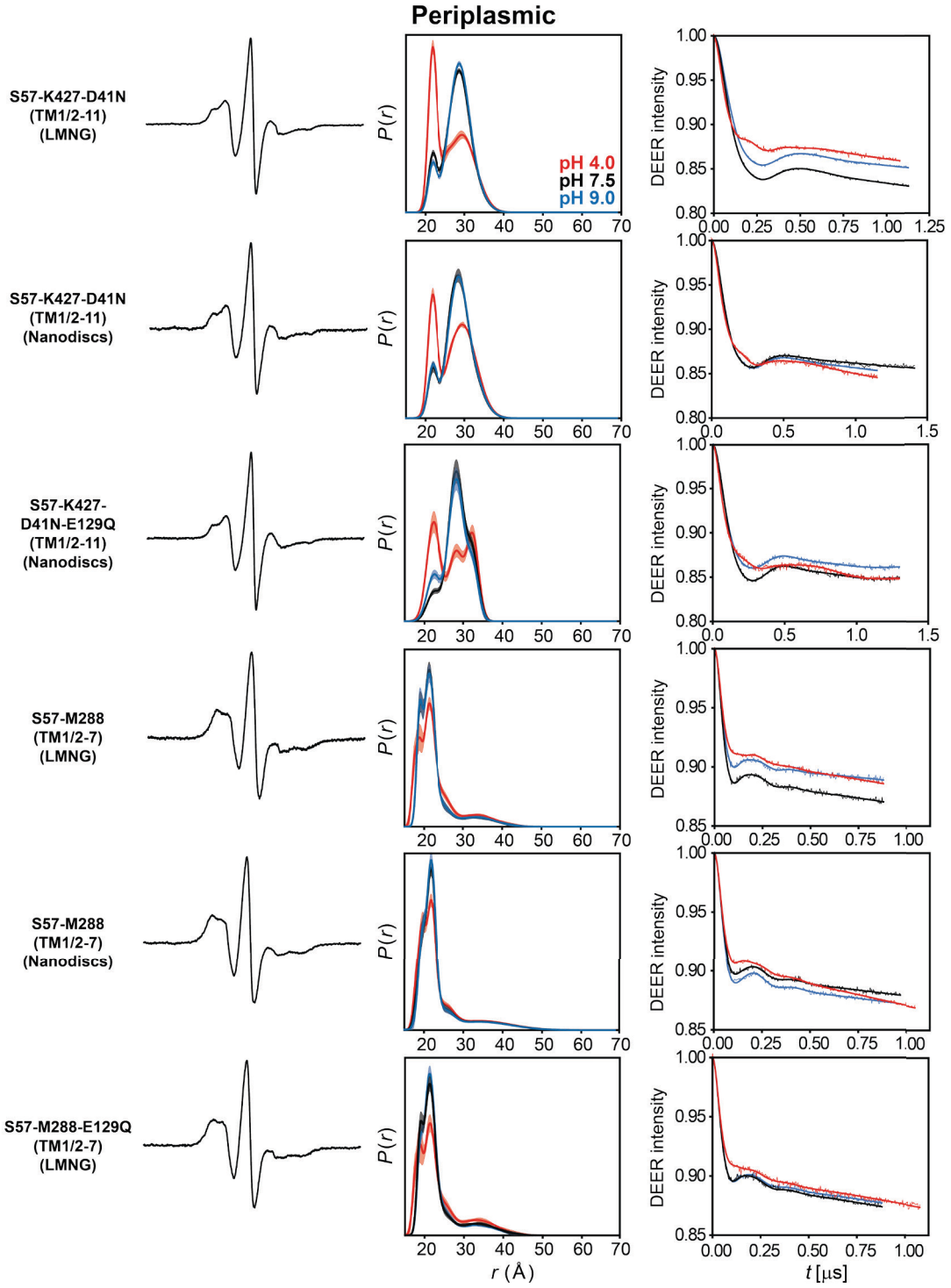

Data Appendix 3. DEER data analysis for the periplasmic side. For each mutant, from left to right, CW EPR, distance distributions, and the primary DEER traces along with the fits are shown.

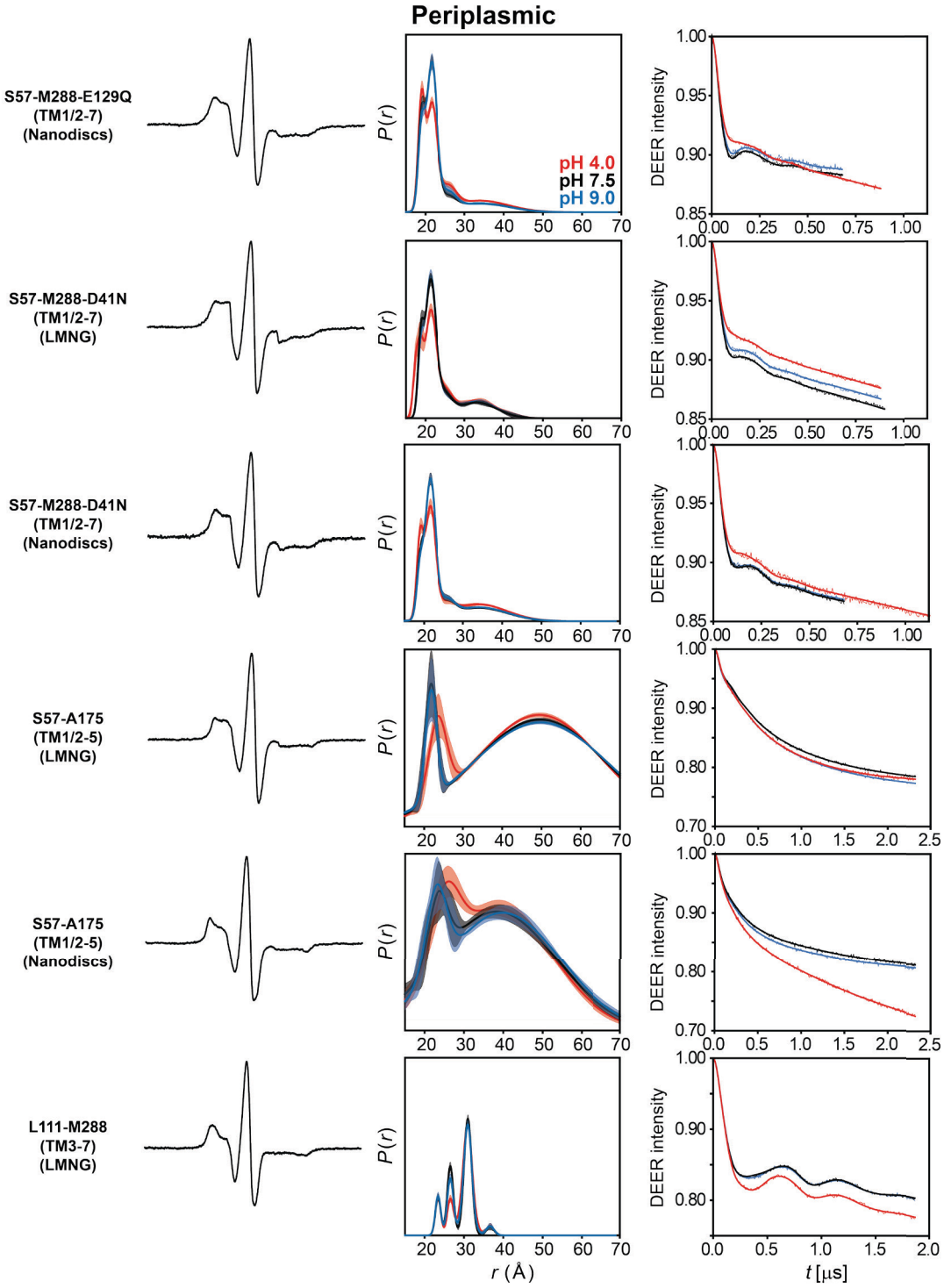

Data Appendix 4. DEER data analysis for the periplasmic side. For each mutant, from left to right, CW EPR, distance distributions, and the primary DEER traces along with the fits are shown.

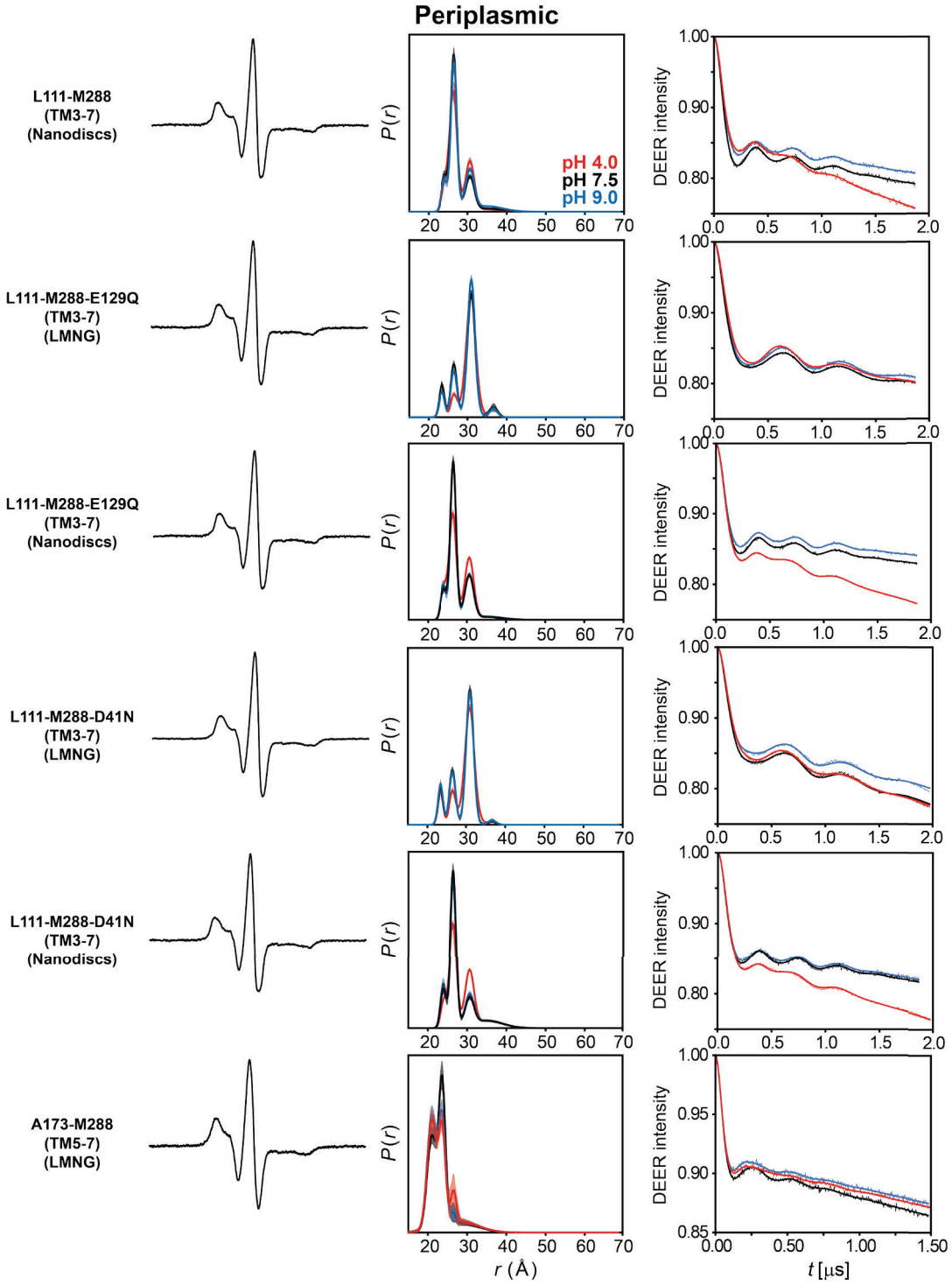

Data Appendix 5. DEER data analysis for the periplasmic side. For each mutant, from left to right, CW EPR, distance distributions, and the primary DEER traces along with the fits are shown.

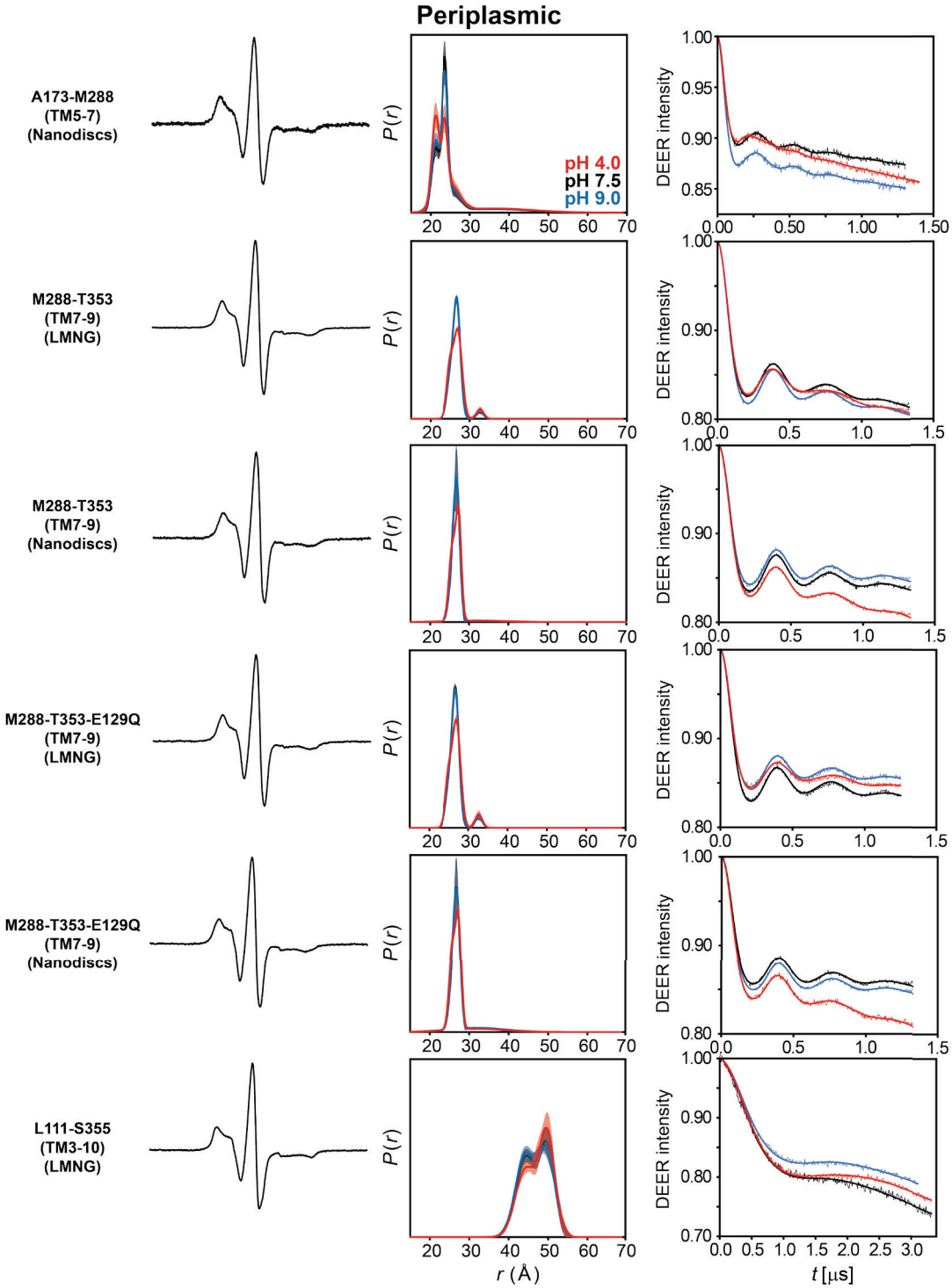

Data Appendix 6. DEER data analysis for the periplasmic side. For each mutant, from left to right, CW EPR, distance distributions, and the primary DEER traces along with the fits are shown.

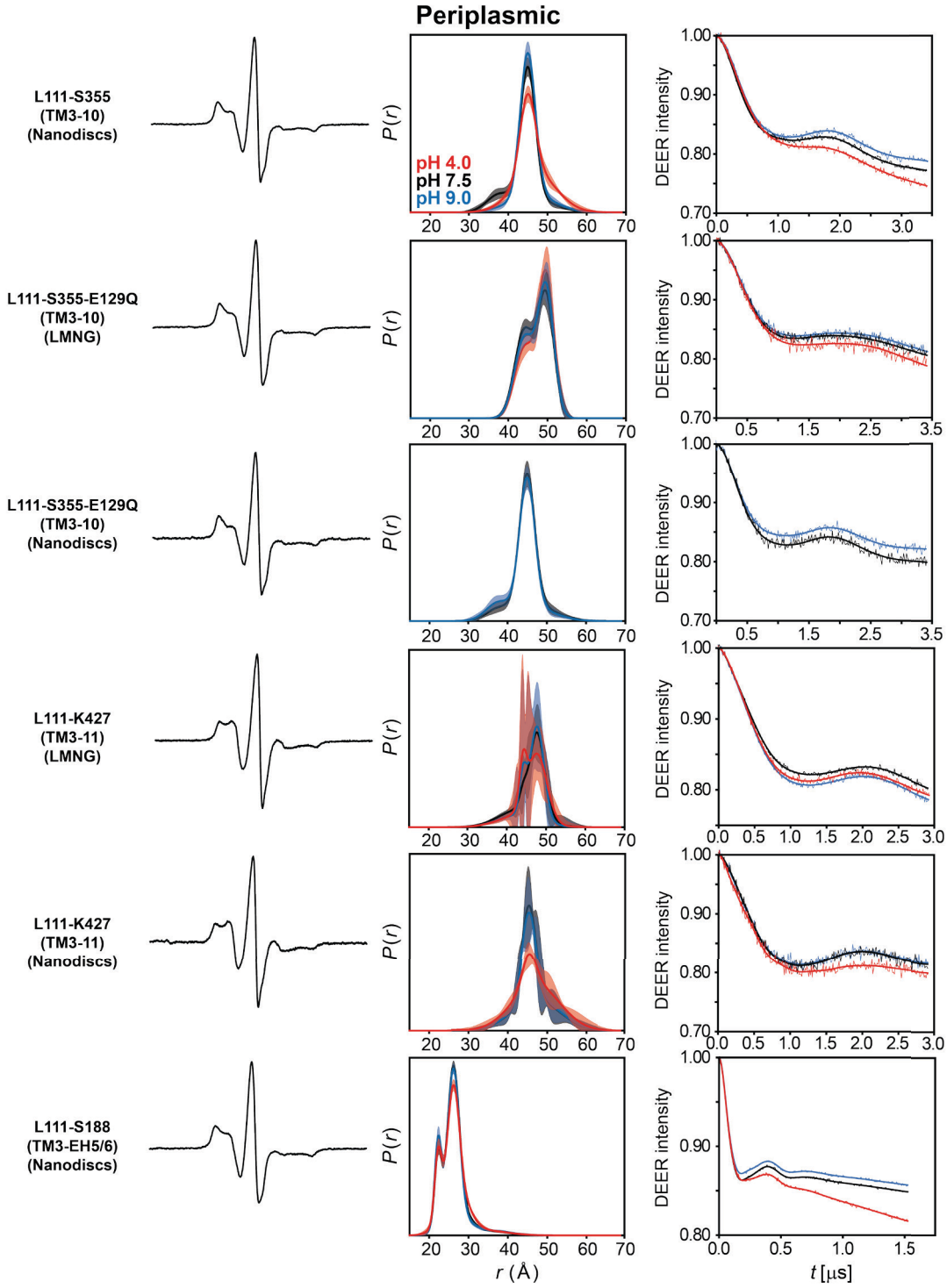

Data Appendix 7. DEER data analysis for the periplasmic side. For each mutant, from left to right, CW EPR, distance distributions, and the primary DEER traces along with the fits are shown.

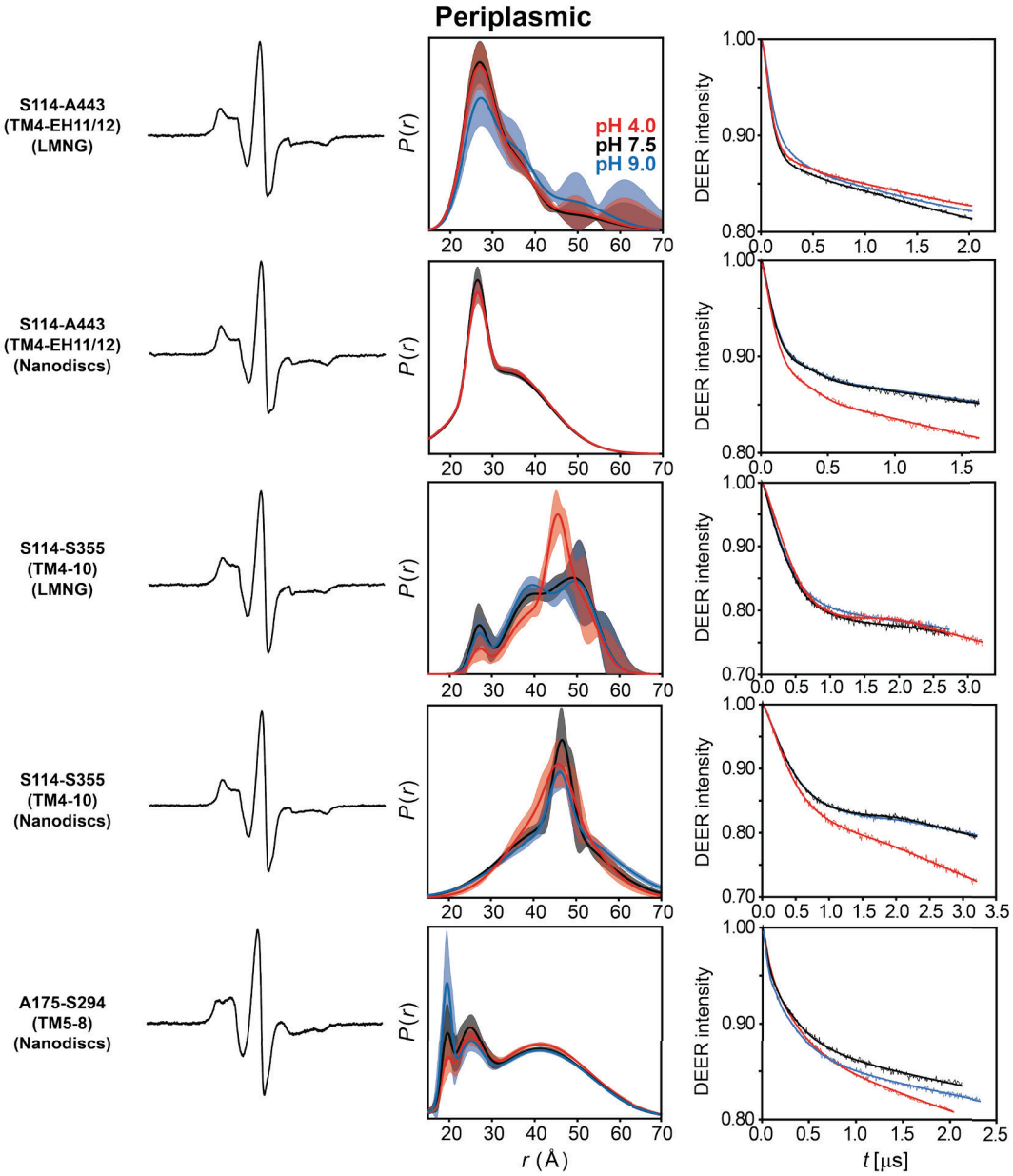

Data Appendix 8. DEER data analysis for the periplasmic side. For each mutant, from left to right, CW EPR, distance distributions, and the primary DEER traces along with the fits are shown.

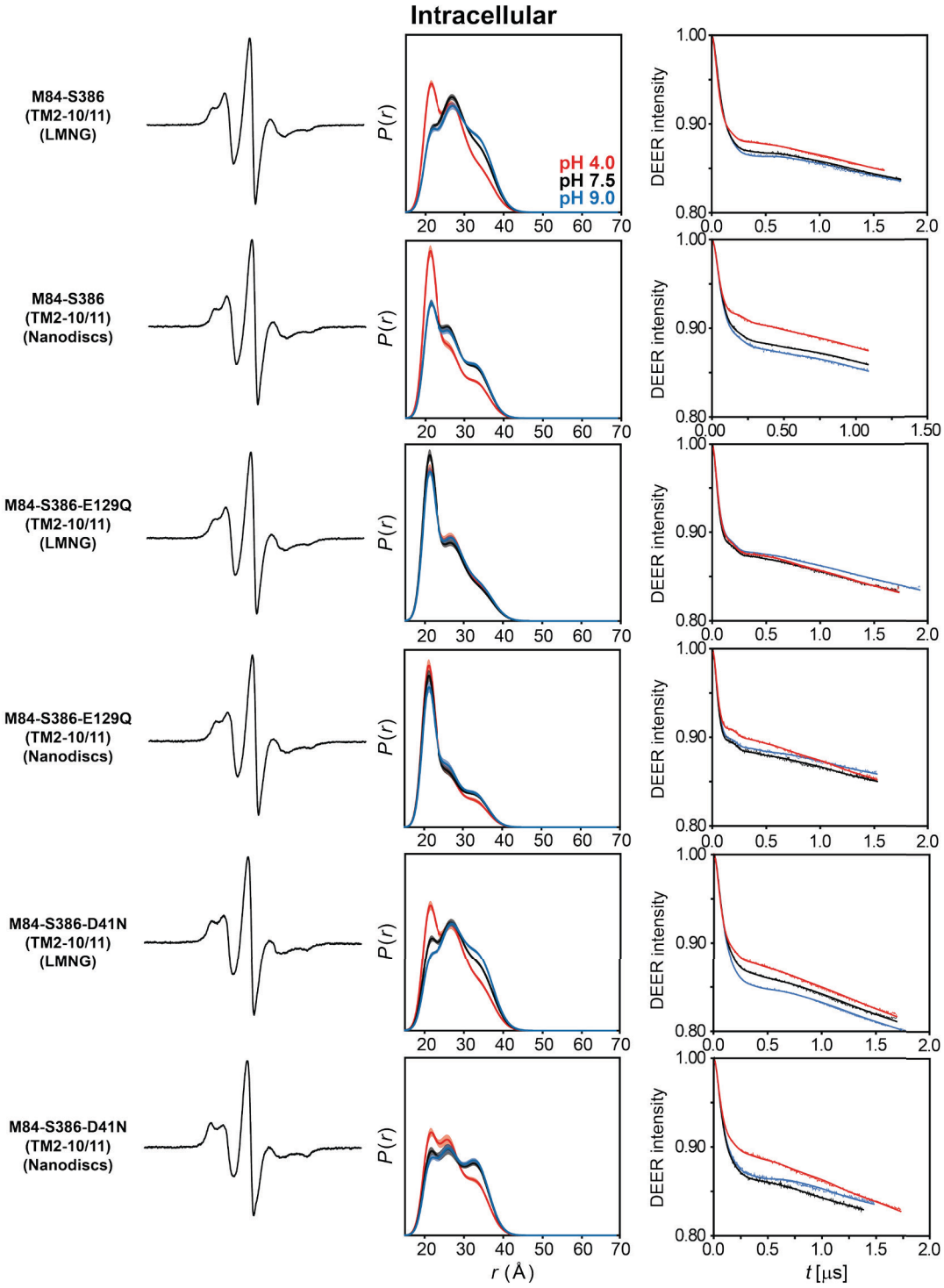

Data Appendix 9. DEER data analysis for the intracellular side. For each mutant, from left to right, CW EPR, distance distributions, and the primary DEER traces along with the fits are shown.

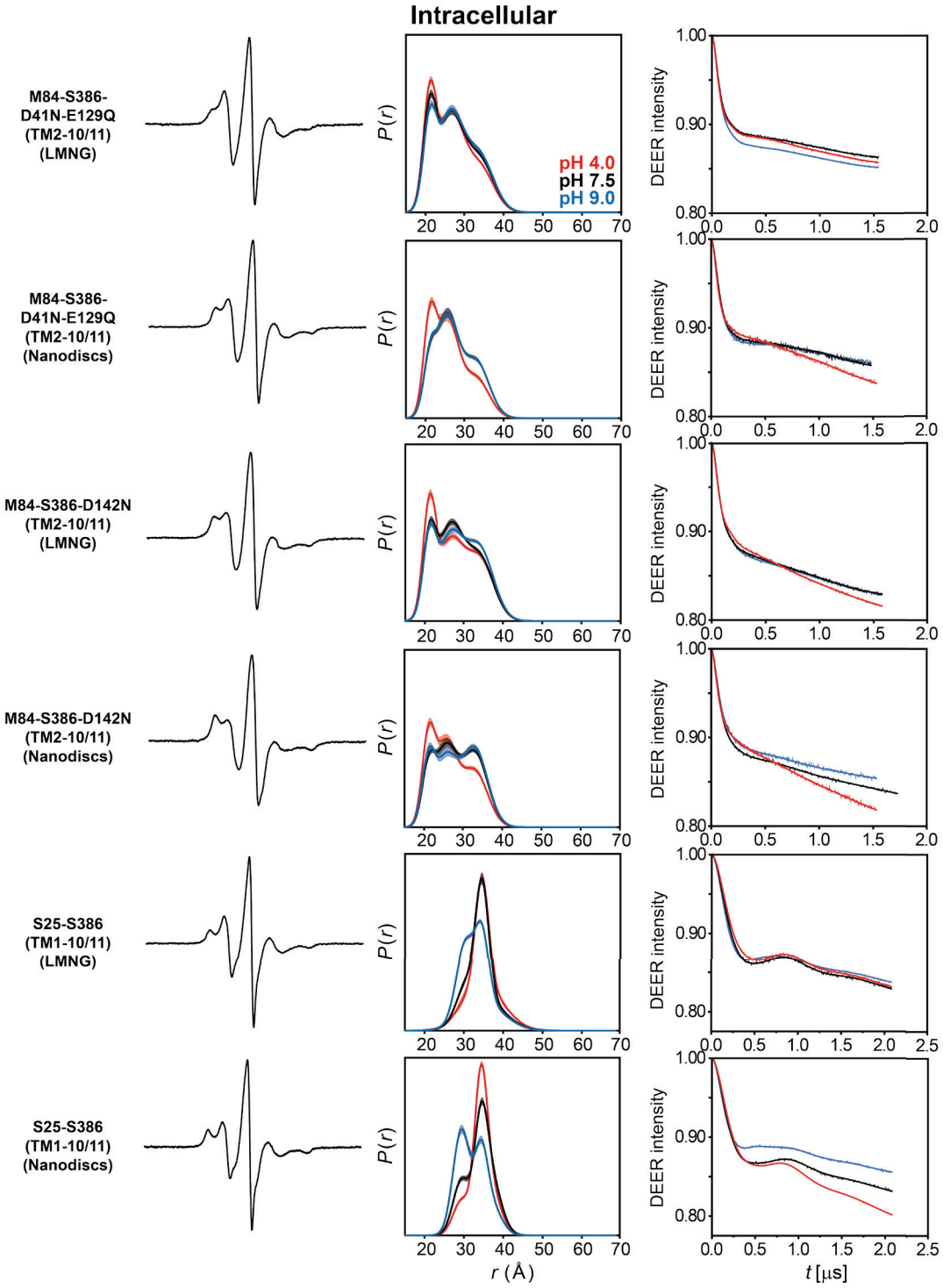

Data Appendix 10. DEER data analysis for the intracellular side. For each mutant, from left to right, CW EPR, distance distributions, and the primary DEER traces along with the fits are shown.

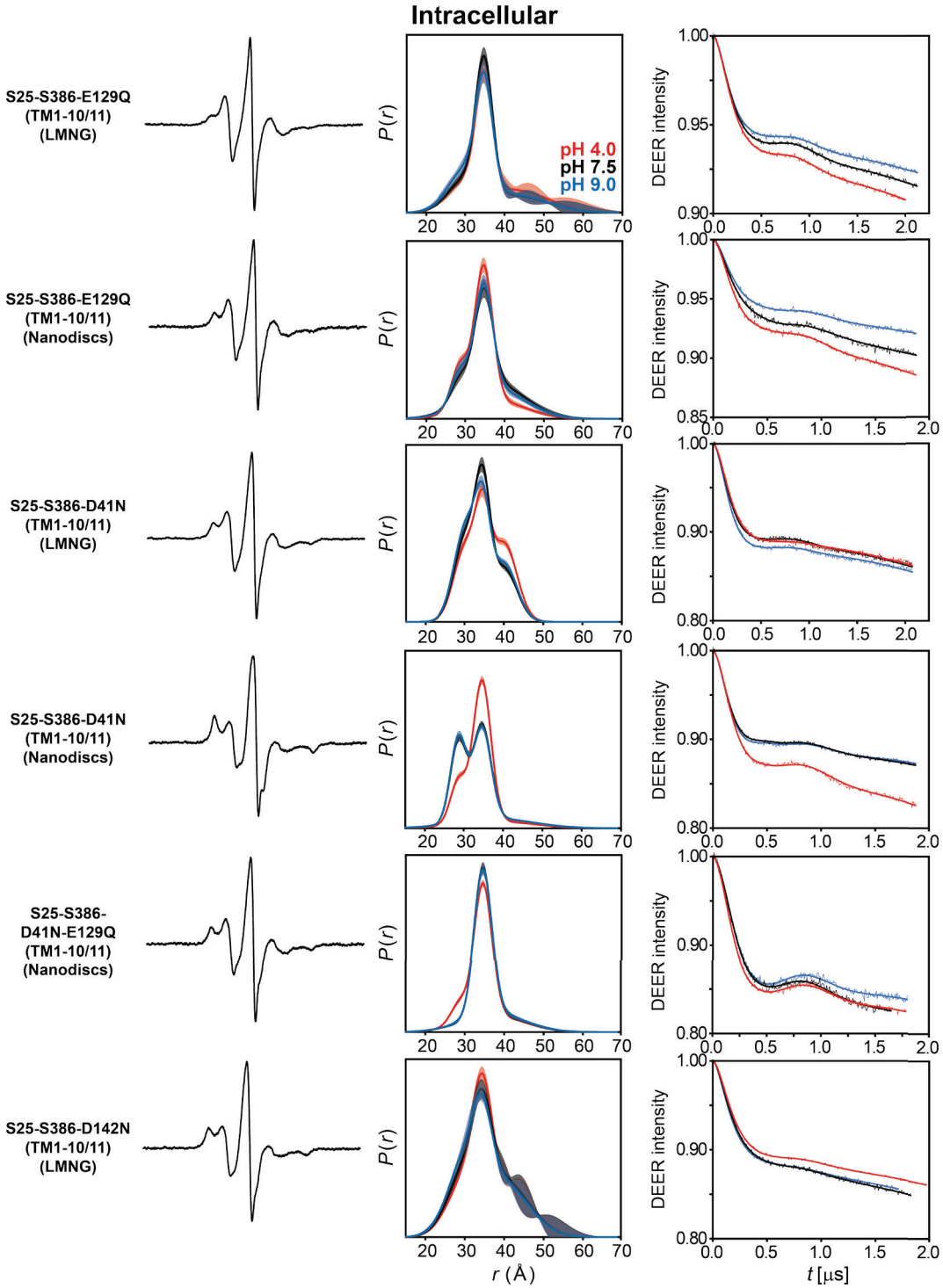

Data Appendix 11. DEER data analysis for the intracellular side. For each mutant, from left to right, CW EPR, distance distributions, and the primary DEER traces along with the fits are shown.

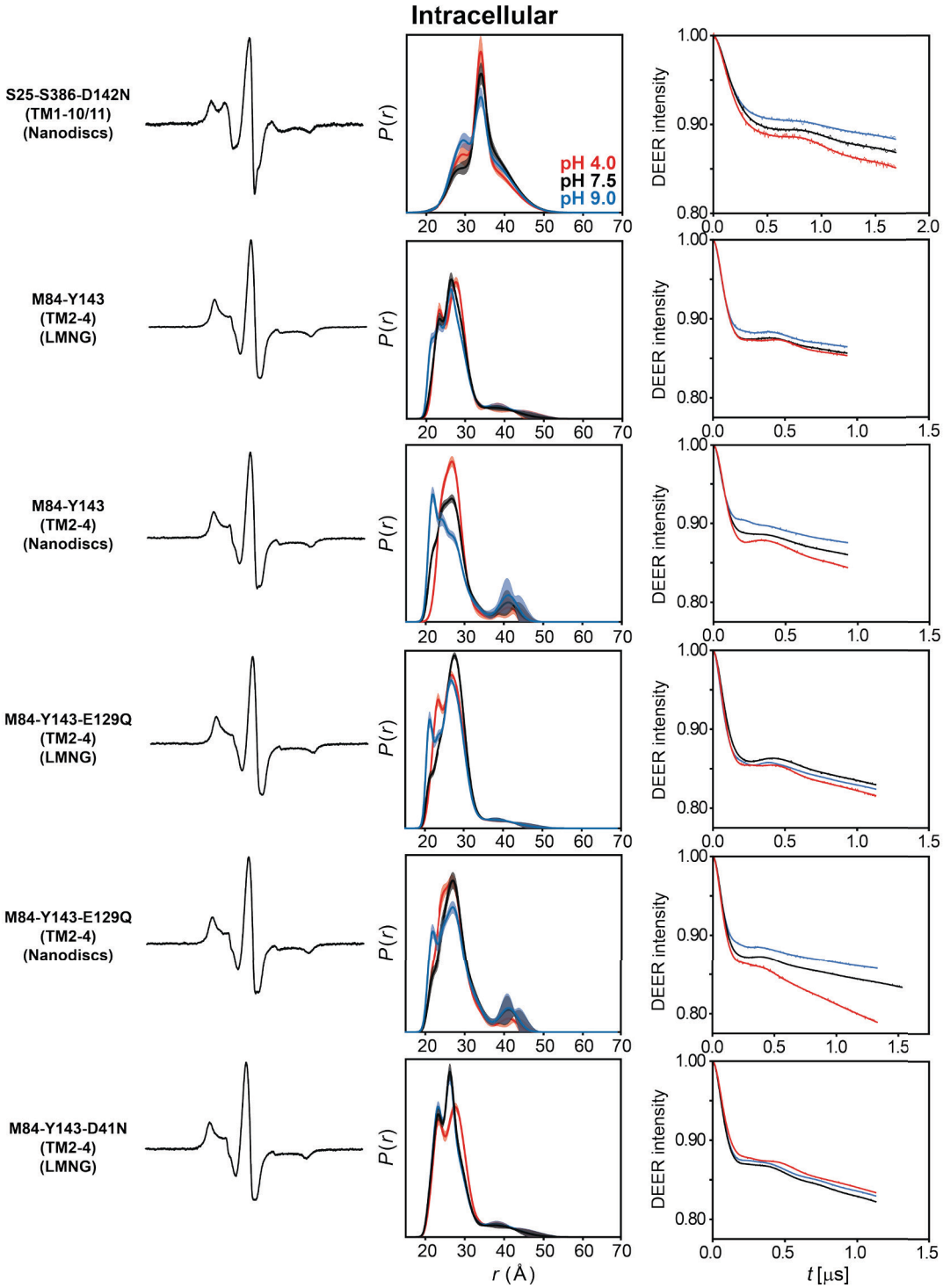

Data Appendix 12. DEER data analysis for the intracellular side. For each mutant, from left to right, CW EPR, distance distributions, and the primary DEER traces along with the fits are shown.

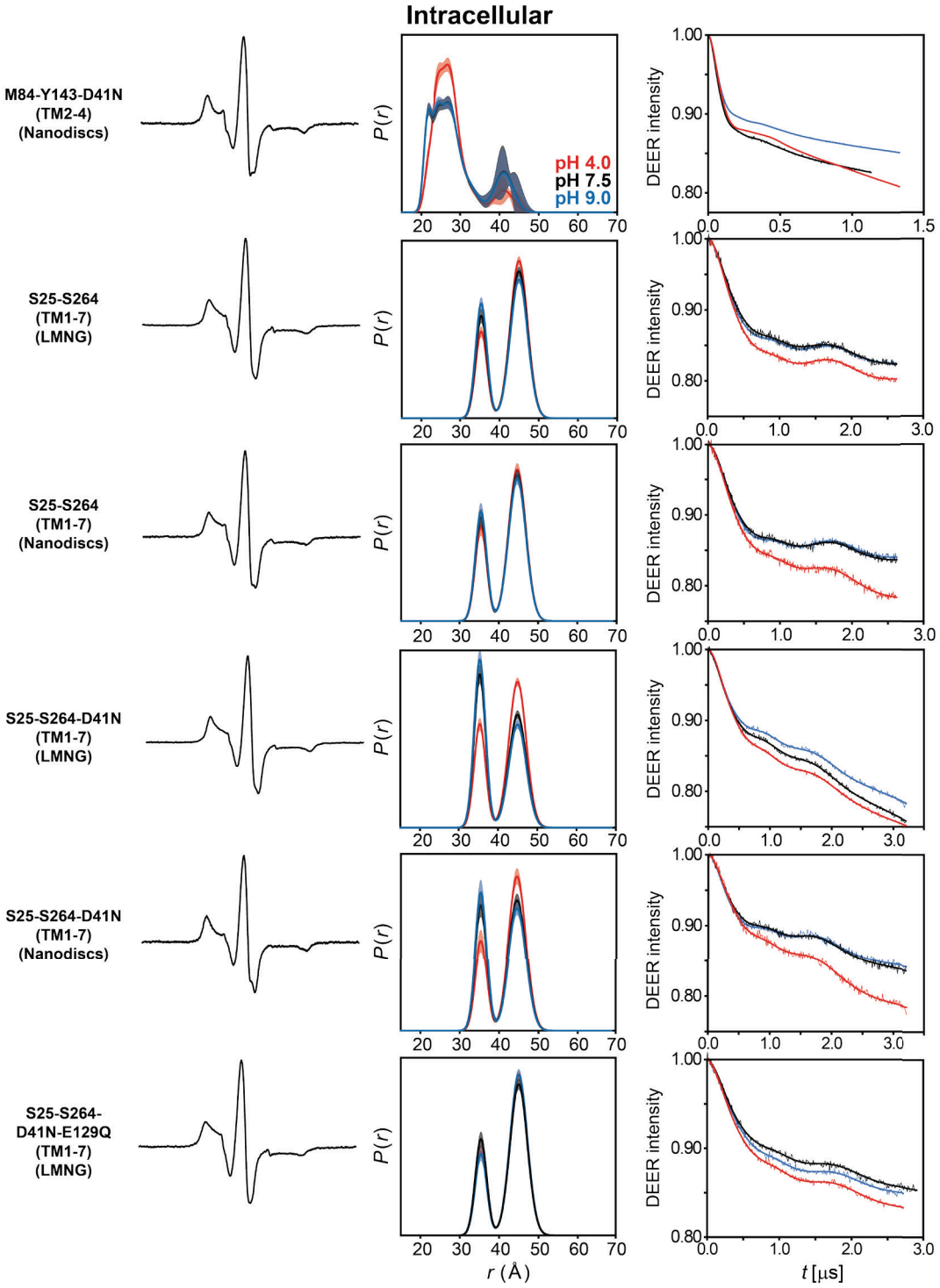

Data Appendix 13. DEER data analysis for the intracellular side. For each mutant, from left to right, CW EPR, distance distributions, and the primary DEER traces along with the fits are shown.

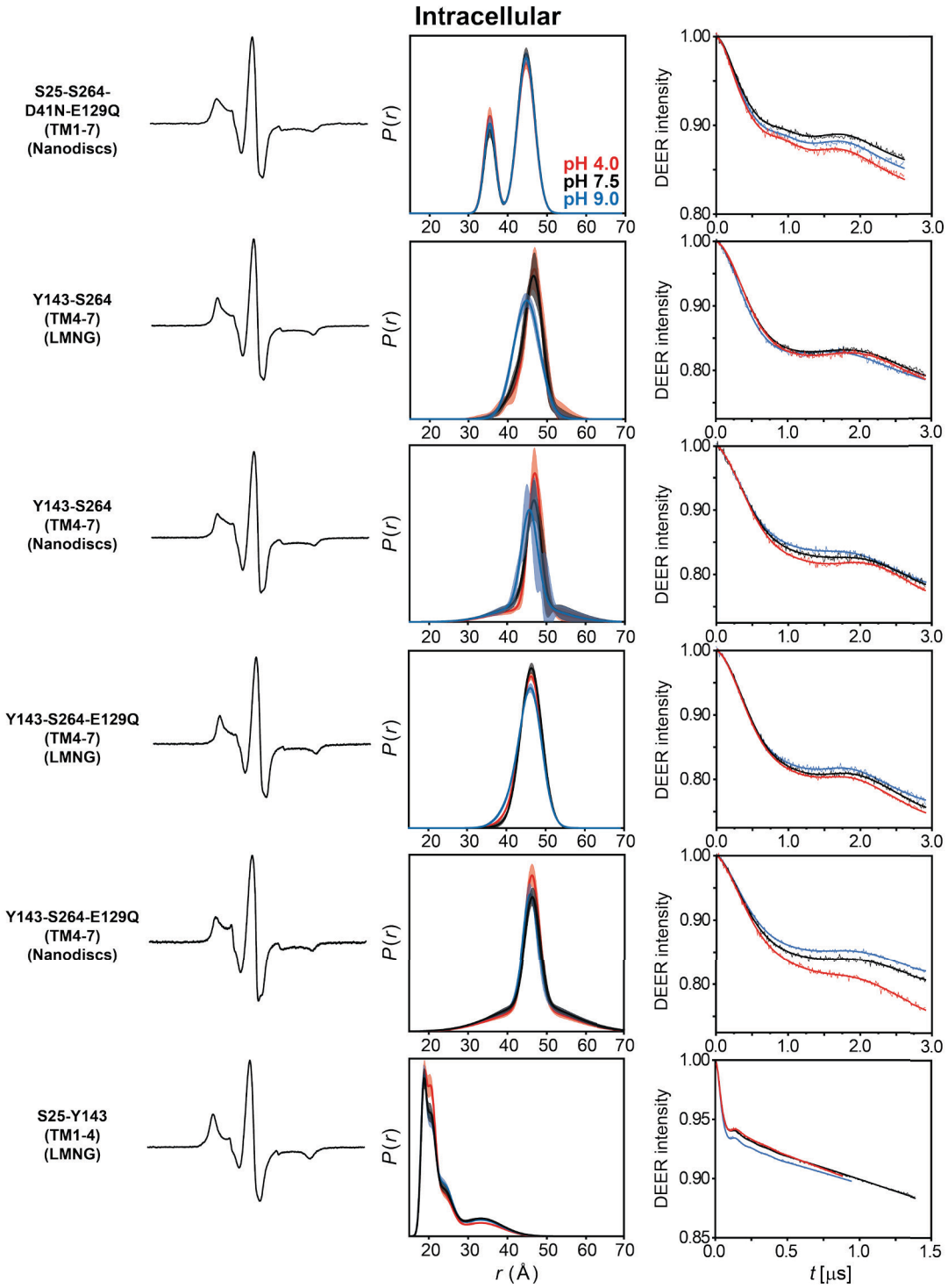

Data Appendix 14. DEER data analysis for the intracellular side. For each mutant, from left to right, CW EPR, distance distributions, and the primary DEER traces along with the fits are shown.

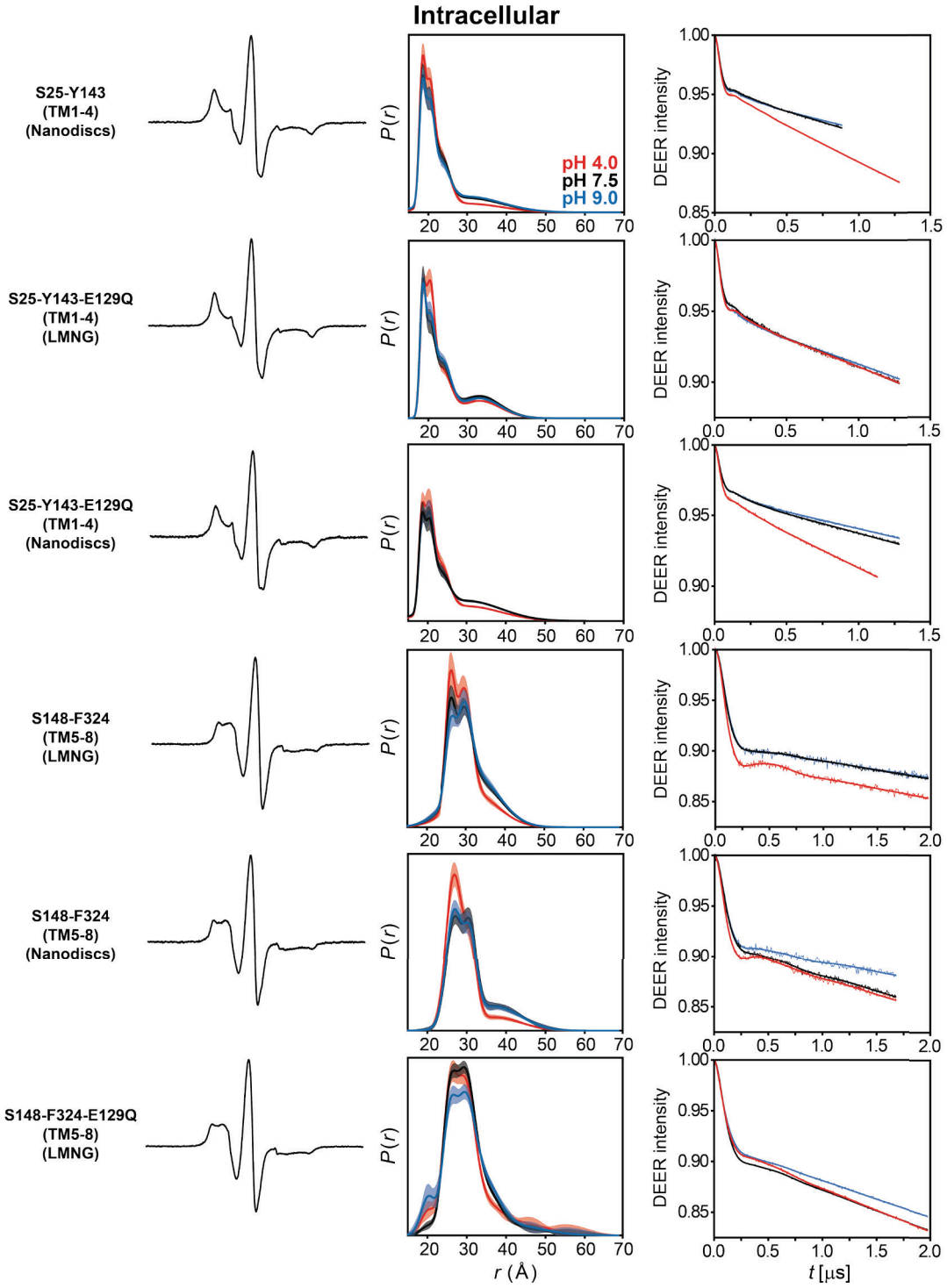

Data Appendix 15. DEER data analysis for the intracellular side. For each mutant, from left to right, CW EPR, distance distributions, and the primary DEER traces along with the fits are shown.

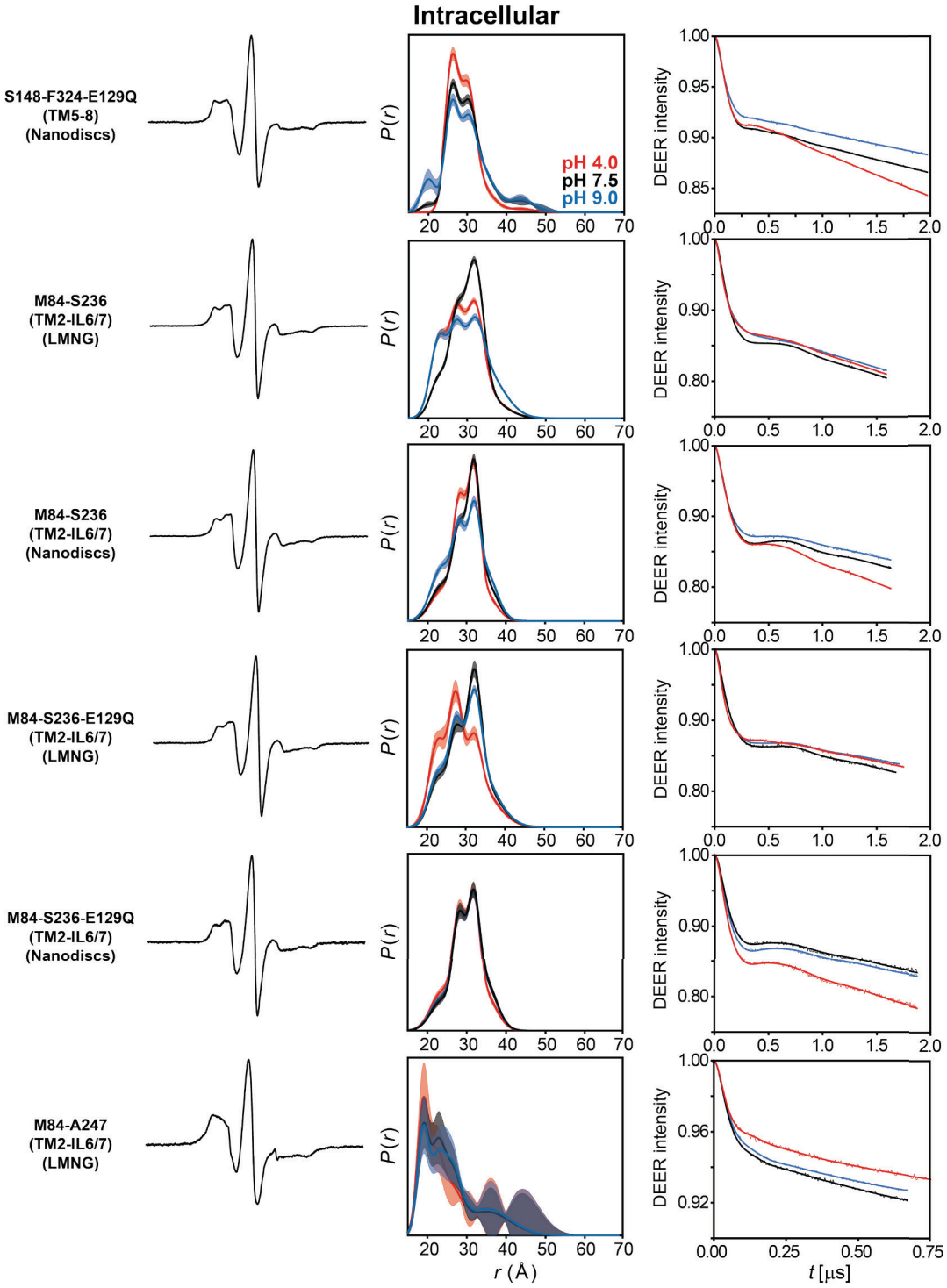

Data Appendix 16. DEER data analysis for the intracellular side. For each mutant, from left to right, CW EPR, distance distributions, and the primary DEER traces along with the fits are shown.

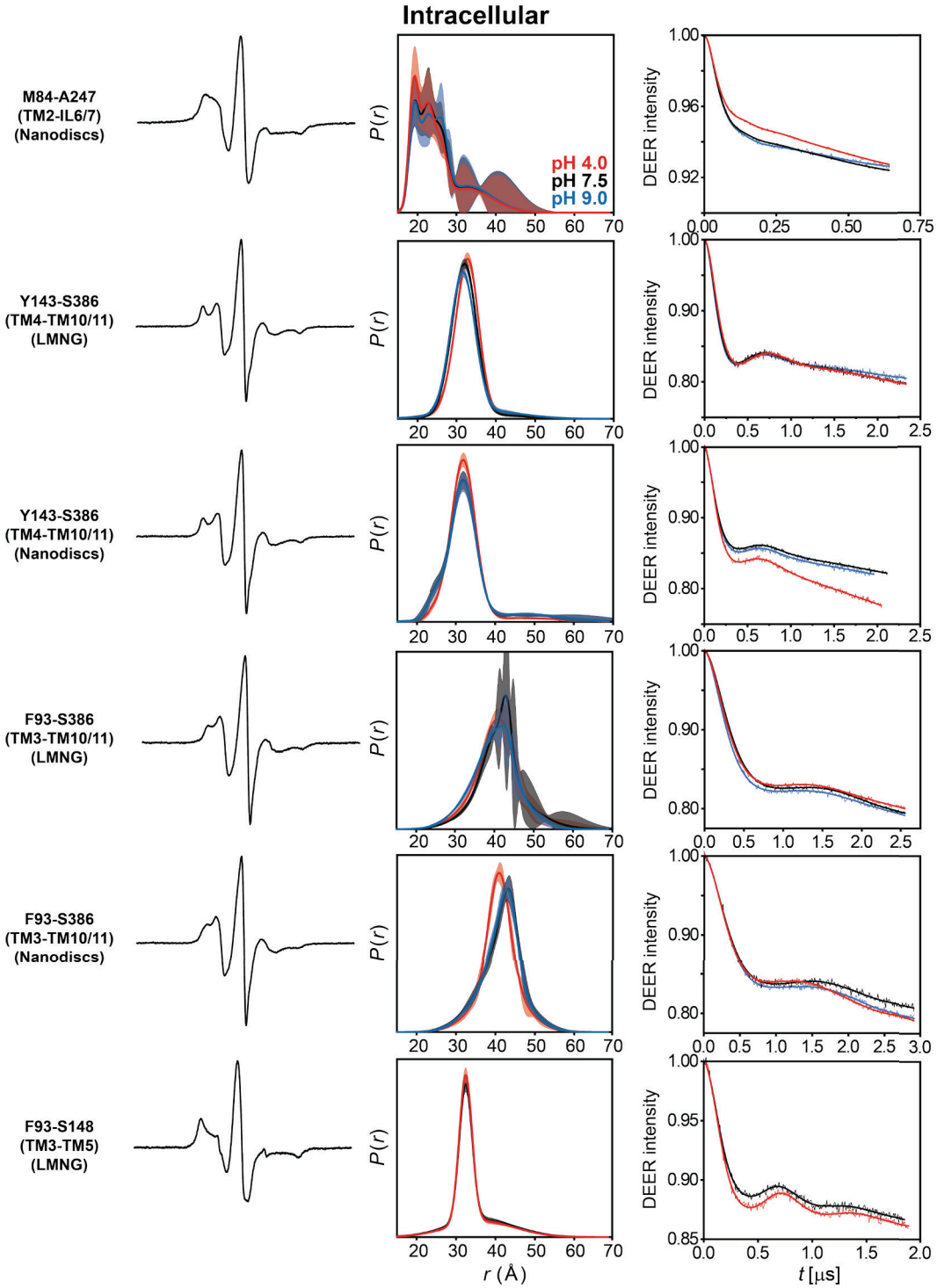

Data Appendix 17. DEER data analysis for the intracellular side. For each mutant, from left to right, CW EPR, distance distributions, and the primary DEER traces along with the fits are shown.

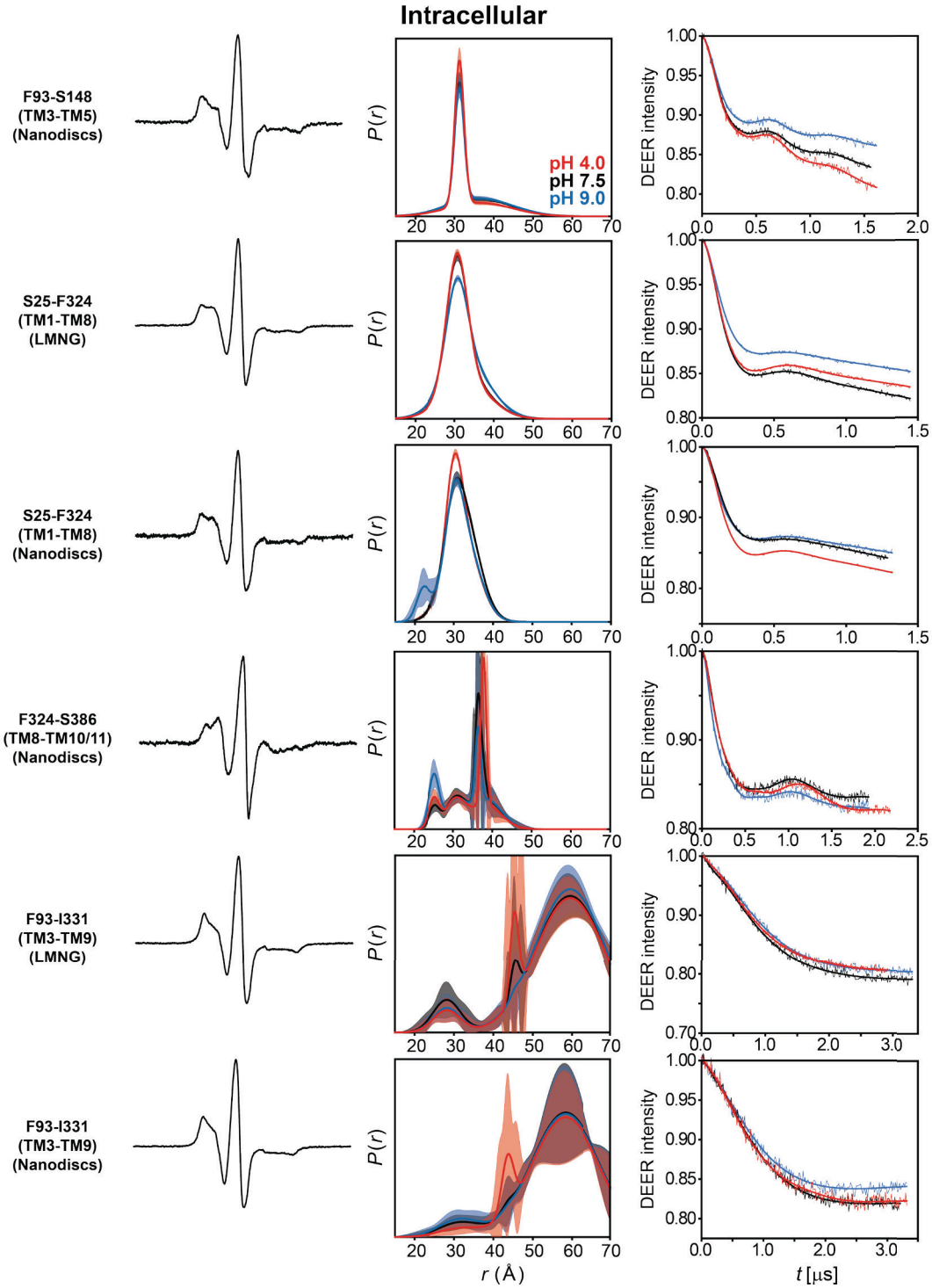

Data Appendix 18. DEER data analysis for the intracellular side. For each mutant, from left to right, CW EPR, distance distributions, and the primary DEER traces along with the fits are shown.